Order Number 9334968

# A measurement of the $\tau$ polarization at the Z resonance with the DELPHI detector at LEP

Chan, Antonio Wong, Ph.D.

Iowa State University, 1993

U·M·I
300 N. Zeeb Rd.
Ann Arbor, MI 48106

# A measurement of the $\tau$ polarization at the Z resonance with the DELPHI detector at LEP

by

Antonio Wong Chan

A Dissertation Submitted to the

Graduate Faculty in Partial Fulfillment of the

Requirements for the Degree of

DOCTOR OF PHILOSOPHY

Department: Physics & Astronomy
Major: High Energy Physics

**Approved:**

Signature was redacted for privacy.

**In Charge of Major Work**

Signature was redacted for privacy.

**For the Major Department**

Signature was redacted for privacy.

**For the Graduate College**

Iowa State University
Ames, Iowa
1993

# DEDICATION

To my family,
for their steadfast support and encouragement over the years.

# TABLE OF CONTENTS

# LIST OF FIGURES

# LIST OF TABLES

## ACKNOWLEDGEMENTS

I have been fortunate to have met so many kind people along this long road to obtaining my degree.

I would like to thank my family, for their understanding and support over the years. God has truly blessed me.

I am also grateful to my advisor, Prof. Eli Rosenberg, the High Energy Physics Program Director at Ames Laboratory, for his support, advice and comic relief during the last 3 years. It has been a pleasure working with him. Prof. Alexander Firestone's enthusiasm and skillful analysis techniques have been invaluable during my stay at CERN. I have learned much from him, and I would like to thank him for his willingness to help without fail.

I would like to thank Prof. Bert Crawley, Mr. Arthur Klein, Dr. Thomas Meyer and Mrs. Linda Shuck for their assistance and patience.

My gratitude is also extended to many scientists at CERN. Special thanks to Ugo Amaldi, Jean Eudes Augustin, Walter Bonivento, Herbert Burmeister, Mogens Dam, Michael Feindt, Barry King, Julio Lozano, Francisco Matorras, Baljeet Nijjhar, Luc Pape, Paolo Privitera, Duncan Reid and Pedro Vaz, for their assistance, suggestions and guidance at various stages during my stay at CERN and during the course of this work.

I am grateful to my fellow graduate student, Mr. David Edsall, for his tireless assistance and patience.

I should like to express my thanks to various people who have helped me at various times in the past, Mr. Shinichi Urano, Prof. Robert Webb (Texas A & M University) and Mr. Shah Zaman.

I am deeply in debt to the support staff at the DELPHI collaboration for their assistance and kindness during my stay in Geneva.

I am also thankful to many people in the Ames community for their support and encouragement, especially members of the University Baptist Church and the Iowa State Intervarsity Christian Fellowship chapter.

This work was performed in part using computer equipment supported by Ames Laboratory under contract no. W-7405-eng-82 with the U.S Department of Energy. The United States government has assigned the DOE Report number IS-T 1654 to this thesis.

# CHAPTER 1. INTRODUCTION

## An Overview of the Standard Model

Over the past seventy years or so, the field of particle physics has been rapidly evolving. The construction of large scale fixed target and colliding machines involving the collaboration of hundreds of physicists has been necessary. We have learned from these experiments that a picture of the universe comprised only of particles occurring naturally in ordinary matter (protons, neutrons, electrons, neutrinos and photons) is incomplete. Instead, it is possible to create many additional short-lived particles. The properties of all particles and the details of their interactions seem to be well described by a collection of theories known as the "Standard Model."

The Standard Model (SM) has its roots in the relativistic description of charged spin $\frac{1}{2}$ particles and their electromagnetic interactions provided by Dirac in 1927. In addition to the electromagnetic force, the SM must be able to describe weak interactions, such as in $\beta$ decay, $n \rightarrow p + e^- + \bar{\nu}_e$. In the late 60's, Weinberg, Salam and Glashow [1] proposed a model, in which the electromagnetic and weak forces were unified. In this model ($SU(2) \times U(1)$), leptons are treated as weak isospin doublets $(\nu_e, e)$, $(\nu_\mu, \mu)$, $(\nu_\tau, \tau)$. Four gauge fields are then necessary to describe the interactions, the photon and three new gauge bosons, $W^\pm$ and $Z^\circ$. For this theory to yield finite results (renormalizability) [2], Weinberg invoked spontaneous symmetry breaking via the Higgs mechanism [3]. In this manner, the SM not only generated masses for the $W^\pm$ and $Z^\circ$ (Figure 1.1), but it also implies the existence of a new particle, the Higgs boson.

The gauge bosons, $\gamma$, $W^\pm$ and $Z^\circ$, couple to quarks in the same manner as to leptons. The quarks are also spin $\frac{1}{2}$ fermions and form weak isospin doublets, and in addition, there is mixing between the various types of quarks [4]. The SM predicts

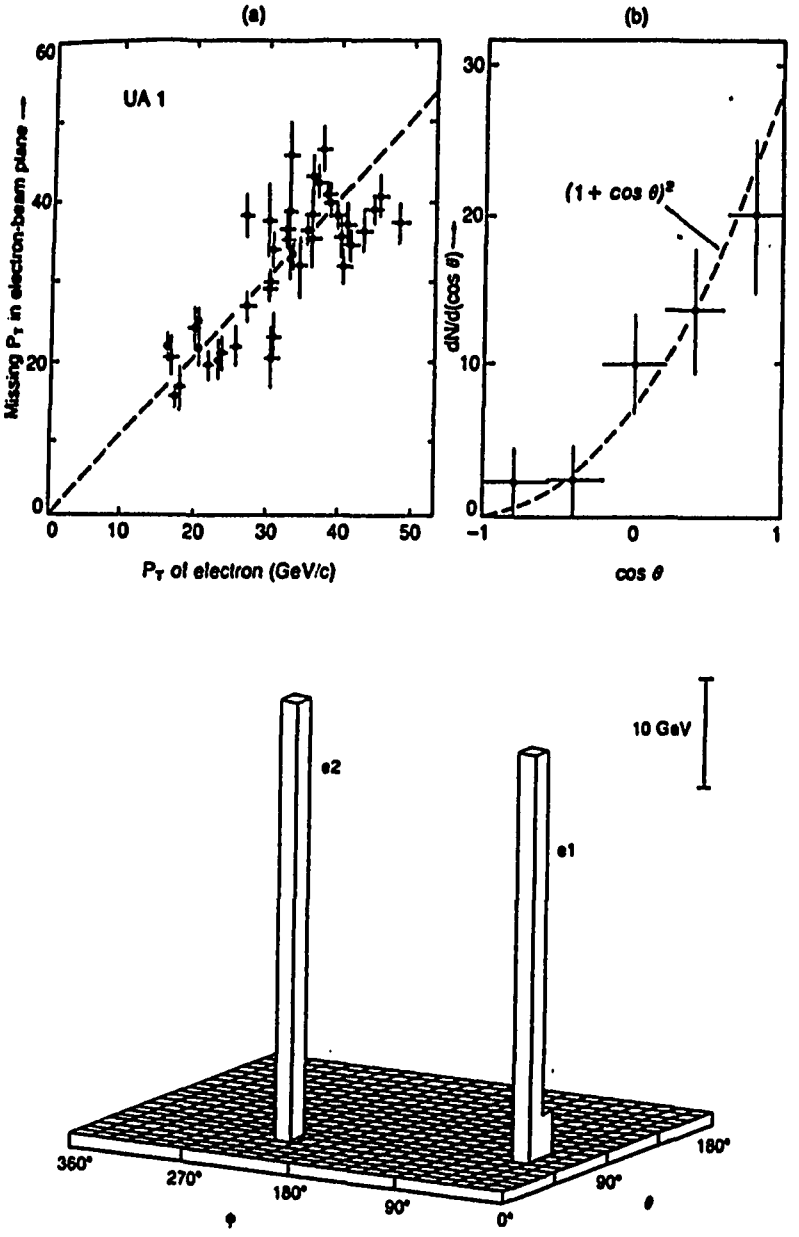


Figure 1.1: The weak force gauge bosons. (a) Missing $p_T$ in electron/beam plane plotted against $p_T$ in $W^- \rightarrow e^-\overline{\nu}_e$ decays, attributed to neutrinos. (b) Angular distribution of decay electrons in rest frame of $W$ boson. A $Z^0 \rightarrow e^+e^-$ event in the UA1 detector, with energy plotted as a function of polar and azimuthal angles (bottom) [5].

Table 1.1: Particles & fundamental interactions in the Standard Model.

| Type | Particle Name | Charge | Strong | EM | Weak |
|---|---|---|---|---|---|
| quarks | u , c ,(t) | $+\frac{2}{3}$ | yes | yes | yes |
| | d , s , b | $-\frac{1}{3}$ | yes | yes | yes |
| leptons | $\nu_e, \nu_\mu, \nu_\tau$ | 0 | no | no | yes |
| | e , $\mu, \tau$ | $-1$ | no | yes | yes |
| gauge bosons | $\gamma, W^{\pm}, Z^{\circ}$, 8 gluons, (Higgs) | | | | |

the existence of the top quark, the doublet partner of the bottom quark. The current lower limit on the mass of the top quark, set by the CDF collaboration at FNAL, is $M_t > 91\ GeV/c^2$ [6].

The final piece of the SM is a description of the strong force, which is responsible for quark-quark binding in hadrons. The strong force is described by a $SU(3)$ local gauge symmetry theory, with the introduction of the color quantum number and eight gauge bosons, known as gluons. This theory is known as Quantum Chromodynamics (QCD). The composite nature of hadrons has been demonstrated by electron-nucleon deep inelastic scattering experiments. In these experiments, an electron beam of variable energy is scattered off a fixed target. The scattering cross section is a function of energy, and for high enough energies, the nucleon behaves as a free fermion, signaling that structureless particles (quarks) reside within the nucleon.

In Table 1.1, a summary of the known constituents of matter as described by the SM is given. Quarks and leptons are separated into 3 distinct generations in accordance with their symmetry under weak interactions. Under the assumption that additional generations have the same structure and that new neutrinos are massless, results from LEP have constrained the number of generations to three at the 98% confidence level [7].

## The Electroweak Interaction

In the annihilation s-channel process $e^+e^- \rightarrow \gamma \rightarrow e^+e^-$, the interaction amplitude may be expressed as

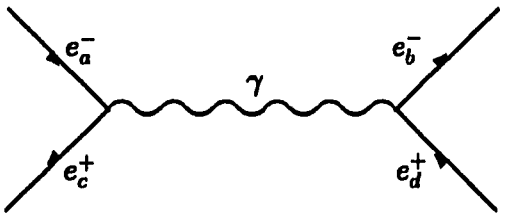


Figure 1.2: Feynman diagram representing $\gamma$-exchange in $e^+e^-$ annihilations.

$$\Re_\gamma = -(e\overline{\psi}_c\gamma^\mu\psi_a)\frac{g\mu\nu}{q^2}(e\overline{\psi}_d\gamma^\nu\psi_b), \tag{1.1}$$

where the middle term is the photon propagator. $\psi$ and $\overline{\psi}$ represent field operators, $\gamma^\mu$ are $4 \times 4$ Dirac matrices, and $q$ is the four-momentum transfer (Figure 1.2).

The strength of the electromagnetic interaction can be characterized as

$$\sim \frac{e^2}{q^2}, \tag{1.2}$$

where $e$ is the electromagnetic coupling constant. The corresponding expression for massive vector boson exchange, which governs weak decays, is

$$\frac{g^2}{8(M_W^2 - q^2)}. \tag{1.3}$$

Therefore, we see that when $q^2 \ll M_W^2$, the propagator for weak interactions disappears, that is, the particles interact essentially at a point. This leads one to believe that weak interactions are weak not because $g \ll e$, but because $M_W$ is large.

In reality, $g \approx e$, so that at energies $O(M_W)$ and above, the weak interaction is of comparable strength to the electromagnetic interaction. The approximate equality of these coupling constants suggests that the observed interactions may be due to some combined electroweak interaction.

## The V-A Nature of Weak Interactions

The weak charged current interaction between an electron and its neutrino can be described by

$$J^{\mu} = \overline{\psi}_e \gamma^{\mu} \frac{1}{2}(1-\gamma^5)\psi_{\nu}, \tag{1.4}$$

where $\psi_{\nu} = \begin{pmatrix} \phi_L \\ \phi_R \end{pmatrix}$ is a four component spinor ($\phi_L$ and $\phi_R$ are two component spinors).

Applying the operator $\frac{1}{2}(1-\gamma^5)$ on $\psi_{\nu}$ gives

$$\frac{1}{2}(1-\gamma^5)\psi_{\nu} = \begin{pmatrix} \phi_L \\ 0 \end{pmatrix}. \tag{1.5}$$

That is, only left-handed (LH) $\nu_e$ (and righthanded (RH) $\overline{\nu}_e$) are coupled to electrons by the weak interactions (Figure 1.3). Neutrinos only interact via weak forces, so there are no other ways to observe them. To this date, $\nu_R$ (or $\overline{\nu}_L$) has not been observed, and the limits on the neutrino mass are consistent with zero. For massless particles, the handeness and helicity are identical.

The $J^{\mu}$ contains both vector, $\gamma^{\mu}$, and axial-vector, $\gamma^{\mu}\gamma^5$, couplings of the same magnitude and opposite sign, and is known as the V-A interaction. The vector term is of the same form as the electromagnetic interaction (1.1). The relative strengths of the two interactions is characterized by the weak mixing angle, $\theta_W$, which is discussed in the next section. Parity is violated in this process, since the operator $(1-\gamma^5)$ projects out only the LH component of $\psi_{\nu}$. One can write the charged current as

$$J_{\mu}^{(CC)} = \overline{\psi}_a \gamma_{\mu} \frac{1}{2}(1-\gamma^5)\psi_b, \tag{1.6}$$

where $a, b$ can be leptons or quarks. The neutral current has a similar form (Figure 1.4)

$$J_{\mu}^{(NC)} = \overline{\psi}_a \gamma_{\mu} \frac{1}{2}(v_a - a_a\gamma^5)\psi_a. \tag{1.7}$$

Unlike the charged current, where $v_a = a_a = 1$, the neutral current in the SM has

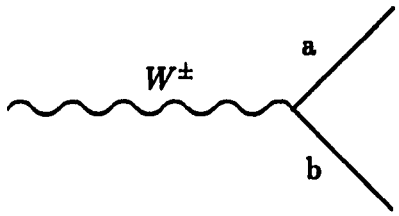


Figure 1.3: Feynman diagram representing $W^{\pm}$ decays.

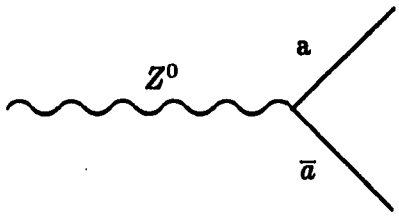


Figure 1.4: Feynman diagram representing $Z^{\circ}$ decays.

$$v_a = I_a^3 - 2Q_a sin^2\theta_W, \qquad a_a = I_a^3, \tag{1.8}$$

where $I_a^3$ and $Q_a$ are the third component of the weak isospin and the charge of fermion $a$, respectively. Table 1.2 lists the values of $v$ and $a$ for the known leptons and quarks.

### Electroweak Unification and the Weak Mixing Angle

Leptons can interact through electromagnetic and weak interactions. As we have seen, both the form and strengths of the interactions are strikingly similar. The

Table 1.2: The $Z \rightarrow f\overline{f}$ vertex factors in the Standard Model.

| fermion | $Q_f$ | $a_f$ | $v_f$ |
|---|---|---|---|
| $\nu_e, \nu_\mu, \nu_\tau$ | 0 | $\frac{1}{2}$ | $\frac{1}{2}$ |
| $e^-, \mu^-, \tau^-$ | -1 | $-\frac{1}{2}$ | $-\frac{1}{2} + 2sin^2\theta_W$ |
| $u, c, (t)$ | $\frac{2}{3}$ | $\frac{1}{2}$ | $+\frac{1}{2} - \frac{4}{3}\ sin^2\theta_W$ |
| $d, s, b$ | $-\frac{1}{3}$ | $-\frac{1}{2}$ | $-\frac{1}{2} + \frac{2}{3}\ sin^2\theta_W$ |

electromagnetic current is a pure vector current having both LH and RH couplings. The weak neutral current has both vector and axial-vector parts and also couples to both LH and RH components. However, the V-A charged weak current couples to LH components only. This difference between the weak charged and electromagnetic current, as well as the apparent different strengths, masked the underlying unity of the two interactions. It was not until the mid-60's, that Glashow, Weinberg and Salam finally overcame these difficulties. Necessary ingredients were the existence of the weak neutral current and of heavy intermediate vector bosons.

The SM demands that interactions between leptons conserve weak isospin $I$ and hypercharge $Y$, by requiring the Lagrangian to be invariant under the $SU(2)_L$ group of transformations in weak isospace *and* the $U(1)_Y$ group of transformations in weak hypercharge, the so-called $SU(2)_L \times U(1)_Y$ symmetry group. The weak hypercharge is related to the electric charge through a Gell-Mann Nishijima relation

$$Q = e(I^3 + \frac{1}{2}Y). \tag{1.9}$$

In this context, the basic electroweak interaction is

$$-ig(J^i)^\mu W^i_\mu - ig'\frac{1}{2}(j^Y)^\mu B^\mu, \tag{1.10}$$

where, $J^{(i)\mu}$ $(i = 1,2,3)$ and $j^Y$ are the weak isospin current and weak hypercharge current, respectively.

$B^\mu$ and $W^i_\mu$ $(i = 1,2,3)$ are the gauge bosons corresponding to these two interactions. By requiring the neutrinos to have no ordinary electromagnetic interactions, we can define the observed vector bosons as linear combinations of these fields:

$$A_\mu = B_\mu cos\theta_W + W^3_\mu sin\theta_W \quad \longrightarrow \quad photon\ \ field, \tag{1.11}$$

$$Z_\mu = -B_\mu sin\theta_W + W^3_\mu cos\theta_W \quad \longrightarrow \quad Z\ \ field, \tag{1.12}$$

$$W^\pm_\mu = \sqrt{\frac{1}{2}}(W^1_\mu \mp W^2_\mu) \quad \longrightarrow \quad W^\pm\ \ field. \tag{1.13}$$

The weak mixing angle, $\theta_W$, plays a fundamental role in the weak interaction processes in the SM. Among other things, it specifies the relative strength of the neutral and charged weak interactions

$$\rho = \frac{M_W^2}{M_Z^2 \cdot cos^2\theta_W}. \tag{1.14}$$

The average experimental value is $\rho = 1.0095 \pm 0.0071$ [8], consistent with the simplest theoretical models.

Also, the mixing angle can be expressed as

$$gsin\theta_W = g'cos\theta_W = e \qquad \rightarrow \qquad tan\theta_W = \frac{g'}{g}, \tag{1.15}$$

where $g$ and $g'$ are the weak coupling constants between the fermions and the $W_\mu^i$ and $B^\mu$ fields, respectively. These coupling constants are related to the electromagnetic coupling constant, $e$, through the weak mixing angle.

Lastly, the degree of V-A mixing in weak neutral interactions can also be determined from the weak mixing angle. The ratio

$$\frac{v_l}{a_l} = \frac{I_l^3 - 2Q_l sin^2\theta_W}{I_l^3}, \tag{1.16}$$

where $l$ is any particle which interacts via the neutral current, determines the weak mixing angle, thus offering a unique opportunity to study $Z^\circ$ decays.

### $e^+e^-$ Annihilations at the $Z^\circ$ Resonance

The interaction amplitudes corresponding to $\gamma$ and $Z$ exchange for the process $e^+e^- \rightarrow l^+l^-$ (s-channel photon exchange only) are

$$\Re_\gamma = -\frac{e^2}{p^2}(\overline{\psi}_l\gamma^\nu\psi_l)(\overline{\psi}_e\gamma_\nu\psi_e), \tag{1.17}$$

$$\Re_Z = \frac{g^2}{4cos^2\theta_W}\left[\overline{\psi}_l\gamma^\nu(v_l - a_l\gamma^5)\psi\right]\frac{i(g^{\nu\sigma} - q^\nu q^\sigma/M_Z^2)}{M_Z^2 - q^2}\left[\overline{\psi}_e\gamma_\sigma(v_e - a_l\gamma^5)\psi\right]. \tag{1.18}$$

The corresponding differential cross section is

$$\frac{d\sigma}{d\Omega} = \frac{1}{64\pi^2 s}|\Re|^2, \tag{1.19}$$

where,

$$\Re = \Re_\gamma + \Re_Z, \qquad s = (E_{CM})^2 = (E^{e^-}_{CM} + E^{e^+}_{CM})^2. \tag{1.20}$$

If we assume lepton universality (see "Lepton Universality"), we obtain

$$\frac{d\sigma}{d\Omega} = \frac{\alpha^2}{4s}\left[A_0(1+cos^2\theta) + A_1 cos\theta\right], \tag{1.21}$$

where,

$$\chi(s) = \left(\frac{G_F M_Z^2}{8\pi\alpha\sqrt{2}}\right)\frac{s}{s - M_Z^2 + is\Gamma_Z/M_Z}, \tag{1.22}$$

$$A_0 = 1 + 2Re(\chi(s))v^2 + |\chi(s)|^2(v^2+a^2)^2, \tag{1.23}$$

$$A_1 = 4Re(\chi(s))a^2 + 8|\chi(s)|^2 v^2 a^2. \tag{1.24}$$

Since $e^+e^-$ annihilation can occur through both electromagnetic ($\gamma$) and weak neutral current ($Z$) interactions, one should be able to observe the interference effect between the two currents (Figure 1.5). The electroweak interference term in (1.21) is linear in $cos\theta$, so the symmetric angular distribution from the QED term (quadratic in $cos\theta$) is spoiled, and gives rise to a forward-backward asymmetry (1.38).

To obtain an estimate of the production rates, we can compute the ratio of the full cross-section to the QED cross section

$$\frac{(e^+e^- \to l^+l^-)}{\sigma_{QED}} = A_0, \qquad \sigma_{QED} = \frac{4\pi\alpha^2}{3s}. \tag{1.25}$$

Notice that this does not hold for quarks, since $v_q, a_q \neq v_l, a_l$, and the expression for quarks has an additional factor of 3 due to color. The result is

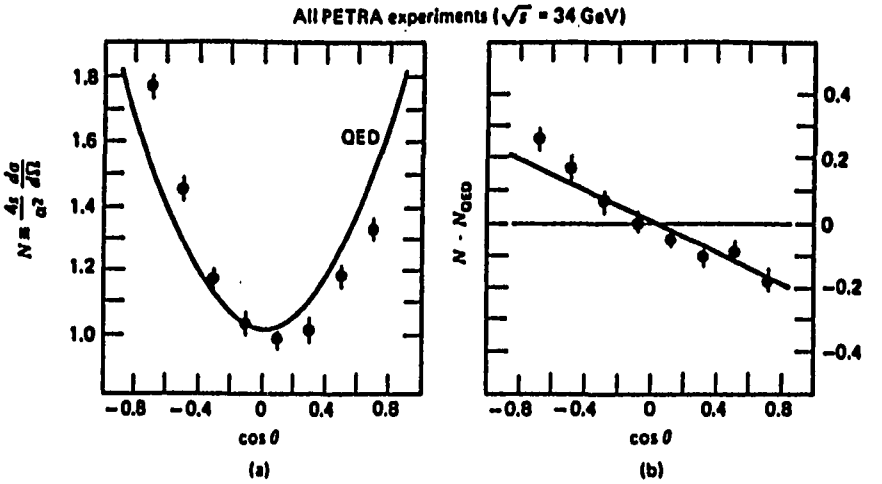


Figure 1.5: The electroweak interference. (a) The $cos\theta$ distribution for the process $e^+e^- \rightarrow \mu^+\mu^-$ does not follow the QED prediction. (b) The discrepancy is explained by the interference of the virtual Z and $\gamma$ contributions [9].

$$\frac{(e^+e^- \rightarrow q\bar{q})}{\sigma_{QED}} = 3\left[Q_q^2 + 2Q_q Re(\chi(s))v_q v_e + |\chi(s)|^2(v_q^2 + a_q^2)(v_e^2 + a_e^2)\right]. \quad (1.26)$$

These two ratios, at $s \simeq M_Z^2$, are of the order of $10^2 - 10^3$. Such a large enhancement over $\sigma_{QED}$ was a major motivation for the construction of the LEP collider ($s = M_Z^2$) at CERN, which offers the opportunity to study $Z^\circ$ decays with its unmatched statistical power.

## The $\tau$ Lepton

In 1975, Martin Perl and colleagues working at the Mark I detector at SLAC, observed 24 $e\mu$ events in $e^+e^-$ annihilations, leading to the discovery of the tau lepton, the charged lepton of the third generation of particles [10]. It took some time to establish the discovery, due to several complicating factors. The most serious of these

Table 1.3: Major decay modes and branching ratios of the $\tau$ lepton.

| Decay Mode | Branching Ratio |
|---|---|
| $e^-\overline{\nu}_e\nu_\tau$ | $17.93 \pm 0.26\%$ |
| $\mu^-\overline{\nu}_\mu\nu_\tau$ | $17.58 \pm 0.27\%$ |
| $\pi^-\nu_\tau$ | $11.60 \pm 0.40\%$ |
| $\pi^-\pi^\circ\nu_\tau$ | $24.00 \pm 0.60\%$ |
| $\pi^-\pi^+\pi^-\nu_\tau$ | $05.60 \pm 0.70\%$ |
| $h^-2\pi^\circ\nu_\tau$ | $10.30 \pm 0.90\%$ |

was that the energy threshold for the production of the $\tau^+\tau^-$ pair is approximately 3.6 $GeV$, which is very close to the threshold of 3.72 $GeV$ required for the production of a charmed meson-pair $D^\circ\overline{D^\circ}$. Since the latter can decay via weak interactions, they can also produce $e\mu$ final states. The two pieces of evidence that eventually established the $\tau$ decay beyond any doubts were the lack of any other hadronic tracks in the observed events (seen in $D^\circ\overline{D^\circ}$ decays) and the production of $e\mu$ final states below the threshold of the charmed meson-pair production (due to the lower mass of the $\tau$). The energy dependence of the production rate has determined the spin of the tau to be $\frac{1}{2}$ (Figure 1.6). The $\tau$ has one new feature compared to the electron and the muon. Because of its large mass, it can decay not only into lighter leptons ($e$'s and $\mu$'s) but also into hadrons ($\pi$'s and $\rho$'s). The major decay modes and branching ratios of the tau lepton are given in Table 1.3 [8].

Apart from this new feature, the $\tau$ lepton seems to be just a more massive copy of the electron and muon. Further studies have indicated that the $\tau$ has its own $\nu_\tau$ and its own tau lepton number, which is conserved in weak interactions.

It is amusing to note that, years earlier, Y. S. Tsai. predicted the existence of a more massive version of the electron in his classical paper *Decay Correlations of Heavy Leptons in* $e^+ + e^- \rightarrow l^+ + l^-$, in which Tsai provided the production and decay theory, including the decay modes and their branching ratios for various lepton masses [11]. This very elegant and detailed paper began with the speculation, *"Since muons exist in nature for no apparent reason, it is possible that other heavy leptons may also exist in nature. If one discovers heavy leptons, one may be able*

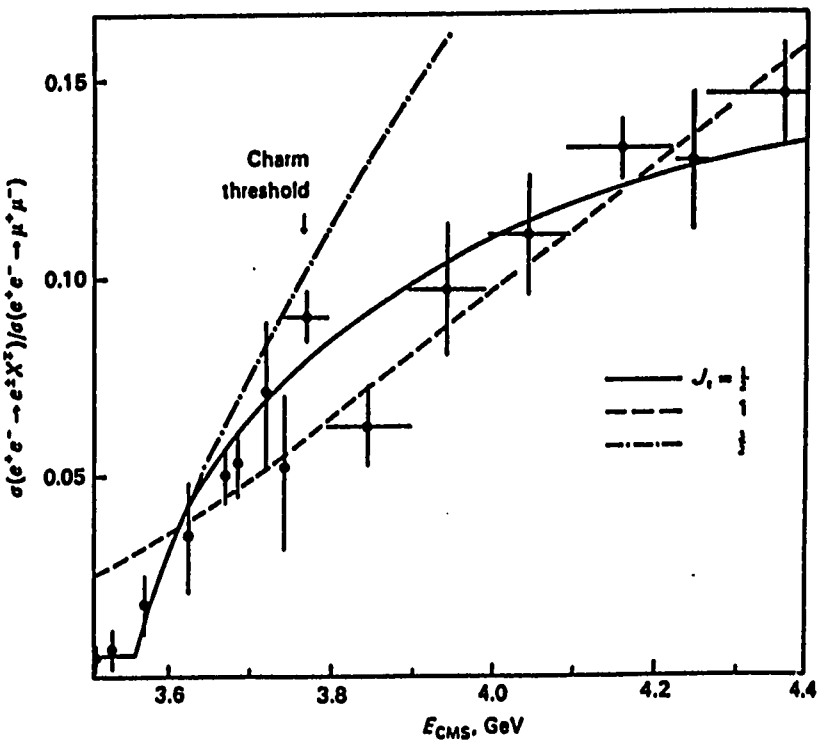


Figure 1.6: Analysis of $\tau$ lepton production by DELCO collaboration. The data from SPEAR (SLAC) favors spin 1/2 for the $\tau$ [12].

*to understand why muons exist...*", a puzzle that has not yet been resolved.

### Lepton Universality

For the past 15 years, leptonic decays of the $\tau$ have represented the best signature of its production process and have been extensively studied in many experiments. These studies established the global properties of the $\tau$; its mass, spin, coupling constants and its consistency with the V-A theory of weak interactions. However, much remains to be learned about the detailed Lorentz structure of the weak current in $\tau$ decays, and precise measurements of the leptonic decays are needed to address the fundamental question of lepton universality, which implies that the $\tau$ is a sequential lepton (i.e., a heavier version of the electron and muon). Lepton universality requires the couplings to the charged weak current to be the same for all three leptons. Precise

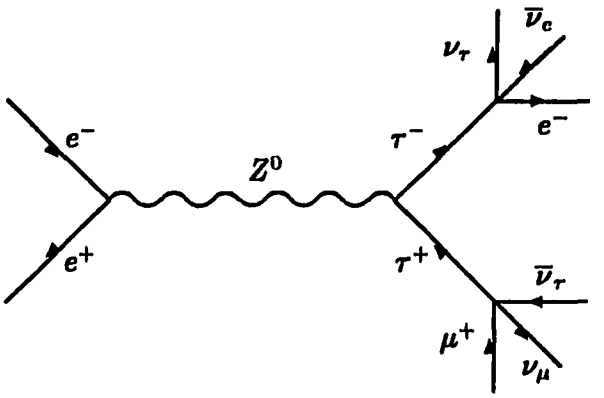


Figure 1.7: Feynman diagram representing $Z^\circ \rightarrow \tau$ decays.

measurements of the $\tau$ decay properties will allow for searches of physics beyond the Standard Model.

The tau leptonic decay process can be described by Feynman diagrams (Figures 1.7 and 1.8), and the corresponding decay width can be expressed as:

$$\Gamma_\tau(\tau \rightarrow l\nu_\tau\nu_l) = \frac{g_\tau g_l m_\tau^5}{384\pi^4} \int d\Omega \int dx\{x^2[3 - 2x \mp (\omega \cdot \hat{p}_l)(2x-1)]\}, \qquad (1.27)$$

where $x = E/E_{max}$ is the scaled energy of the daughter lepton $l$, $\omega$ is the $\tau$ polarization vector, and $\hat{p}_l$ is the unit vector along the direction of the decay lepton. In this case, $m_\tau$ is the mass of the $\tau$, and $g_\tau$ and $g_l$ are the corresponding Fermi coupling constants of the $\tau$ and the final state lepton to the weak current. This expression can be integrated, adding correction factors for the non-zero masses of the final state particles, first order electroweak radiative effects, the finite mass of the $W$ boson [13]

$$\Gamma_\tau(\tau \rightarrow l\nu_\tau\nu_l) = \frac{G_F^2 m_\tau^5}{192\pi^3} f(y) \left[1 + \frac{3}{5}\frac{m_\tau^2}{m_W^2}\right] \left[1 + \frac{\alpha(m_\tau)}{2\pi}(\frac{25}{4} - \pi^2)\right], \qquad (1.28)$$

where $y = (m_l/m_\tau)$, $g_e = g_\mu = g_\tau = G_F$, and

$$f(y) = 1 - 8y + 8y^3 - y^4 - 12y^2 ln(y). \qquad (1.29)$$

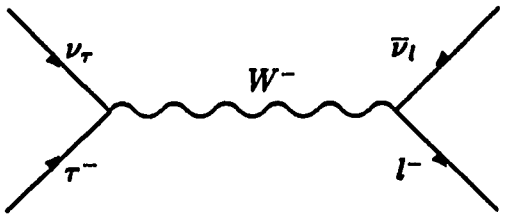


Figure 1.8: Feynman diagram representing the leptonic decays of the $\tau$.

All these effects are quite small compared to the uncertainty on the value of the mass of the $\tau$ ($m_\tau = 1784.1 \pm {}^{2.7}_{3.6}\ MeV$) [8]. Recently, the BES collaboration reported its measurement of $m_\tau$, improving the accuracy by an order of magnitude, $m_\tau = 1776.9 \pm 0.4 \pm 0.3\ MeV$ [14]. The correction factor $f(y)$ can be ignored in the case of the electron ($m_e = 0.511\ MeV$), but not in the case of the tau decay to muon ($m_\mu = 105.66\ MeV$) [15].

The decay process of muon into electron is completely analogous to that of the tau decay. Thus, the corresponding partial decay widths are related. Neglecting the neutrino masses

$$\frac{\Gamma(\tau \to e\bar{\nu}_e\nu_\tau)}{\Gamma(\mu \to e\bar{\nu}_e\nu_\mu)} = \left(\frac{g_\tau}{g_\mu}\right)^2 \cdot \left(\frac{m_\tau}{m_\mu}\right)^5 \cdot \frac{BR(\mu \to e\bar{\nu}_e\nu_\mu)}{BR(\tau \to e\bar{\nu}_e\nu_\tau)}. \tag{1.30}$$

Since $\tau_\mu/\tau_\tau = \Gamma_\tau/\Gamma_\mu$, (1.30) can be expressed in terms of experimentally measured quantities

$$\left(\frac{g_\tau}{g_\mu}\right)^2 = \left(\frac{\tau_\mu}{\tau_\tau}\right) \cdot \left(\frac{m_\mu}{m_\tau}\right)^5 \cdot \frac{BR(\tau \to e\bar{\nu}_e\nu_\tau)}{BR(\mu \to e\bar{\nu}_e\nu_\mu)}, \tag{1.31}$$

where BR is the branching ratio for each of the decay channels.

The LEP experiments recently measured a combined value of $g_\tau/g_\mu = 0.994 \pm 0.010$, supporting lepton universality [16].

**The Z to $\tau$ Decay at LEP**

The full Born differential cross section for the process $e^+e^- \rightarrow \tau^+\tau^-$ [17], including the dependence on the $\tau$ longitudinal polarization, p, is

$$\begin{aligned}\frac{d\sigma}{dcos\theta}(s, cos\theta, p) &= (1+cos^2\theta)F_0(s) + 2cos\theta F_1(s) \\ &\quad + p\cdot[(1+cos^2\theta)F_2(s) + 2cos\theta F_3(s)], \end{aligned} \tag{1.32}$$

with the form factors,

$$F_0(s) = \frac{\pi\alpha^2}{2s}(q_e^2q_\tau^2 + 2Re(\chi(s))q_eq_\tau v_ev_\tau + |\chi(s)|^2(v_e^2+a_e^2)(v_\tau^2+a_\tau^2)), \tag{1.33}$$

$$F_1(s) = \frac{\pi\alpha^2}{2s}(2Re(\chi(s))q_eq_\tau a_ea_\tau + |\chi(s)|^2 2v_ea_e2v_\tau a_\tau), \tag{1.34}$$

$$F_2(s) = \frac{\pi\alpha^2}{2s}(2Re(\chi(s))q_eq_\tau v_ea_\tau + |\chi(s)|^2(v_e^2+a_e^2)2v_\tau a_\tau), \tag{1.35}$$

$$F_3(s) = \frac{\pi\alpha^2}{2s}(2Re(\chi(s))q_eq_\tau a_ev_\tau + |\chi(s)|^2 2v_ea_e(v_\tau^2+a_\tau^2)), \tag{1.36}$$

where $\chi(s)$ is given by (1.22).

The $q_e, v_e, a_e, q_\tau, v_\tau, a_\tau$ are the charges and Z coupling constants of the electron and $\tau$ respectively. The first term in $F_0$ is from the photon exchange, the third term is from the Z exchange, and the middle term is due to $\gamma - Z$ interference. Notice that for $F_1, F_2, F_3$, only Z and interference terms appear. These form factors are directly related to various measurable quantities that lead to the determination of the coupling constants, such as the Born cross-section, $\sigma_{Born}$, the forward-backward asymmetry, $A_{FB}$, the $\tau$-polarization asymmetry, $P_\tau$, and the $\tau$-polarization forward-backward asymmetry, $A_{pol}^{FB}$:

$$\sigma_{Born}(s) = \frac{8}{3}F_0(s), \tag{1.37}$$

$$A_{FB}(s) = \frac{1}{\sigma_{Born}}[\sigma(cos\theta > 0) - \sigma(cos\theta < 0)] \simeq \frac{3}{4}\frac{2v_e a_e 2v_\tau a_\tau}{(v_e^2 + a_e^2)(v_\tau^2 + a_\tau^2)}, \quad (1.38)$$

$$P_\tau(s) = -\frac{1}{\sigma_{Born}}[\sigma(p > 0) - \sigma(p < 0)] \simeq -\frac{2v_\tau a_\tau}{(v_\tau^2 + a_\tau^2)}, \quad (1.39)$$

$$\begin{aligned} A_{pol}^{FB}(s) &= -\frac{1}{\sigma_{Born}}[\sigma(cos\theta > 0, p > 0) - \sigma(cos\theta > 0, p < 0) \quad (1.40) \\ &\quad -\sigma(cos\theta < 0, p > 0) - \sigma(cos\theta < 0, p < 0)] \simeq -\frac{3}{4}\frac{2v_e a_e}{(v_e^2 + a_e^2)}, \end{aligned}$$

where the final approximation is taken at the Z peak, excluding $\gamma$ exchange.

## Motivation, Overview and Previous Experimental Work

In the nearly two decades since the discovery of the $\tau$ lepton, much has been learned about it. All the experimental results so far indicate the $\tau$ is a sequential lepton, having the same form of interaction as the electron and muon, and the same universal coupling constant. In spite of all this success, there are some important areas about properties of the $\tau$ lepton where little experimental data is available.

Far above the production threshold, the helicities of $\tau^+$ and $\tau^-$ prefer to be opposite to each other. Since the helicities of $\tau^+$ and $\tau^-$ are strongly correlated in the production, one expects that the helicities of the decay products of $\tau^+$ are strongly correlated to those of the $\tau^-$. Since the $\tau$ decays via weak interactions where parity conservation is violated maximally ($W^\pm$ exchange), the angular distribution of the daughter particles depends on the helicity of the parent $\tau$. Therefore, a study of the decay distribution of the daughter particles is a direct probe of the spin properties of the parent $\tau$.

The difference in the coupling of the $Z^\circ$ to positive and negative helicity $\tau^\pm$ gives rise to a polarization effect. The $\tau$ polarization can be determined from the angular distributions of its decay products in the $\tau$ rest frame. In practice, a transformation from the rest frame to the laboratory frame is performed, and laboratory frame distributions, such as energy and momentum, are used to measure the polarization.

As shown in (1.39), the average polarization asymmetry of the $\tau$ depends only on the ratio of the axial-vector and vector couplings near the $Z^0$ resonance. Since $g_V$ is linear in $sin^2\theta_W$, the $\tau$ polarization measurement offers the unique possibility of determining the degree of V-A mixing in neutral weak current interactions. On the other hand, $P_\tau$ has to be measured via the decay distributions of each $\tau$ decay mode, which results in a substantial loss of statistics. Furthermore, systematic uncertainties arising from decay mode misidentification and background from other leptonic decays of the $Z^0$ can be significant.

Since the polarization measurement uses the properties of decay distributions, it cannot be done on the two processes, $e^+e^- \rightarrow Z^0 \rightarrow e^+e^-$ or $e^+e^- \rightarrow Z^0 \rightarrow \mu^+\mu^-$, since these two processes are, by definition, monochromatic at the $Z^0$ pole (the final states occur at $E_{beam}$), and the final states are either stable (the electron) or have long mean life at LEP energies (the muon), so the decay distributions of these processes are not available for studies. For these two leptonic channels, only the forward-backward asymmetry, $A_{FB}$, can be measured.

The forward-backward asymmetry, $A_{FB}$, is easier to measure and statistically richer than $P_\tau$, but it has the disadvantage of depending on the initial state electron coupling to the $Z^0$, as well as on the $\tau$ coupling to the $Z^0$, thus being less sensitive to the $\tau - Z^0$ coupling.

Assuming a pure V-A charged weak current interaction, we obtain

$$\frac{v_\tau}{a_\tau} = 1 - 4 \cdot sin^2\theta_W. \tag{1.41}$$

Furthermore, assuming lepton universality and observing that $v_\tau/a_\tau \ll 1$, the following expressions are valid at the peak of the $Z^0$ resonance:

$$P_\tau \simeq -2(v/a) = -2(1 - 4 \cdot sin^2\theta_W), \tag{1.42}$$

$$A_{pol}^{FB} \simeq -\frac{3}{2}(v/a) = -\frac{3}{2}(1 - 4 \cdot sin^2\theta_W), \tag{1.43}$$

$$A_{FB} \simeq 3(v/a)^2 = 3(1 - 4 \cdot sin^2\theta_W)^2. \tag{1.44}$$

The corresponding errors on the weak mixing angle are

$$\Delta sin^2\theta_W \simeq \Delta P_\tau/8, \tag{1.45}$$

$$\Delta sin^2\theta_W \simeq \Delta A_{pol}^{FB}/6, \tag{1.46}$$

$$\Delta sin^2\theta_W \simeq \Delta A_{FB}^{-1/2}/8\sqrt{3}. \tag{1.47}$$

Thus, although $P_\tau$ is more difficult to measure than $A_{FB}$, it is a more sensitive measurement of the weak mixing angle than the other variables. Figures 1.9 and 1.10 illustrate the dependence of $A_{FB}$ and $P_\tau$ on the center of mass energy for different values of $sin^2\theta_W$.

In principle, it is simpler to perform a polarization measurement at energies below the $Z^\circ$ resonance, for example, at PEP ($\sqrt{s} = 36\ GeV$) and PETRA ($\sqrt{s} = 44\ GeV$), since one can then safely ignore the $Z^\circ$ exchange term in the Born cross-section. However, since the differential Born cross-section $\propto s^{-1}$ for the photon exchange and the $\gamma - Z$ interference term, very few events are recorded at intermediate energies. In addition, the polarization measurement away from the $Z^\circ$ pole is not very sensitive to different values of $sin^2\theta_W$ (Figure 1.10). In this regard, LEP provides the ideal high statistics environment needed for polarization studies at $\sqrt{s} \simeq 91\ GeV$, the $Z^\circ$ resonance.

At LEP, about 70,000 tau pairs have been collected during the 1990 and 1991 runs by the four detector groups (ALEPH, DELPHI, L3 and OPAL), allowing for a substantial improvement on the tau polarization measurement and on the electroweak parameter $sin^2\theta_W$. Table 1.4 shows the results obtained by each of the experiments. All experiments report final 90 results. OPAL adds a partial 91 data set, and L3 and ALEPH incorporate preliminary 91 results.

The combined LEP polarization value is $P_\tau = -0.138 \pm 0.040$.

Rewriting (1.42), we obtain

$$sin^2\theta_W = \frac{1}{4} + \frac{P_\tau}{8}, \tag{1.48}$$

which yields $\sin^2\theta_W = 0.2328 \pm 0.0050$ and $v_\tau/a_\tau = 0.069 \pm 0.020$.

In addition, by using the expression

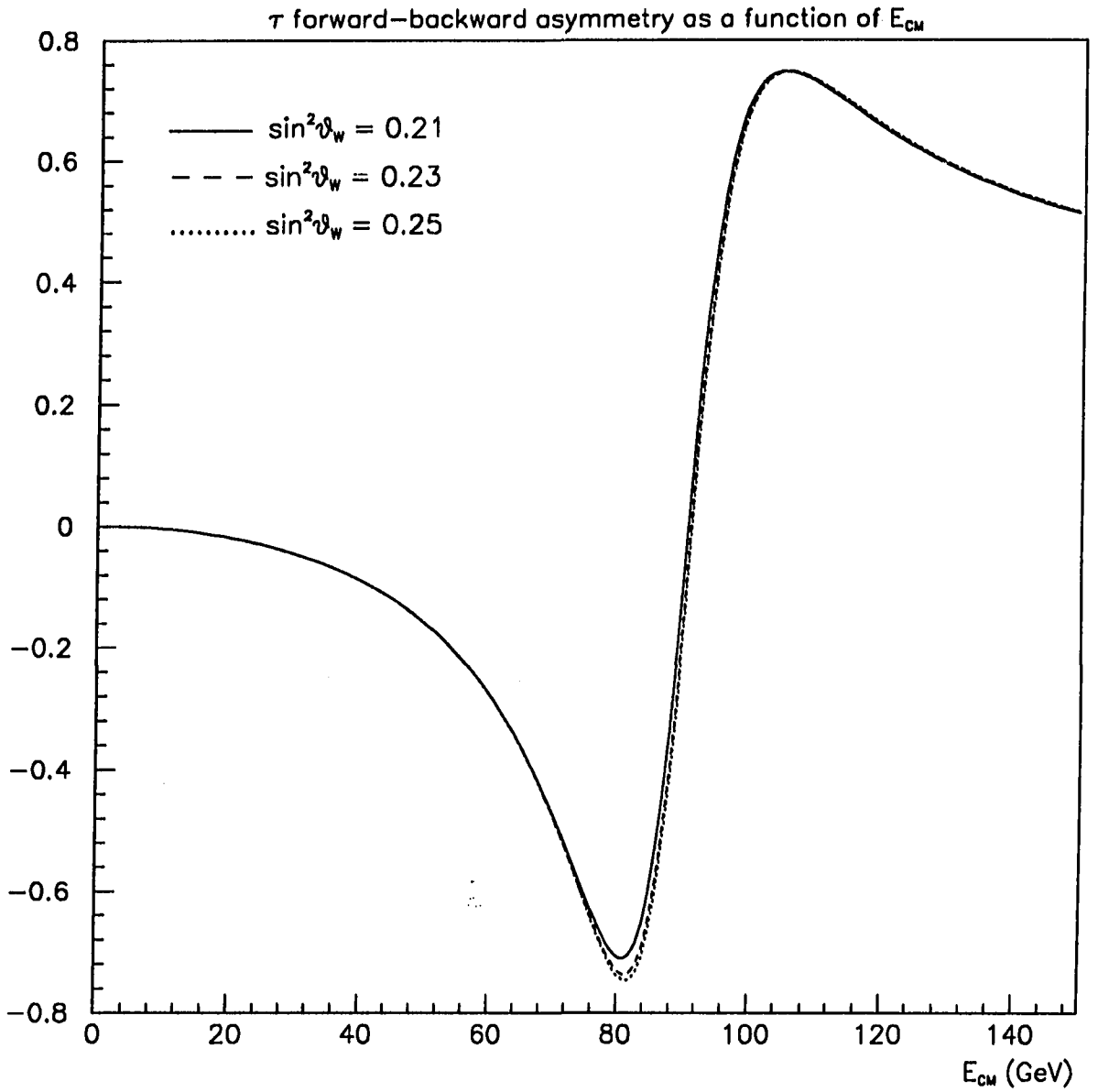


**Figure 1.9:** $A_{FB}$ **as a function of** $E_{CM}$ **for different values of** $sin^2\theta_W$.

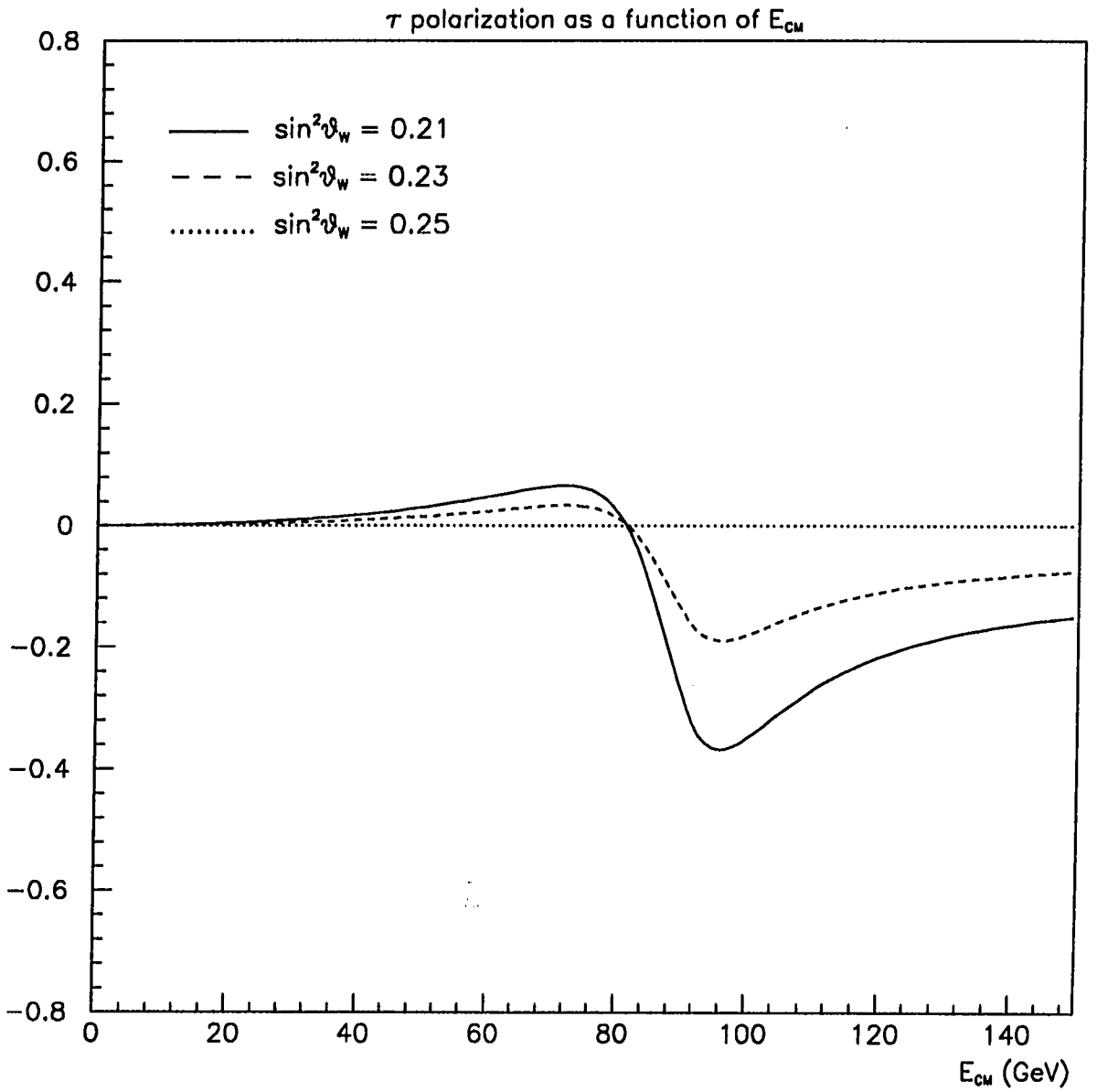


**Figure 1.10:** $P_\tau$ as a function of $E_{CM}$ for different values of $sin^2\theta_W$.

Table 1.4: LEP measurements of $P_\tau$.

| Decay Mode | ALEPH | DELPHI |
|---|---|---|
| $e^-\bar{\nu}_e\nu_\tau$ | $-0.152 \pm 0.090 \pm 0.061$ | $-0.12 \pm 0.22 \pm 0.08$ |
| $\mu^-\bar{\nu}_\mu\nu_\tau$ | $-0.226 \pm 0.074 \pm 0.037$ | $-0.05 \pm 0.18 \pm 0.07$ |
| $\pi^-(K)\nu_\tau$ | $-0.107 \pm 0.038 \pm 0.024$ | $-0.35 \pm 0.11 \pm 0.07$ |
| $\rho^-\nu_\tau$ | $-0.144 \pm 0.037 \pm 0.046$ | $-0.24 \pm 0.09 \pm 0.07$ |
| $a_1\nu_\tau$ | $-0.150 \pm 0.150 \pm 0.070$ | – |
| **Combined result** | $-0.137 \pm 0.031$ | $-0.24 \pm 0.07$ |
| $v_\tau/a_\tau$ | $0.069 \pm 0.016$ | $0.122 \pm 0.036$ |
| **Decay Mode** | **L3** | **OPAL** |
| $e^-\bar{\nu}_e\nu_\tau$ | $-0.078 \pm 0.116 \pm 0.072$ | $-0.03 \pm 0.10 \pm 0.08$ |
| $\mu^-\bar{\nu}_\mu\nu_\tau$ | $-0.108 \pm 0.117 \pm 0.059$ | $-0.10 \pm 0.11 \pm 0.10$ |
| $\pi^-(K)\nu_\tau$ | $-0.147 \pm 0.056 \pm 0.048$ | $-0.04 \pm 0.08 \pm 0.07$ |
| **Combined result** | $-0.127 \pm 0.058$ | $-0.03 \pm 0.08$ |
| $v_\tau/a_\tau$ | $0.064 \pm 0.029$ | $0.015 \pm 0.040$ |

$$\Gamma_{Z\longrightarrow\tau\tau} = \frac{1}{64\pi^2 M_Z}\int \overline{|\Re|}^2 d\Omega = \frac{G_F M_Z^3}{6\sqrt{2}\pi}(v_\tau^2 + a_\tau^2), \tag{1.49}$$

one is able to separate the two constants. From the combined 1990 and 1991 data from all four LEP experiments, one obtains $\Gamma_{\tau\tau} = 82.8 \pm 1.0\ MeV$, and therefore,

$$v_\tau = -0.034 \pm 0.009, \qquad a_\tau = -0.498 \pm 0.003, \tag{1.50}$$

all in very good agreement with world averages. LEP results have improved the accuracy of these electroweak parameters by more than an order of magnitude when compared with previous results taken at lower energy, after only 2 full years of operation [18].

# CHAPTER 2. THE DELPHI DETECTOR

DELPHI, a Detector with Lepton, Photon, and Hadron Identification, is a detector operating at the LEP (Large Electron Positron) collider at CERN. It is designed as a general purpose detector with special emphasis on powerful particle identification, equipped with Ring Imaging Cherenkov counters (RICH), 3-dimensional information with high-granularity in most of its components and precise vertex determination (Figures 2.1, 2.2 and 2.3). DELPHI currently takes data at or near the total center of mass energy of 91.2 $GeV$ at typical luminosities of $4 \times 10^{30}\ cm^{-2}{}_s{}^{-1}$.

In the following description of the detector, we shall use a coordinate system with the z-axis parallel to the beam, radius R and azimuth $\phi$ in the plane perpendicular to it and polar angle $\theta$ (= 0 along z).

For the purpose of explanation of this analysis, only the relevant detectors will be described in some detail. In particular, the detectors in the barrel region will be emphasized ($42^\circ < \theta < 138^\circ$). A more complete description of the detector can be found elsewhere [19].

DELPHI is installed in a cavern 100 m below ground. The ensemble consists of a cylindrical section, the barrel, and two end-caps, which can be axially opened by $2.8m$ to allow access to the various detectors. Three to four-story huts on both sides of the detector house the read-out and acquisition electronics, the 14 subdetector computers, gas distribution and cryogenic systems, and power supplies for the superconducting magnet. An optical data link sends the compressed data to the main data acquisition computer and control center located in a surface building.

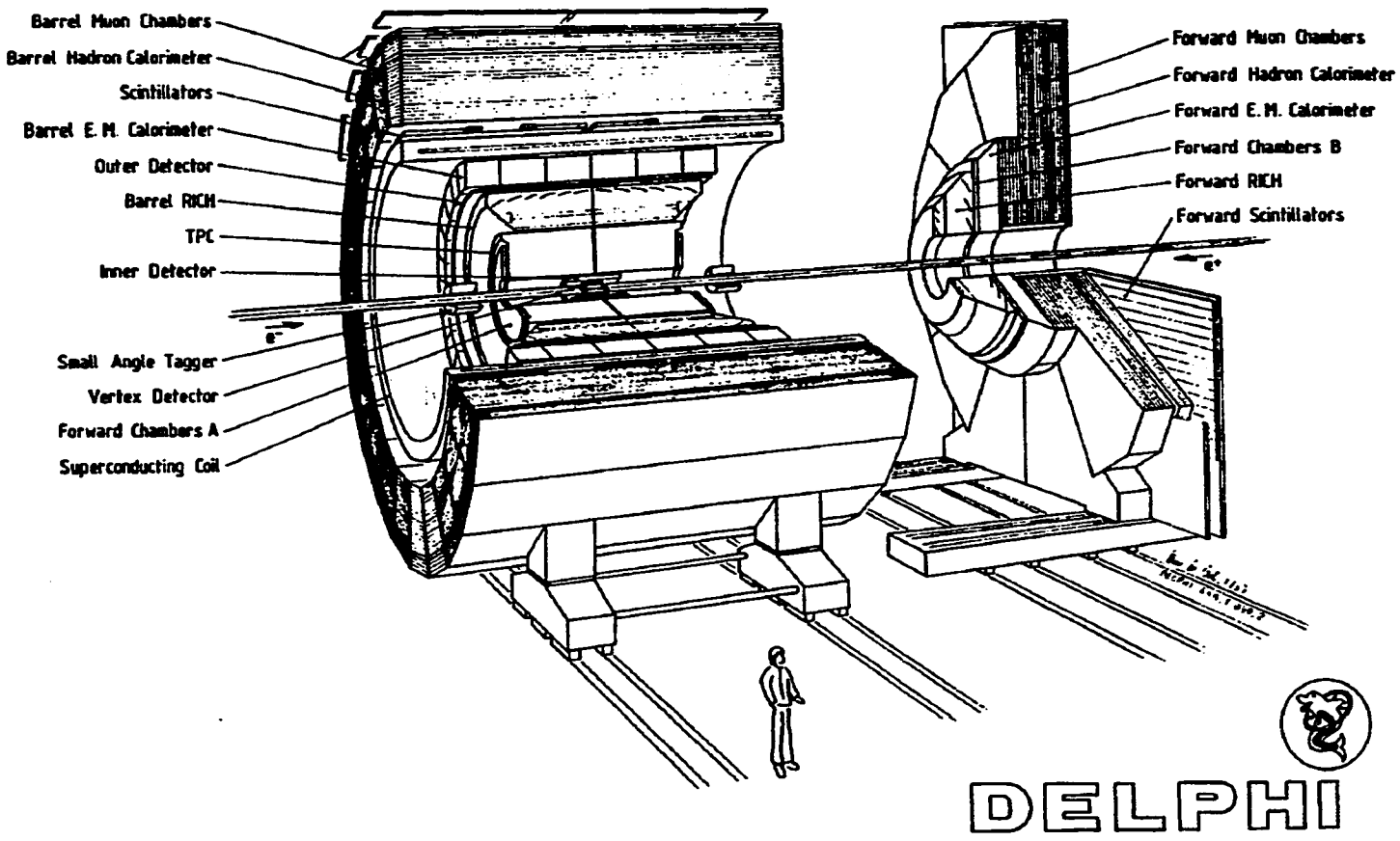


Figure 2.1: A general view of the DELPHI detector.

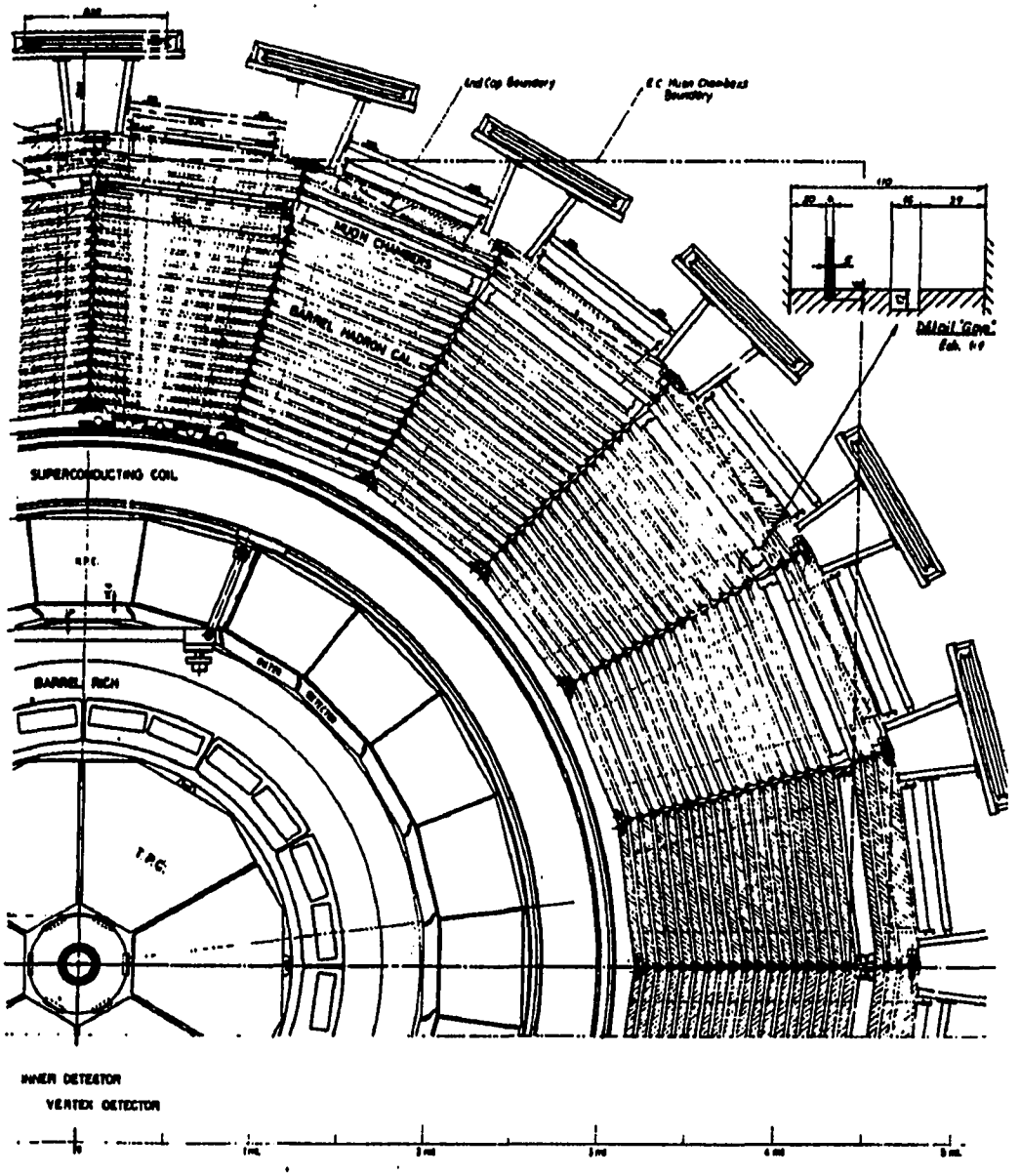


Figure 2.2: A cross-sectional view of the barrel region of DELPHI.

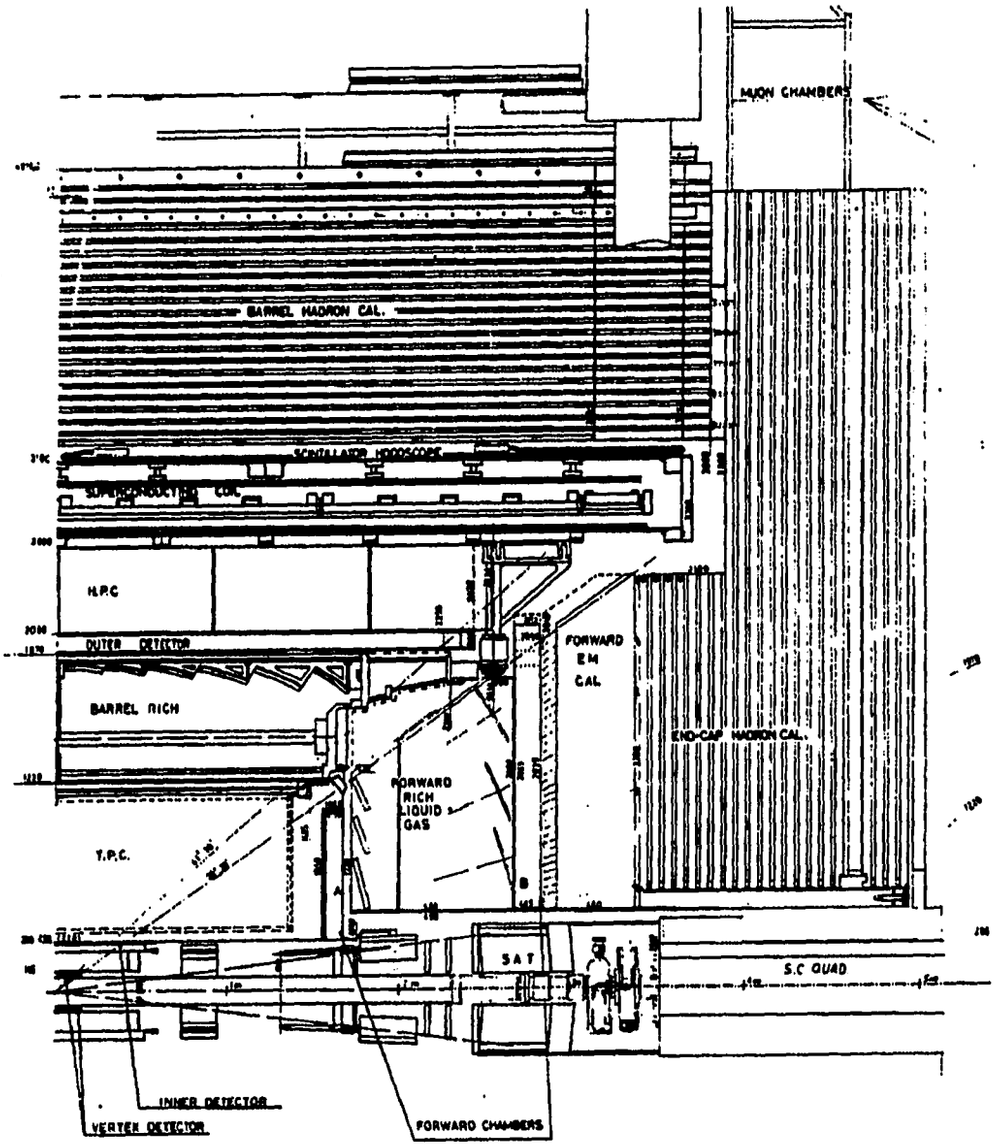


Figure 2.3: A longitudinal view of the DELPHI detector.

## The Solenoid

The superconducting solenoid has a length of 7.4 $m$ and an inner diameter of 5.2 $m$. An input current of 5000 $A$ produces a 1.2 T field. The superconducting cable is made from 17 twisted wires clad in high purity aluminum, and the wires contain 300 $Nb-Ti$ filaments embedded in a copper matrix, forming a flat conductor and wound onto the aluminum support cylinder. The cooling system for the magnet is done by forced flow of liquid helium at 4.5 $K$, which provides 150 $W$ of cooling at 4.5 $K$.

The excellent field homogeneity required for the long drift devices is demonstrated by the uniformity of the longitudinal component inside the Time Projection Chamber (a cylindrical structure of length 300 $cm$, with inner and outer radius of 29 and 120 $cm$, respectively), $12334 \pm \frac{1}{10}$ Gauss, indicating a small axial asymmetry. Negligible azimuthal variation and a radial component $< 5$ Gauss have been measured.

## Tracking

The tracking at DELPHI is performed by the Microvertex detector (MVD), the Inner Detector (ID), the Time Projection Chamber (TPC), and the Outer Detector (OD). For the data in this analysis, track fitting was done with the 2-layer MVD, the ID, the TPC, and the OD. The OD is located between the Barrel Ring Imaging Cerenkov Counter (BRICH) and the High Density Projection Chamber (HPC), the barrel electromagnetic calorimeter.

### The Microvertex Detector

The Microvertex Detector (MVD) is made up of three concentric shells of $Si$-strip detectors at average radii of 6.3, 9.0 and 11.0 $cm$ respectively, giving full azimuthal coverage in the polar angular region $43^\circ < \theta < 137^\circ$ and covering the central region over a length of 24.0 $cm$. The principal objective of this detector is to provide maximum $R\phi$ resolution for the identification of secondary vertices needed for the study of heavy flavor physics. Each layer has 24 sectors with a $10 - 15\%$ overlap in $\phi$, which are subdivided along the $z$-axis into 4 strips. Each strip is 300 $\mu m$ thick

and has a sensitive area of 59 $mm$ × 25.6 $mm$. The strips are paralled to the $z$-axis and have a pitch of 25 $\mu m$ with every second strip read out by capacitive pick-up at the ends. The intrinsic $R\phi$ resolution of the MVD is 6 $\mu m$, and its single point resolution is 8 $\mu m$ [20].

Laboratory measurements gave a signal:noise ratio of 15 : 1 for a minimum ionizing particle (m.i.p.).

### The Inner Detector

The Inner Detector (ID) provides high redundancy for vertex reconstruction and trigger information. It consists of 2 concentric detectors, a jet chamber and a MWPC with 5 cylindrical sublayers. The radiation thickness of the whole detector at $\theta = 90^{\circ}$ is only $0.0375 X_0$.

The jet chamber section, at a radius of 11.8 $cm$, has 24 azimuthal sectors, each providing up to 24 $R\phi$ points per track. The gas mixture ($CO_2/C_4H_{10}/C_3H_7OH$ : 94.85%/4.5%/0.65%), field wire grids on both sides of the sense wire planes and drift field (varying from 1 to 2 $kV/cm$) were chosen to produce a drift velocity proportional to $R$. Thus, the trigger information for radial tracks occur in a narrow time window ($\sim$ 10 $ns$).

The five outer sublayers consist of sense wires 8 $mm$ apart and interspaced with field wires. Each sublayer is 8 $mm$ thick and has circular cathode strips on the inner wall. This system is filled with a $Ar/CO_2$(70/30%) gas mixture.

The average single wire resolution of $\sigma_{R\phi}$ = 90 $\mu m$ in the jet chamber and $\sigma_z$ < 1 $mm$ was achieved during the initial running period in 1989. The trigger efficiency for the jet chamber is > 90% for jet events, while the five outer layers achieved a trigger efficiency > 95% for single tracks.

### The Time Projection Chamber

The TPC covers the polar region $20^{\circ} < \theta < 160^{\circ}$ and is the principal tracking device in DELPHI, since pattern recognition starts from its information. The TPC has an inner radius of 29 $cm$ and an outer radius of 120 $cm$. It is divided into two half-cylinders (each 150 $cm$ long) with respect to a plane perpendicular to the

beam direction at the interaction point. The field is always aligned so that ionization drifts along the beam axis, away from the interaction point to an endplate at each outer end of the half-cylinders. The TPC provides 3 dimensional spatial information and energy loss per unit distance (dE/dX). Charged particles which traverse the TPC sensitive volume ionize the gas. The liberated electrons are caused to drift towards the endplates by parallel $E$ and $B$ fields, to minimize transverse diffusion. The circular pads provide $R-\phi$ spatial information, while the track's z-coordinate is determined from the measured drift time and known drift velocity. The sense wire pulses provide dE/dX information. The two endplates of the TPC are each divided into 6 sectors with 192 sense wires 4 $mm$ apart and 16 circular pad rows at constant spacing. A grid is placed 8 $mm$ in front of the cathode plane. The z-axis of the TPC is parallel to the beam axis, and the cylindrical volume is filled with an $Ar/CH_4(80/20\%)$ gas mixture. With a drift field of 150 $V/m$, the drift velocity is $v_d = 66.94 \pm 0.07\ mm/\mu s$ at $T = 22^{\circ}\ C$.

The TPC operates at 1 $atm$ pressure. The reduced pressure degrades minimally the $dE/dX$ information and momentum resolution, while allowing for lower radiation thickness, faster response and reduced transverse diffusion. The $dE/dX$ resolution is 6.2% for muons at 45 $GeV$ and 7.5% for pions between 280 and 400 $MeV$. Below 8 $GeV$, $e/\pi$ separation is still possible. In addition, $\sigma_{R\phi} = 180 - 280\ \mu m$ (position dependent), $\sigma_z < 0.9\ mm$, and the two-track separation resolution is 1.5 $cm$.

With present luminosities, background is very low. Dark current is about 10 nA/sector and amounts to less than 20 hits from synchroton radiation per beam crossing in the full TPC.

### The Outer Detector

The Outer Detector (OD) provides fast trigger information in both $R\phi$ and $z$, and improves the momentum resolution by a factor of $> 5$ for energetic particles, because of its position outside the BRICH.

The OD is divided in 24 modules, 4.7 $m$ long and each consisting of 145 drift tubes in 5 staggered layers, to provide full azimuthal coverage. The drift tubes are operated in limited streamer mode. All layers provide $R\phi$ information, though only the middle three layers provide fast $z$ information by relative timing of signals from

both ends.

The resolutions of the OD are: $\sigma_{R\phi} = 110\ \mu m$ and $\sigma_Z = 4.4\ cm$, a improvement by a factor of $2-3$ over the original specifications, which allows the determination of track charge, up to the highest momenta, from OD track elements alone.

### Combined Tracking

Track information is obtained from all these independent tracking devices, and the successful combination of their information is essential for the trigger, the vertex and general pattern reconstruction, especially for high momentum particles [19]. The momentum resolution for muons at 45 $GeV$ during the 1992 run was $\Delta p/p = 3.5\%$, using the 2-layer MVD, the ID, the TPC, and the OD. Further improvements are expected with the upgraded 3-layer MVD and a better understanding of the tracking detectors.

### The Barrel Muon Detector

The Barrel Muon Detector (MUB) is DELPHI's outermost subdetector, placed outside of the calorimeters. Thus, with the exception of muons and neutrinos, most particles are absorbed in the calorimeters' converter material before reaching the MUB.

The MUB is composed of 2 layers. The first layer of $2 \times 24$ planks is inserted into the return yoke of the solenoid, after 90 $cm$ of iron and contains 3 staggered drift-chamber planes. The second layer is mounted on the outside of the yoke, behind an additional 20 $cm$ of iron, with overlapping planks to provide clearance for cables and pipes, each containing 2 staggered drift-chamber planes. The sensitive region of the majority of the chambers is 3.65 $m$ in length. Except for the third chamber of the first layer, which is regarded as a spare, all other chambers are read out, thus providing full azimuthal coverage in the angular region $51^\circ < \theta < 129^\circ$.

Each plank is 20.8 $cm$ wide and 2.6 $cm$ high, with a single anode wire in the center. Cathode $Cu$-strips are glued on the plastic sheets that coat the upper and lower inner walls of each plank. The cross section for drifting is $20 \times 1.6\ cm^2$. The drift chambers operate in the proportional mode, with a $Ar/CH_4/CO_2$(85.5/8.5/6%)

gas mixture.

High overall muon detection efficiency ($\sim 95\%$), with $\sigma_{R\phi} = 4\,mm$ and $\sigma_Z \sim 2.5$ $cm$ for extrapolated tracks, has been achieved.

## Calorimetry

Calorimetry in the barrel region in DELPHI is made up of two independent detectors: the High Density Projection Chamber (HPC) and the Hadronic Calorimeter (HCAL). The HPC is located behind the OD and in front of the solenoid, while the HCAL is placed behind the Time of Fligh Counters (TOF) and the solenoid.

### The High Density Projection Chamber

The High Density Projection Chamber (HPC) is the first large-scale application of the time projection principle to calorimetry, providing three-dimensional information of the charge distribution in electromagnetic showers, with very high granularity in all dimensions. Together with precise tracking, the HPC allows for the detection and separation of electromagnetic showers in the dense event topologies encountered at LEP.

The HPC consists of 144 modules split into two half-cylinders with respect to a plane perpendicular to the z-axis (beam axis) and centered at $\theta = 90^\circ$. Each half-cylinder has 3 azimuthal rings (in the z-direction), each containing 24 modules. The total length of the HPC is 505 $cm$, with inner radius of 208 $cm$ and outer radius of 260 $cm$. A 1 $cm$ gap between modules in both $z$ and $\phi$ and a gap of 7 $cm$ at $z = 0$ between the two halves limit somewhat the shower containment in the detector. The HPC covers the angular region $43^\circ < \theta < 137^\circ$. Including edge effects and the gaps between modules, the HPC has a sensitive region that covers approximately 62% of the spherical surface area at $R = 208$ $cm$, centered around the interaction region.

Each HPC module contains 41 lead wire converter layers separated by 8 $mm$ drift gaps filled with an $Ar/CH_4$ gas (except for the trigger gap). Resistor chains soldered to the lead wires form a voltage divider network and provide a uniform electric field parallel to the beam axis, with a voltage gradient of about 100 $V/m$ between adjacent wires. The precisely aligned $\boldsymbol{E}$ and $\boldsymbol{B}$ fields enhance the drifting process while

minimizing transverse diffusion. In the HPC, drift distance varies between 65 *cm* and 85 *cm* depending on the module. A correction due to the measured attenuation length of $\sim$ 350 *cm* has been applied to the data.

For triggering purposes, a plane of scintillators has been inserted into one of the sampling gaps near the shower maximum ($4.5X_0$). Light guides connect the readout to the PMT's located just outside the cryostat, in a region of low $\boldsymbol{B}$ field.

In the HPC, the electromagnetic showers develop as follows: incoming particles bremsstrahlung in the lead structure, and the resulting photons then pair- produce. The electron-positron pair in turn bremsstrahlung, and the whole process repeats itself until the energy of the remaining daughter particles is below the threshold for further interaction with matter. The charged particles produced in this shower are then drifted out to a single proportional wire plane at one end of a HPC module . The charge collected by the anode wire induces a signal in one of the pads, which is amplified, shaped and then digitized. The drift origin in $z$ is obtained from the known drift velocity ($v_d \simeq 5.75\ cm/\mu s$) and the measured drift time. Flash analog-to- digital converters (FADC's) operating at 15 $MHz$ ($\sim$ 67 $ns$) sample the drifting charge 256 times over the $\sim$ 85 *cm* drift length. Therefore, the sample position relative to a signal synchronized with the beam cross-over (BCO) clock gives a measurement of the drift time.

The electronic readout system provide excellent tail suppresion originating from gas amplification effects (less than 0.1% of peak height after 1 $\mu s$) and baseline stability. A zero suppression algorithm is implemented in the electronic hardware to eliminate random hits. This results in an average data transfer rate of only 14 kbytes per hadronic event at LEP for the entire HPC. The wire and pad positions provide $x - y$ information. With 18,432 electronic channels and nine readout layers ($18X_0$), the HPC granularity of 3.85 *mm* along $z$ and $1^\circ$ in azimuth has been achieved in 1992. In addition, the dynamical range of 800 : 1 of the detector is capable of coping with electromagnetic showers of up to 50 $GeV$, while remaining fully sensitive to minimum ionizing particles (m.i.p.'s).

The angular resolution of the HPC with vertex constraints is $(36/\sqrt{E} \oplus 2.5)$ *mrad* in $\theta$ and $(97/\sqrt{E} \oplus 10)$ *mrad* in $\phi$ for fixed $\theta$ and $\phi$. Overall energy resolution is approximately $(25/\sqrt{E} \oplus 5)$ %, which translates into an energy resolution of $\sim$ 6%

for Bhabhas at 45 $GeV$.

### The Hadron Calorimeter

The Hadron Calorimeter (HCAL) is a sampling gas detector imbedded in the solenoid return yoke. It measures the energy and position of hadronic showers and muons that pass through the inner regions of DELPHI with minor interactions.

The barrel part covers the angular region $42.6^\circ < \theta < 137.4^\circ$ and is segmented into 24 (each 7.6 $m$ long) modules with trapezoidal cross-section, each with 20 sampling layers of limited streamer mode tubes inserted into 2 $cm$ gaps between the 5 $cm$ iron plates. The detector tubes ($\sim$ 350 $cm$ long and $\sim$ 8.5 $cm$ wide) are glued on the readout boards. The gas composition in the HCAL is $Ar/CO_2$/isobutane (10/60/30%). With this gas mixture, an average of 10 $pC$ is induced on the readout boards with a $HV$ of 3.92 $kV$.

The detector plane consists of wire chambers with 8 cells of $9 \times 9$ $mm^2$ with one anode wire in each. The copper-clad readout boards are segmented into pads where the induced charges are picked up. In the barrel region, a set of pads in 5 neighboring layers covering an angular region $\Delta\phi = 3.75^\circ$ and $\Delta\theta = 2.96^\circ$ form a tower. The dimensions of a typical tower in the barrel are $25 \times 25 \times 35$ $cm^3$. The towers have a "pointing" geometry, that is, the towers point to the nominal interaction point.

The performance of the detector has been studied using dimuon and hadronic decays of the $Z^\circ$. Good linearity up 10 $GeV$ has been established, with an energy resolution of $120\%/\sqrt{E}$. The HCAL efficiency of single muon detection from MUB identified dimuon events is approximately 80%.

## Luminosity Monitoring

The main luminosity monitoring device in DELPHI is the Small Angle Tagger (SAT), which consists of two-arm system of cylindrical detectors enclosing the beam pipe. The SAT is optimized for luminosity measurements by counting Bhabha events. The two arms are identical and placed symmetrically on each side of the interaction point, covering the range $|z| = 191 - 300$ $cm$. Each arm consists of a calorimeter and a tracker in front.

The SAT calorimeter is made of alternating layers of scintillating fibers (1.0 *mm* thick) and lead sheets (0.9 *mm* thick) aligned parallel to the beam. It covers the angular region $43 < \theta < 135$ *mrad*. Scintillating fibers were chosen because of their good radiation hardness and ease of machining. The sensitive part of the calorimeter has an inner radius of 10 *cm* and an outer radius of 36 *cm*, with $z$-values from 245 *cm* and 285 *cm*. The total thickness of the SAT is $28X_0$.

Behind the calorimeter, the fibres are collected in 144 bunches per half-cylinder and coupled to conical lightguides to circular photodiodes with an 1 $cm^2$ active area. The light guides and electronics cover the last 15 *cm* of the SAT, up to $z = 300$ *cm*. Light collection efficiency is about 70% and diode quantum efficiency is 90% at the peak. A prototype has shown an energy resolution of $11.4\%/\sqrt{E} \oplus 1.2\% \oplus 2.3\%$, where the last term comes from response variations across the detector. The total systematic error on the luminosity determination is estimated to be 1.4%, originating mainly from geometrical uncertainties, energy cuts, Monte Carlo modeling and theory (1%).

The fiducial acceptance of the SAT determines the precision in the theoretical calculation of the Bhabha cross-section, and hence the luminosity. Since the trackers are not fully operational, a circular "lead mask" was placed in front of one of the calorimeters to precisely define the fiducial acceptance of the SAT. It covers the inner 3 *cm* of the calorimeter acceptance, and the outer surface points back to the nominal interaction region. In addition, a "$\phi$ mask" was also installed to cover $\pm 15^\circ$ around the the 2 *cm* vertical gap between the two calorimeter half-barrels. The radius of the "lead mask" and the width of the "$\phi$ mask" are each known to better than 0.1 *mm*. The thickness of the mask is $12X_0$, reducing the energy deposited in the calorimeter by an average of 85%. This resulted in a clear separation between electrons passing through the mask and electrons showering in the SAT calorimeter, thus defining accurately the fiducial acceptance of the SAT. The uncertainty in the luminosity due to the fiducial acceptance is only 0.4%.

## Trigger

DELPHI foresees a four-level trigger system to cope with the high luminosity and background rates in LEP. However, during the first two full years of low luminosity operation, only first and second-level triggers were implemented. For the 1992-1993 periods, various components of the third-level trigger are being tested and incorporated to the general trigger system.

In the four-level design, the first two levels are synchronous with the BCO, which occurs every 22 $\mu s$ for 4-bunch mode at LEP. Beginning in 1993, LEP will run continuously in 8-bunch mode, so the BCO will occur every 11 $\mu s$.

The trigger decisions for the first and second-level triggers are taken 3 and 40 $\mu s$ after the BCO, respectively, while the third and fourth-level triggers are asynchronous with the BCO, and the processing time is considerably longer (30 and 300 $ms$, respectively).

The first and second-level central triggers are made up of subtriggers from individual detectors. The main trigger components in the barrel are "track", "muon", "electromagnetic energy" and "hadronic energy". These two trigger levels are both hardware-based, designed in FASTBUS standard, and requiring a logical combination of "AND" and "OR" of the detector subtriggers to validate events. The third-level trigger is software-based, and it will be used to reduce the trigger rates to a few hertz in the high luminosity operational phase.

The timing of the first-level trigger is tuned to minimize space charge in the TPC, and the second-level trigger uses information from detectors with long drift times (for example, the HPC). Thus, a loss of one BCO occurs if an event passes the first-level trigger.

With a luminosity of $\sim 4 \times 10^{30}\ cm^{-2}s^{-1}$, typical trigger rates of 500 $Hz$ and 2 $Hz$ have been obtained by the first and second-level trigger, respectively. In addition, trigger efficiencies $> 97\%$ have been achieved routinely.

## Data Acquisition System

The Data Acquisition System (DAS) is based on the FASTBUS standard and is divided in 3 main phases separated by data buffers.

The first phase is hardware-controlled and sychronous with the BCO. The main tasks are to activate the first and second-level triggers and reset the front-end buffers (FEBs) in case of negative trigger decisions. Depending on the detector, it takes 200 $ns$ to 23 $\mu s$ for data to reach the FEBs. The first-level trigger decision takes 3 $\mu s$, and in case of a negative decision, the FEBs are reset, and DAS is ready for the next BCO. If the decision is positive, then the second-level trigger begins, and the decision is taken 39 $\mu s$ after the BCO. If the decision is negative, the system is reset for the next BCO, having lost one BCO in the meantime. If the decision is positive, the data is transferred, and the FEBs are freed and reset, which adds a 3.5 $\mu s$ dead time.

The second phase is software-controlled and asynchronous with the BCO. This main readout phase takes typically 30 $ms$. The main readout phase involves the transfer of the data from the FEB to the Multi Event Buffer (MEB) in two steps. First, FEB data from each FASTBUS module is transferred to the crate event buffer by a Fastbus Intersegment Process (FIP), which performs zero suppresion of background events and electronic noise, formatting and third- level trigger decisions. Second, the data in the various crate event buffers is transferred to the Multi Event Buffer (MEB) for each detector and duplicated in the Spy Event Buffer (SEB) to provide a fast, online data inspection. A set of FIPs named Local Event Supervisors (LES) perform this transfer of data to the VAXes corresponding to each of the detectors. The LES is capable of block transfers at a maximum rate of 20 $Mb/s$.

The third phase is software-controlled and involves the transfer of data from the various MEBs to a single Global Event Buffer (GEB) in the central DAS VAX cluster. This task is handled by a single FIP, the Global Event Supervisor (GES). The global event buffer has a 2 $Mb$ RAM memory. The data is finally transferred for storage on magnetic tape at typical rates of 2 $Hz$.

# CHAPTER 3. POLARIZATION OBSERVABLES

As already discussed previously, the distribution of the $\tau$ decay products serves as a spin analyzer of the parent $\tau$ and gives an unique possibility of determining the $\tau$ polarization through the study of its decay products. At this point, it is appropriate to discuss the different aspects of this measurement in more detail.

## Leptonic Decays

In the $\tau$ rest frame, the decay distribution can be written as [21]

$$\frac{dN}{x^2 d\Omega dx} \propto W_1(x) + P W_2(x) cos\theta, \tag{3.1}$$

where $x = E^{lepton}/E^{lepton}_{max}$ and $\theta$ is the angle between between the $\tau$ polarization and the momentum of the final state charged lepton.

In the Standard Model, neglecting the mass of the lepton and radiative corrections, $W_1$ and $W_2$ can be expressed as [22]

$$W_1 = 3 - 2x, \qquad W_2 = 1 - 2x. \tag{3.2}$$

For a longitudinal polarization, the laboratory frame parameter $x_l = E^l/E^l_{max}$ is related to the $\tau$ rest frame parameter $x$ by a Lorentz boost, $2x_l = x(1 + cos\theta)$.

One may therefore write

$$\frac{dN}{dx_l} \propto \int_{x_l}^{1} 2x[W_1(x) + P\frac{2x_l - x}{x} W_2(x)]dx. \tag{3.3}$$

After normalization and integration, one obtains

$$\frac{1}{N}\frac{dN}{dx_l} = \frac{1}{3}[(5 - 9x_l^2 + 4x_l^3) + P(1 - 9x_l^2 + 8x_l^3)]. \tag{3.4}$$

Therefore, the decay distribution for a 3-body lepton decay is a $3^{rd}$ order polynomial. A fit to the energy decay distribution of electrons and momentum distribution of muons provides a measurement of the polarization in these channels (Figures 3.1 and 3.2).

## Hadronic Decays

The simplest case is a two body decay, $\tau^- \rightarrow \pi^- \nu_\tau$. In the $\tau$ rest frame, the two final state particles are emitted back to back. Since $\nu_\tau$ has a negative helicity, it prefers to be emitted opposite to the direction of the spin of the $\tau^-$. Therefore, the $\pi^-$ prefers to be emitted in the direction of the spin of the $\tau^-$. In this case, we see that $dN/d(cos\theta) \propto 1 \pm cos\theta$, where $\theta$ is the angle between the pion direction and the $\tau$ polarization axis.

Summing over the helicity states, one obtains the angular distribution

$$\frac{dN}{dcos\theta} \propto \frac{1}{2}[1 + Pcos\theta]. \tag{3.5}$$

The Lorentz boost from the $\tau$ rest frame to the laboratory frame produces a simple relation between the angle $\theta$ and the momentum of the pion measured in the laboratory frame:

$$cos\theta = \frac{4p_\pi m_\pi^2 - 2E_{beam}(m_\tau^2 + m_\pi^2)}{(m_\tau^2 - m_\pi^2)\sqrt{4E_{beam}^2 - 4m_\tau^2}} \simeq 2x_\pi - 1, \tag{3.6}$$

where $x_\pi = p_\pi / E_{beam}$ and assuming $(m_\pi/m_\tau)^2 \ll 1$ and $(m_\tau/E_{beam})^2 \ll 1$. The decay distribution in the laboratory frame is

$$\frac{1}{N}\frac{dN}{dx_\pi} = 1 + P(2x_\pi - 1). \tag{3.7}$$

Thus, the pion angular distribution sensitivity to $P_\tau$ in the $\tau$ rest frame is recovered in the laboratory frame (Figure 3.1). A fit to the momentum decay distribution allows a measurement of the longitudinal polarization and of the weak mixing angle in this channel (Figure 3.2).

For multipion final states, the spin of the hadronic system is either $J = 0$ or $J = 1$, and the $G$-parity is $G = P(-1)^J$. For a $2\pi$ final state, Conserved Vector Current (CVC) requires $J^P = 1^-$. For a $3\pi$ final state, one has $J^P = 1^+$ or $0^-$, but the latter is suppressed by PCAC [13,21]. The dominant $2\pi$ and $3\pi$ final states, $\tau^- \rightarrow \rho^-\nu_\tau$ and $\tau^- \rightarrow a_1^-\nu_\tau$, can be treated similarly, but now the spin 1 hadronic system can assume helicity values 0 or $-1$. The decay distribution is then

$$\frac{dN}{dcos\theta} \propto \frac{1}{2}[1 + \alpha P cos\theta], \tag{3.8}$$

where $\alpha$ is given by

$$\alpha = \frac{m_\tau^2 - 2m^2}{m_\tau^2 + 2m^2}. \tag{3.9}$$

One obtains $\alpha_\rho \simeq 0.46$ and $\alpha_{a_1} \simeq 0.12$. Therefore, the sensitivity of the final state angular distribution is greatly reduced.

The sensitivity can be regained by measuring the helicity of the spin 1 hadron through decay distribution of the $\rho$ or $a_1$ in the $\tau$ rest frame and the decay distribution of the hadronic system into final state pions [23,24].

The first angle, $\rho$, can be calculated in a similar manner as for the $\tau^- \rightarrow \pi^-\nu_\tau$ decay, without ignoring the mass of the $\rho$ this time,

$$cos\rho = \frac{2x_\rho - 1 - m_\rho^2/m_\tau^2}{1 - m_\rho^2/m_\tau^2}, \tag{3.10}$$

where $x_\rho = E_\rho/E_{beam} = (E_\pi + E_{\pi^0})/E_{beam}$.

A second angle $\psi$, which characterizes the decay distribution of the hadron into final state pions can be expressed in laboratory observables. For the $\rho$, this is the decay angle of the $2\pi$ system with respect to the $\rho$ line of flight, and is given in terms of the energies of the two pions,

$$cos\psi = \frac{m_\rho}{\sqrt{m_\rho^2 - 4m_\tau^2}} \frac{E_\pi - E_{\pi^0}}{|p_\pi + p_{\pi^0}|}. \tag{3.11}$$

Thus, one regains the sensitivity in multipion final states by performing a two-dimensional fit to the $(cos\rho, cos\psi)$ distributions.

## Sensitivity in Various Channels

For the purpose of understanding the various factors involved in this analysis, it is interesting to compare the sensitivity of the various channels to $P_\tau$. The $P_\tau$ dependence for all decay channels can be expressed most generally as [21]

$$W(x) = f(x) + P_\tau g(x), \tag{3.12}$$

with $\int f(x)dx = 1$ and $\int g(x)dx = 0$, where $f$ and $g$ are functions of a normalized variable $x$ (for example, energy). Fitting this distribution, the error on $P$ is asymptotically given by

$$\Delta P = \frac{1}{\sqrt{N}} \left[ \int \frac{g^2}{f + P_\tau g} dx \right]^{-\frac{1}{2}} = \frac{1}{S\sqrt{N}}, \tag{3.13}$$

where $N$ is the number of events contained in the distribution and $S$ is the ideal sensitivity.

For a given decay mode $Y$, the corresponding expression is

$$\Delta(P_\tau)_Y = \frac{1}{S_Y \sqrt{B_Y N_\tau}}, \tag{3.14}$$

where $B_Y$ is the branching ratio of the decay mode $Y$.

Two interesting observations can be made regarding the sensitivity of the various decay modes. First, the error on $P_\tau$ using all channels improves by a factor of almost two when compared with $\tau^- \to \pi^- \nu_\tau$ decay channel only. Second, the hadronic decay channels are the most sensitive ones (Table 3.1).

A realistic estimation must include the effects of detector acceptance and helicity correlation between the two parent $\tau$'s in the event, but nevertheless, Table 3.1 clearly shows the merits of the various channels in the polarization measurement.

## Fitting and Measurement Techniques

A linear combination of simulated event distributions for positive and negative helicities is fitted to the data with the polarization $P_\tau$ as a free parameter. Specifically, the fitting function used is

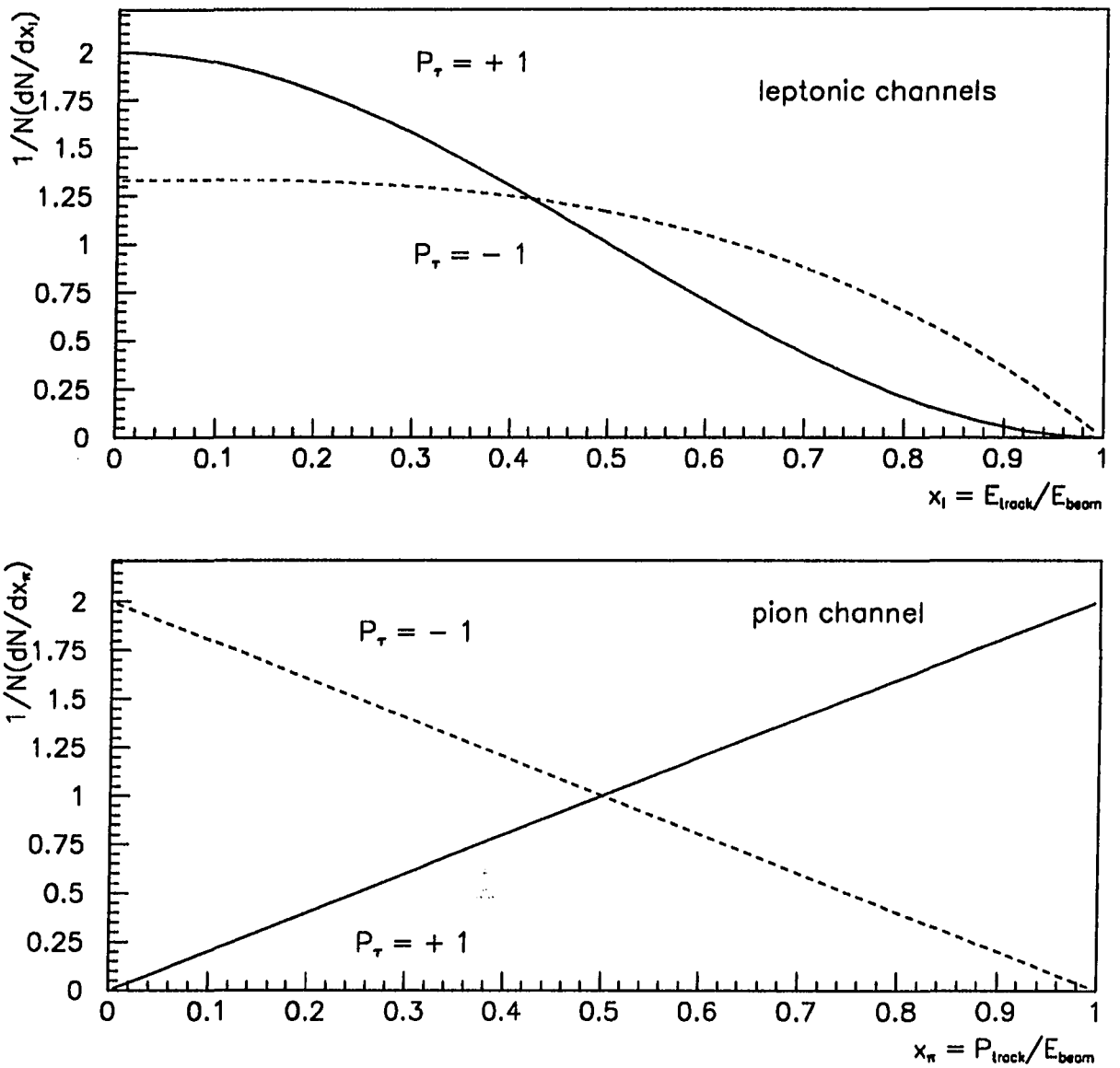


**Figure 3.1:** The expected $\tau$ decay distribution for leptonic (top) and pion modes (bottom) for the two polarization values.

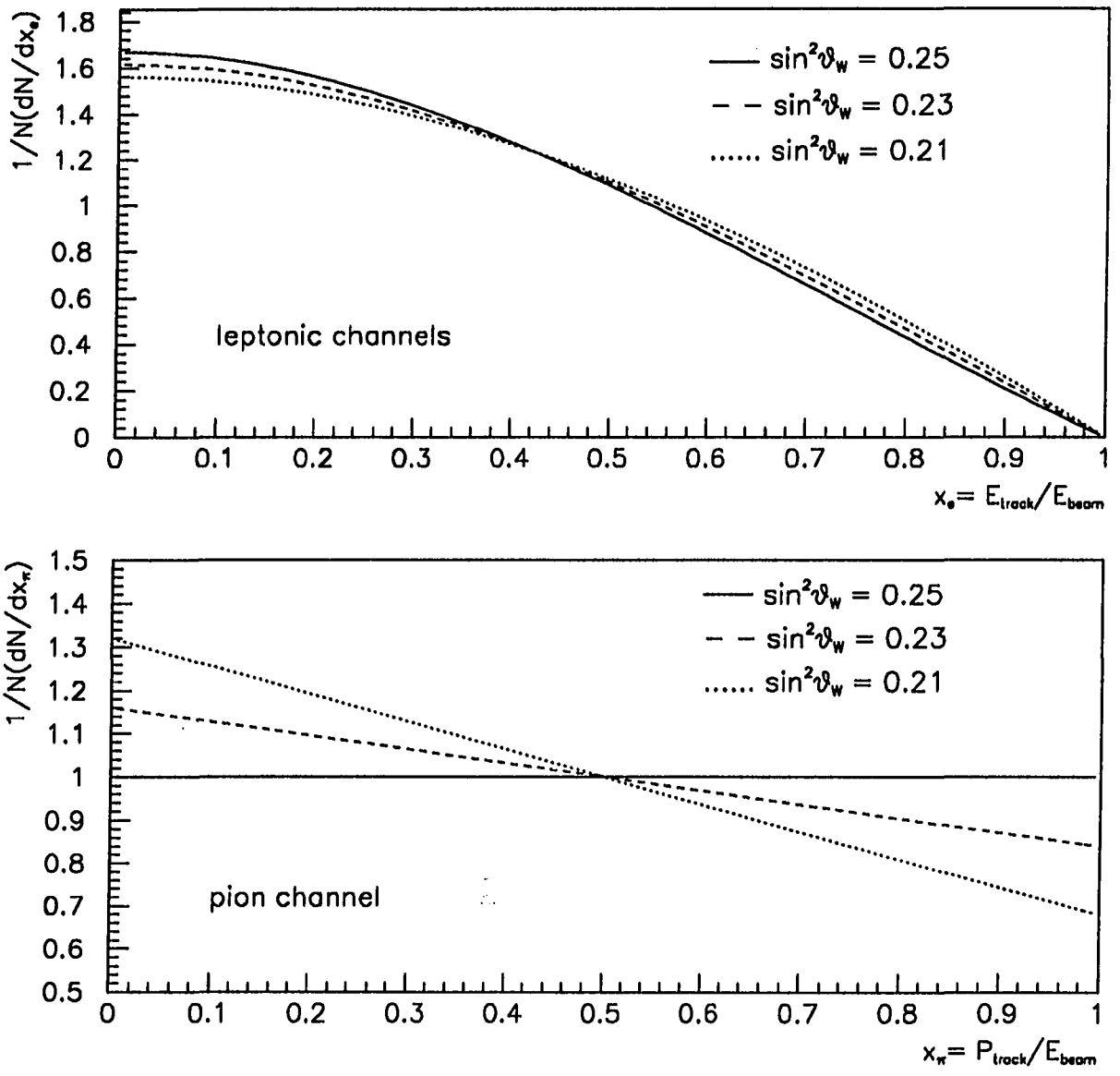


**Figure 3.2:** The expected $\tau$ decay distribution for leptonic (top) and pion modes (bottom) for different values of $sin^2\theta_W$.

$$F(P_\tau) = \frac{1}{2}\left[(1+P_\tau)\cdot f(h=+1) + (1-P_\tau)\cdot f(h=-1)\right], \qquad (3.15)$$

where $f(h=+1)$ and $f(h=-1)$ are the positive and negative helicity distributions, respectively. In general, the acceptances for each of the two helicity states in each channel will be different, causing a slight bias in the polarization measurement of the sample. Small acceptance corrections were derived from Monte Carlo simulation and have been applied in the final fit procedure for each channel. See Table 6.17.

Data and Monte Carlo are averaged over the different center of mass energies, ignoring the small energy dependence of the polarization in the fitting procedure.

The hadronic channels provide the most sensitive measurement of the $\tau$ polarization, though they suffer from high internal backgrounds. On the other hand, the leptonic channels are the least sensitive but benefit from low background levels. Therefore, in order to obtain the best possible measurement, the two most sensitive hadronic channels ($\tau^- \to \pi^-(K^-)\nu_\tau$ and $\tau^- \to \rho^-\nu_\tau$) and one of the leptonic channels ($\tau^- \to e^-\bar{\nu}_e\nu_\tau$) have been chosen for this analysis. This particular choice of decay channels provides a precise, yet balanced measurement of the $\tau$ polarization. The leptonic channel measurement serves as a consistency check of the sensitive measurement provided by the hadronic channels, since it suffers from low background levels that can distort the measurement. The combined statistical power of the three measurements from the 1991 and 1992 data sets ought to provide for a very sensitive measurement of the weak mixing angle.

For the $\tau^- \to e^-\bar{\nu}_e\nu_\tau$ channel, the $\tau$ polarization is determined from the $E_{cone}$ spectrum. $E_{cone}$ is defined as the total electromagnetic energy found in a 30° cone

Table 3.1: Figures of merit of the $\tau$ decay channels.

| Decay mode | $S_Y$ | $B_Y$ | $\Delta P_\tau\sqrt{N_\tau}$ |
|---|---|---|---|
| $e\nu\bar{\nu}$ | 0.22 | 0.18 | 10.71 |
| $\mu\nu\bar{\nu}$ | 0.22 | 0.18 | 10.71 |
| $\pi\nu$ | 0.60 | 0.11 | 05.03 |
| $\rho\nu$ | 0.52 | 0.23 | 04.01 |
| $a_1\nu$ | 0.24 | 0.07 | 15.75 |

around the track extrapolation to the HPC. This includes both the energy associated to the charged track and the neutral energy from radiated photons and photon conversions. In this manner, the polarization is less dependent on the substantial radiative corrections in this channel. For the $\tau^- \rightarrow \pi^- \nu_\tau$ channel, the polarization is extracted from the momentum spectrum, Lastly, the polarization for the $\tau^- \rightarrow \rho^- \nu_\tau$ channel is obtained from a 2-dimensional fit to the $cos\rho$ and $cos\psi$ distributions.

# CHAPTER 4. PARTICLE IDENTIFICATION

In experimental particle physics, good particle identification is necessary for obtaining accurate measurements of observable quantities. It is especially important that detectors work to complement one another in the task of particle identification, as a means of cross-checking the efficiencies of the various subdetectors.

At DELPHI, particle identification in the barrel region is achieved by the information provided by various subdetectors. The MVD, ID, TPC, OD and MUB provide tracking information while the HPC and HAC provide calorimetry information.

Particle identification of the various particles relevant to this analysis is described in more detail in this chapter.

## Electron Identification

Electrons in $\tau \rightarrow e\nu\overline{\nu}$, are identified by the $dE/dX$ information from the TPC, and the showering pattern in the HPC. The TPC is capable of achieving good separation between electrons and pions in the range of 0.2 to 8 $GeV/c$ (Figure 4.1).

To identify a track in the TPC as an electron, the PDEDX variable is used. PDEDX is defined as the difference between the measured $dE/dX$ and the expected $dE/dX$ for an electron with a given momentum $P$, normalized by $\Delta(dE/dX)$, the $dE/dX$ measurement uncertainty:

$$PDEDX = \frac{dE/dX(measured) - dE/dX(expected)}{\Delta(dE/dX)}. \qquad (4.1)$$

The HPC longitudinal segmentation (9 layers) and its excellent spatial resolution are used to identify electrons. The mean longitudinal profile of the energy deposition in an electromagnetic shower can be described by a gamma distribution [25]:

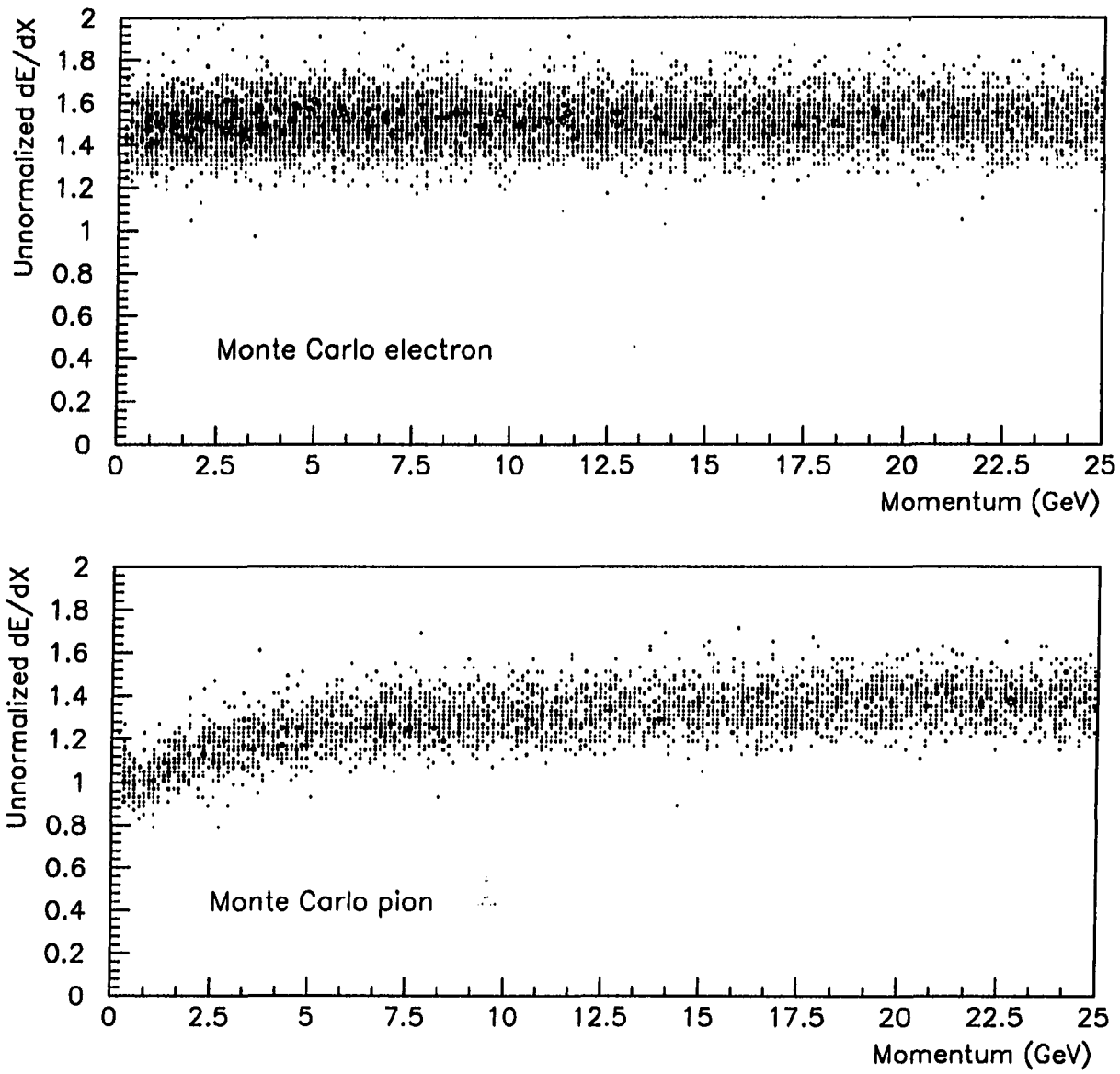


**Figure 4.1: dE/dX variable. Tau Monte Carlo prediction for electron (top) and pion (bottom).**

$$\frac{dE}{dt} = E_0 \cdot b \cdot \frac{(bt)^{a-1} e^{-bt}}{\Gamma(a)}, \tag{4.2}$$

where $t$ is the shower depth (in units of radiation length), $E_0$ is the shower energy and $a$ and $b$ are empirical parameters. In this parametrization, the maximum of the shower, $t_{max} = a/b$, and the scale factor, $L = 1/b$, are both logarithmically dependent on $E_0$.

To identify a particle showering in the HPC as an electron, (4.2) is used to estimate the expected energy deposition per layer. The sum of the squares of the differences between the expected and the measured value of the energy deposited per layer, weighted by the energy measurement uncertainty, is then used as the $\chi^2$ electron identification variable. Details of this algorithm can be found elsewhere [26]. Typically, electrons shower "early", that is, the showering process begins in the first or second HPC layer (Figures 4.2 and 4.3).

## Pion Identification

Pions are identified by a combination of TPC, HPC, HCAL and MUB information. Low energy pions are identified in the TPC by the PDEDX variable, and the showering pattern in the HPC and/or HCAL. Typically, pions leave a minimum ionizing shower pattern in the HPC (total energy deposition less than 0.4 $GeV$) and a shower in the HCAL consistent with a hadronic particle (Figure 6.18),

$$EPION = \frac{\Sigma E_{layer}}{N_{layer} \cdot F(\theta)}, \tag{4.3}$$

where $N_{layer}$ = number of HCAL layers with energy deposition $E_{layer}$, and [27]

$$F(\theta) = 1 + \frac{1 - sin\theta}{1 - 1/\sqrt{2}}. \tag{4.4}$$

Interacting pions, that is, pions that shower in the HPC, usually leave a large energy deposition in the HPC, which can be mistaken for a electromagnetic shower. However, hadronic showers in the HPC take longer to develop than an electromagnetic one [28], and the full power of the HPC longitudinal segmentation is realized.

Hadronic showers typically start "late" in the HPC (Figure 4.4), although the first layer of energy deposition for pions in the HPC is a function of momentum.

Lastly, high momentum pions are not easily separated from electrons in the TPC, and they may punch through the HCAL and leave a signal in the MUB, faking a muon signature. The use of the *EPION* variable and a constraint on the depth of the signal in the MUB are sufficient to eliminate the muon background in this case.

### Muon Identification

Muons are identified with the help of the HPC, HCAL and MUB (Figure 4.5). A typical muon behaves as a minimum ionizing particle in the HPC and HCAL and leaves a signal in the MUB overlapping layers (see "Pion Identification").

Whereas the efficiency for detection of high energy muons is high with the MUB alone, the identification of low momentum muons requires the combined usage of HPC, HCAL and MUB for maximum effectiveness.

Particles that leave a minimum ionizing signal in the HPC, a shower pattern consistent with a muon in the HCAL and a signal in the MUB beyond the first layer are accepted as muon candidates.

### Photon Identification

Photons and other neutral particles are identified by the MVD, TPC and HPC.

A shower in the HPC is accepted as a photon candidate if no tracks in the TPC and in the MVD are associated to it (Figure 4.6). Furthermore, the following requirements are imposed in order to improve the quality of the sample [29]:

- $E_{HPC} > 0.5\ GeV$.
- The neutral particle deposits energy in at least 3 consecutive layers in the HPC.

These cuts suppress $\delta$-rays and most low-energy $\gamma$ conversions in the BRICH/OD walls.

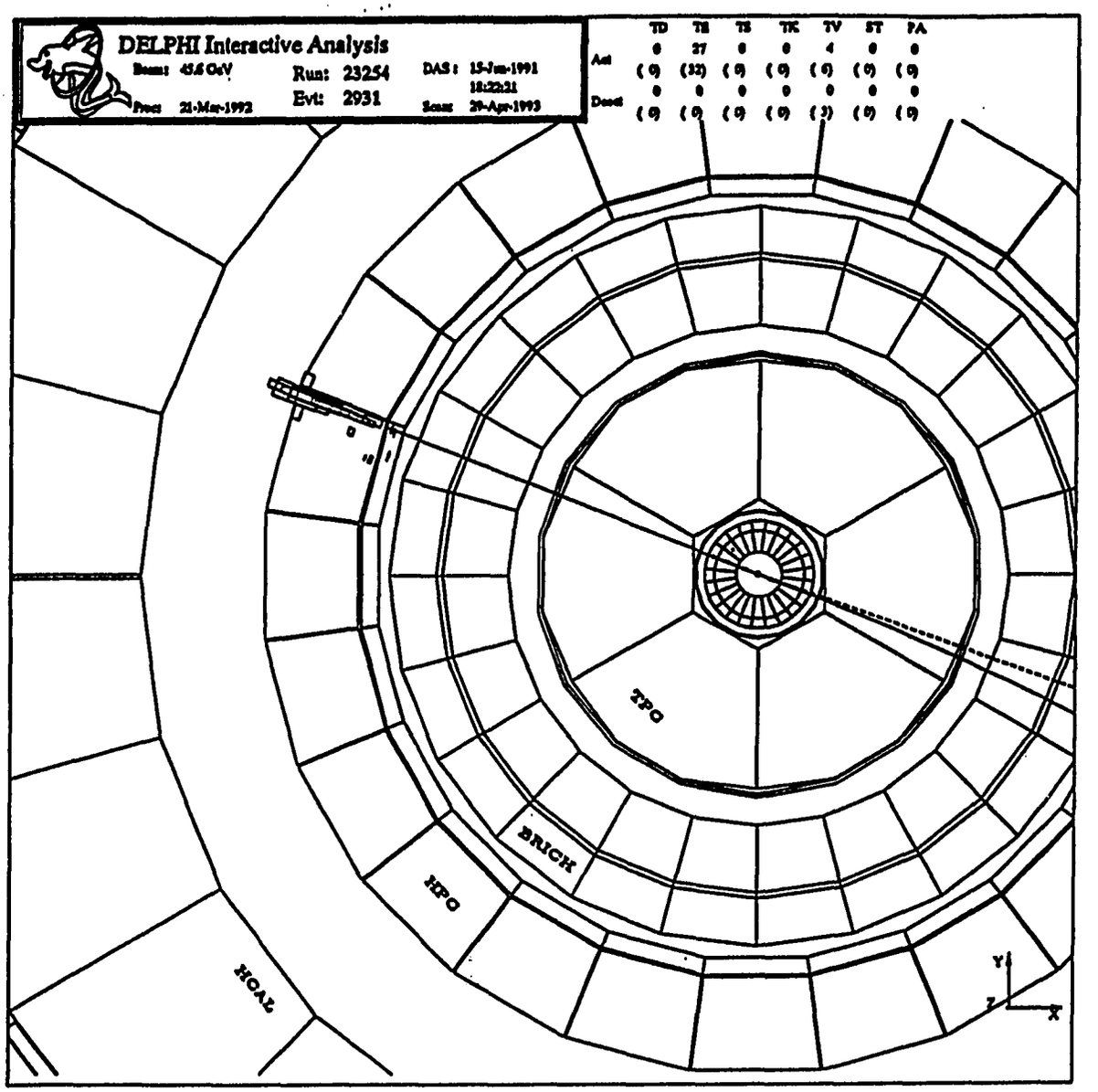


Figure 4.2: A typical tau electron in the HPC. Notice the "early" shower development.

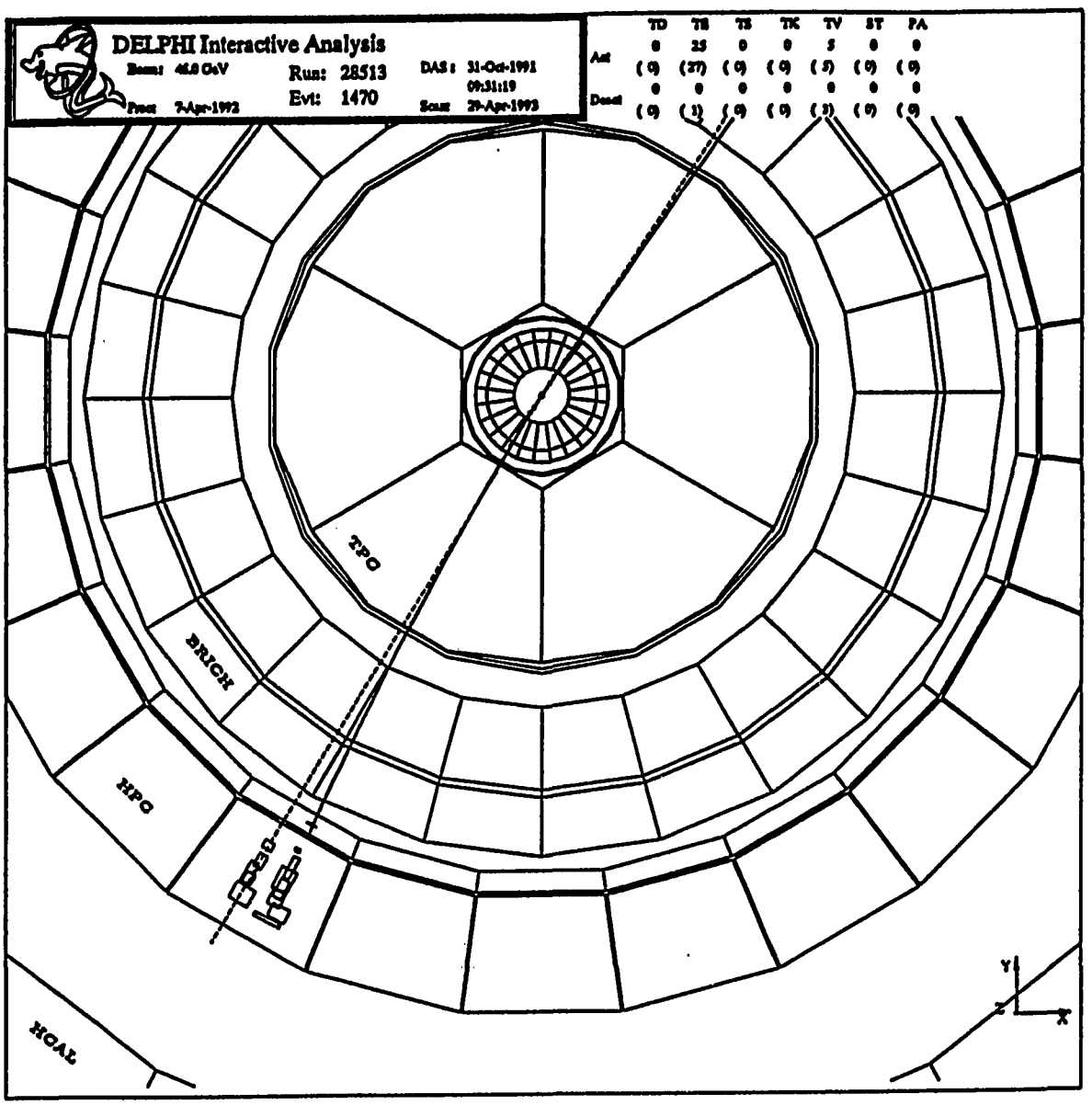


Figure 4.3: A tau electron with a radiated photon in the HPC.

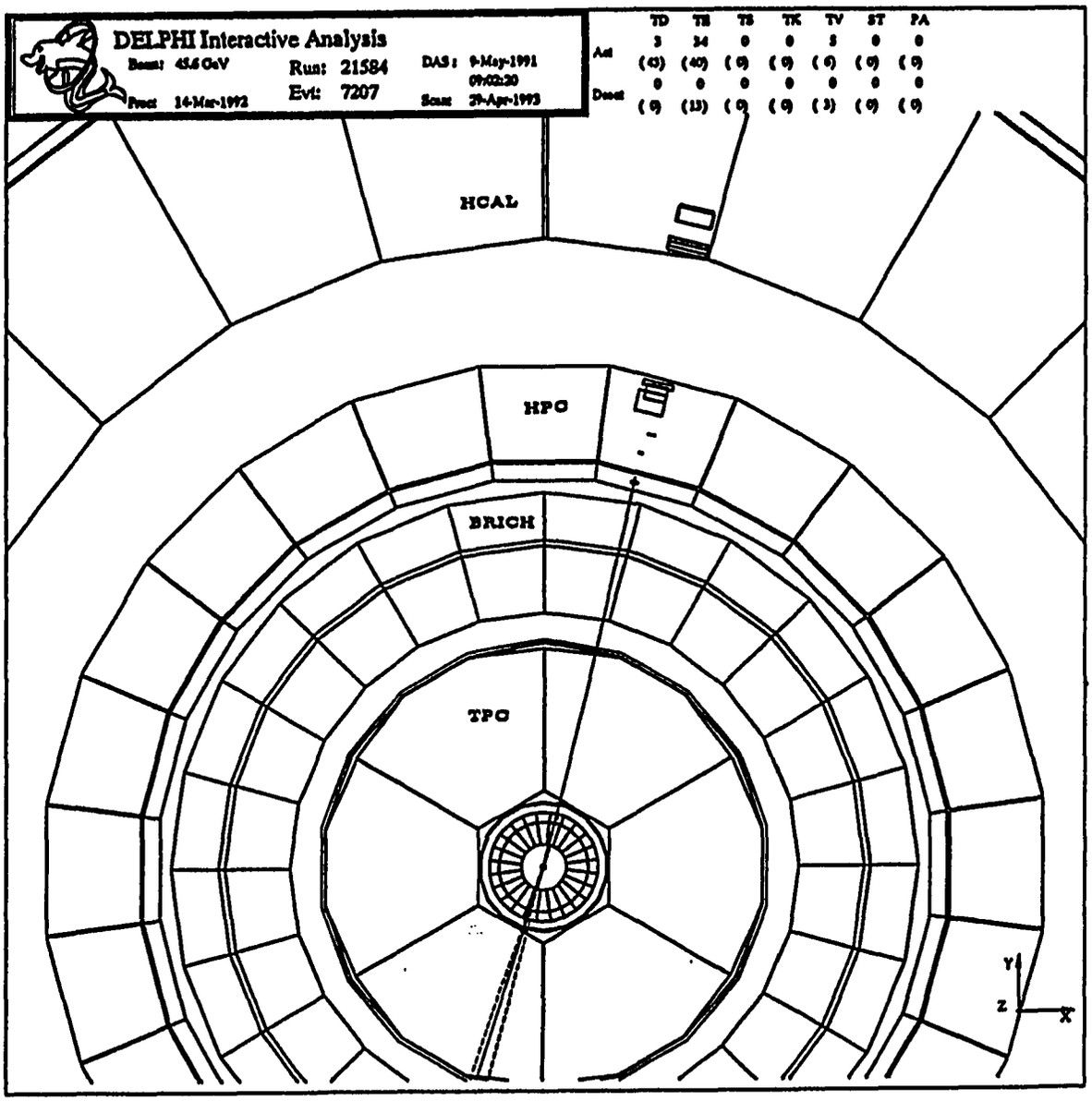


Figure 4.4: An interacting tau pion. Notice the "late" shower pattern in the HPC and punch-through into the HCAL.

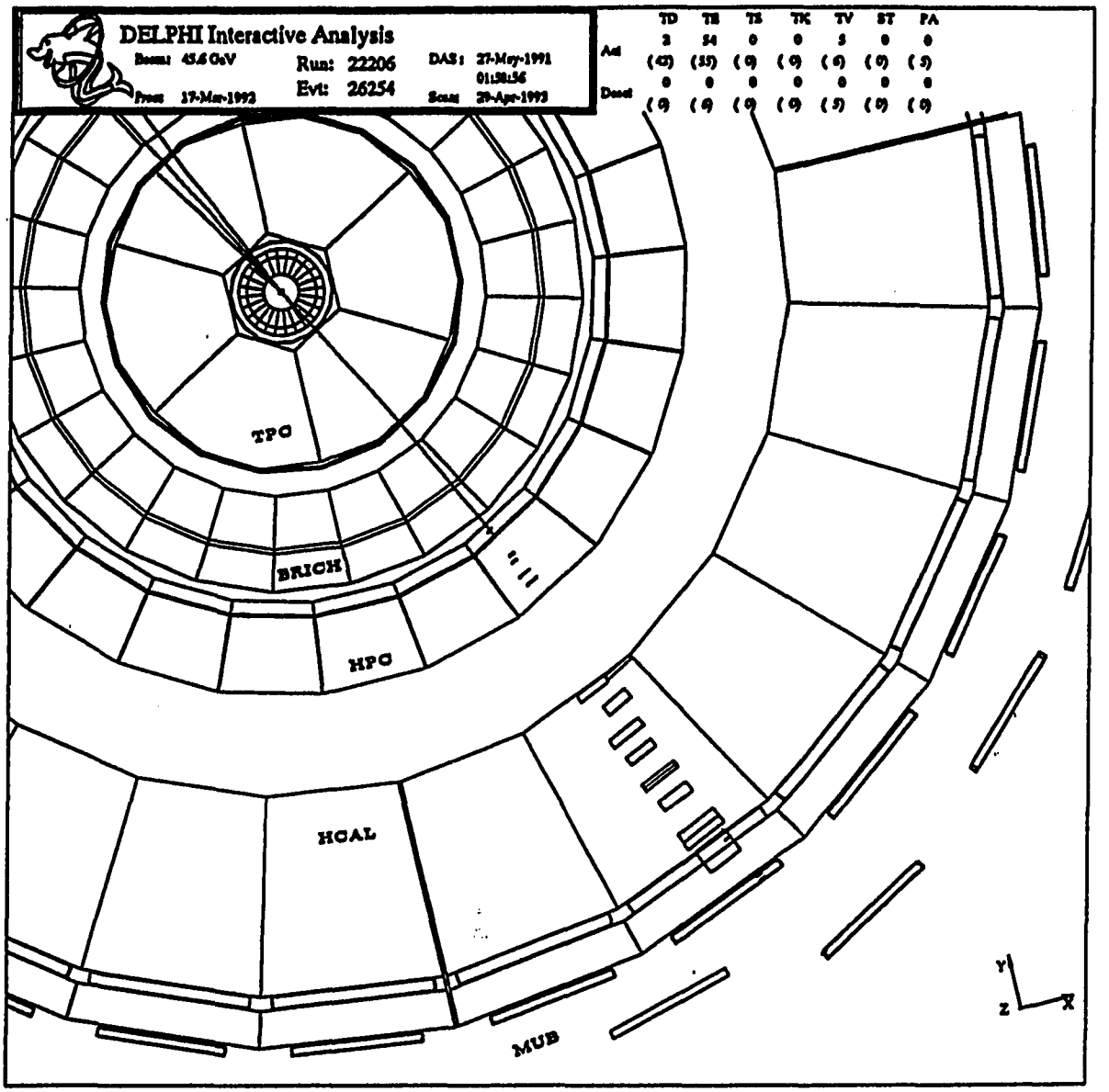


Figure 4.5: A typical tau muon. Notice the m.i.p. signal in the HPC, deep penetration in the HCAL and a signal in all MUB layers.

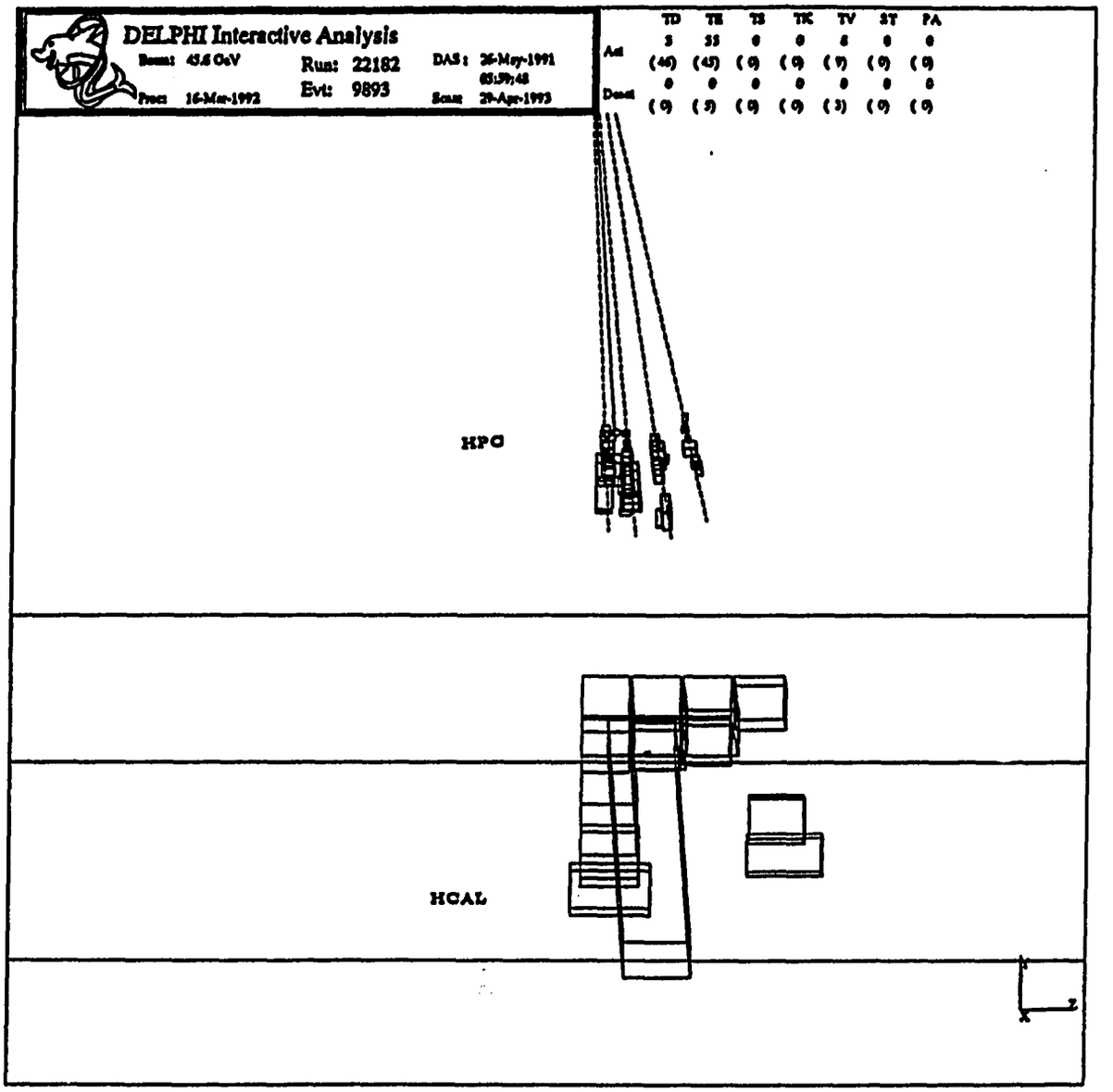


Figure 4.6: Typical photons (dotted lines) in the HPC. The excellent spatial resolution of the HPC allows good separation between close electromagnetic showers.

# CHAPTER 5. EVENT SELECTION

In this section, a detailed discussion of the analysis is presented, including a description of the data sets and a description of the Monte Carlo simulations, along with a brief summary of the procedures used to select and organize them.

The data sets used were recorded in 1991 and 1992 by the DELPHI detector at LEP. In 1991, 6547 $\tau^+\tau^-$ events were selected, and in 1992, 18357 $\tau^+\tau^-$ events were selected from the general data sample, corresponding to 750000 hadronic $Z^\circ$ decays in 1992 (225000 hadronic $Z^\circ$ decays in 1991).

The general procedure for processing raw data from the DELPHI detector is as follows: raw data is first processed by DELANA [30], the DELPHI data analysis program, whose output is a detailed data structure containing individual subdetector information about every charged and neutral particle observed in every event. This data structure is commonly referred to as TANAGRA data [31]. Since most physics analysis do not need such detailed information and since TANAGRA data is very volumous, a reduced data set produced from TANAGRA through the PXDST program [32] has been performed. This reduced data set is known as Data Summary Tape (DST) data, and although its use is common in experimental high energy physics, the contents of this data structure are unique to each experiment. DST data contains a summary of event-by-event information, such as run number, event number, center-of-mass energy, individual track positions, momenta, associated shower energies, neutral shower information, etc.

Monte Carlo simulation is first produced by generators such as BABAMC, DYMU3, KORALZ and JETSET [33], which generate "raw" simulated data. Next, this "raw" data is processed through a detailed simulation of the DELPHI detector called DELSIM [34]. This program includes a vast array of physics processes (such as interactions of particles with the detector material and particle decays) and the

response of the various subdectors to the particles interactions (such as drifting of ionization charge, dead zones in a subdetector, response of the electronics). Lastly, the output of DELSIM is processed through DELANA and PXDST, just as in the case of real data. The final simulated data has the same TANAGRA and DST structure as real data, so direct comparisons between data and Monte Carlo distributions are possible. In addition, the simulated data also contains information about event generation and the ensuing decay processes.

From these DST data, the leptonic selection and the $\tau$ selection are performed to obtain the final $\tau$ enriched data sample.

Before identifying exclusive $\tau$ decays, an enriched sample of $\tau^+\tau^-$ events has been selected with a loose set of cuts. The selection was optimized to minimize distortions in the momentum and energy spectra and decay mode dependent biases.

The thrust axis is defined as the direction of the most energetic track, and the plane perpendicular to this axis divides the event into two hemispheres corresponding to each $\tau$. The most energetic track on each hemisphere is defined as the leading track in that hemisphere. For the purpose of this selection, calorimetric energies in the HPC are defined as all energy deposited in a cone of $30^\circ$, $E_{cone}$, around a charged track.

The selection occurred in two stages. First, $Z^\circ \rightarrow l^+l^-$ events were selected with the following requirements [35]:

- two back to back jets with one particle in one jet and up to five in the other. The acolinearity angle, $\theta_{acol}$, between the isolated particle and the resultant momenta of the particles in the opposite jet is required to be less than $20^\circ$;
- the isolation angle, defined as the angle between the isolated particle and the closest particle in the recoiling jet, is required to be greater than $160^\circ$;
- the total visible energy in the event (charged and neutral particles) is required to be greater than 8 $GeV$.

In addition, each charged particle has to satisfy the following conditions:

- momentum greater than 200 $Mev/c$;
- distance of closest approach of the track to the beam axis less than 5.0 $cm$;

- distance of closest approach to the nominal interaction point along the beam direction less than 10.0 *cm*.

These cuts reject hadronic events and low energy background from two-photon interactions (Figure 5.1).

In the second stage, tau pairs were separated from the other two leptonic channels. This has been achieved by taking advantage of the presence of undetected neutrinos in all tau decay modes, as opposed to $e^+e^- \rightarrow e^+e^-$ and $e^+e^- \rightarrow \mu^+\mu^-$ events (Figure 5.2), which are characterized by low acolinearity and high visible momentum/energy [36].

In order to insure good understanding of the detector response, the angular acceptance was restricted to the barrel region of DELPHI, $43^\circ < \theta < 137^\circ$. However, as $e^+e^- \rightarrow \tau^+\tau^-$ events are very acolinear, the requirement that both $\tau$'s be within this polar range is very strict. Instead, the criteria used is that at least one leading track be in this polar range.

Before the selection criteria can be described, it is necessary to define the following two variables:

- The "Radial Energy" variable, $E_R$, is defined as $E_R = \sqrt{E_1^2 + E_2^2}/E_{beam}$, where $E_1$ is the $E_{cone}$ energy in the HPC associated with the most energetic track (the "leading" track) in hemisphere 1, and $E_2$ is the corresponding variable in hemisphere 2. $E_{beam}$ is the beam energy.
- The "Radial Momentum" variable, $P_R$, is defined as $P_R = \sqrt{P_1^2 + P_2^2}/E_{beam}$, where $P_1$ is the momentum of the isolated track, and $P_2$ is the resultant momentum of the tracks in the opposite hemisphere.

The selection of tau pairs has been done with the following criteria:

- $E_R < 1.0$;
- $P_R < 1.0$.

These cuts highly suppress the bhabha and dimuon background, while affecting only slightly the $\tau^+\tau^-$ sample. Figure 5.3 shows the variable $E_R$ for Monte Carlo

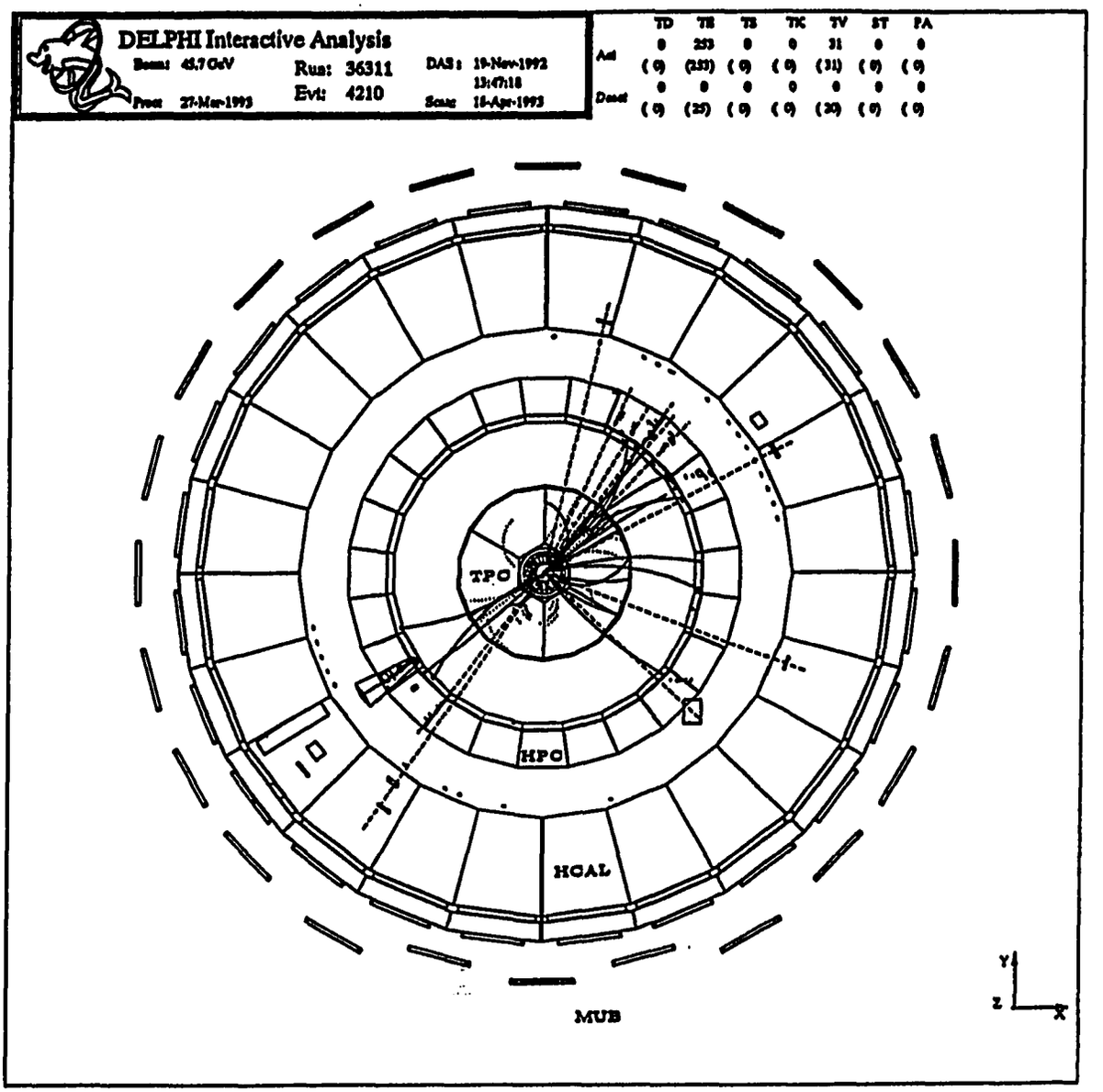


Figure 5.1: A typical $e^+e^- \rightarrow q\bar{q}$ event.

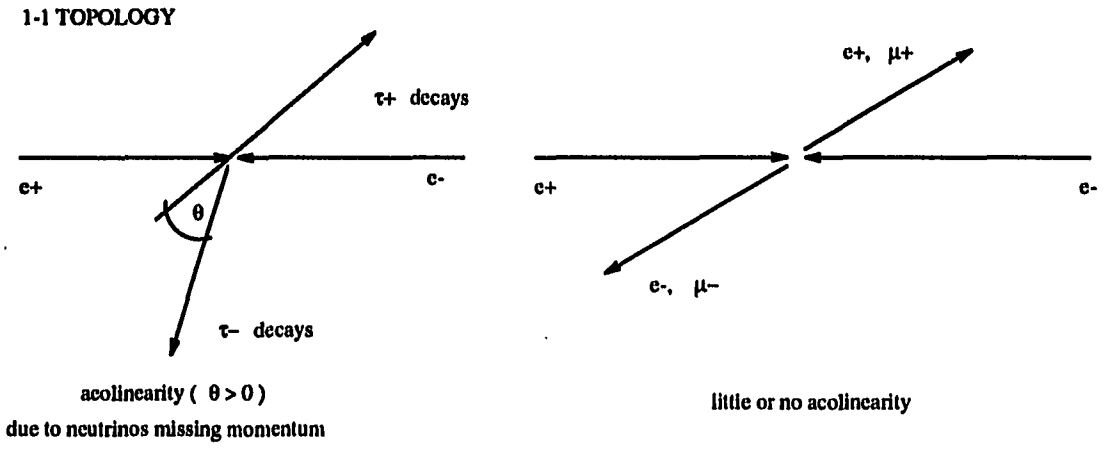


Figure 5.2: Topologies for $Z^{\circ}$ nonradiative leptonic decays.

taus, bhabhas and dimuons. Figure 5.4 shows the variable $P_R$ for similar Monte Carlo data sets.

In order to reject cosmic ray, beam-gas and beam-wall events, tracks are required to originate at the beam intersection point. We require:

- $|z1| < 4.5\ cm$ and $|z2| < 4.5\ cm$;
- $|r1| < 1.5\ cm$ and $|r2| < 1.5\ cm$,

where $r1$ and $r2$ are the impact parameters of the two leading tracks with respect to the interaction point, while $z1$ and $z2$ are the longitudinal distances between the points of closest approach and the interaction point.

Another source of background comes from two-photon events, $e^+e^- \rightarrow e^+e^- f\bar{f}$, when the final state $e^+e^-$ escape undetected at low polar angles and the $f\bar{f}$ system is misidentified as a low-visible-energy and low-transverse-momentum $\tau$ pair event.

Therefore, to reject cosmic ray events (those which cross near the nominal interaction region) and $e^+e^- \rightarrow e^+e^- f\bar{f}$ events, two prong events must satisfy the following criteria:

- $\theta_{acol} > 0.5^\circ$;
- $|z1 - z2| < 3\ cm$;
- $|P_T| > 0.4\ GeV$,

where $P_T$ is the transverse component of the total momentum of the event.

### Results of Event Selection with 1991 Monte Carlo Simulations

The selection criteria described above have been applied to Monte Carlo simulations with the 1991 DELPHI detector configuration. The detailed study included both data and Monte Carlo studies.

Table 5.1 shows the selection efficiency in the fiducial region for each of the individual channels considered. Small decay mode dependent biases lead to slightly different efficiencies for each channel. Backgrounds from the other leptonic channels, $q\bar{q}$, cosmic rays and other sources are summarized in Table 5.2.

Table 5.1: 1991 Selection efficiency for individual exclusive channels.

| Decay mode | Efficiency |
|---|---|
| $e\nu\bar{\nu}$ | $83.35 \pm 0.90\%$ |
| $\mu\nu\bar{\nu}$ | $86.42 \pm 0.93\%$ |
| $\pi(K)\nu$ | $79.66 \pm 1.07\%$ |
| $\rho\nu$ | $83.28 \pm 0.80\%$ |
| $a_1\nu$ | $81.60 \pm 0.96\%$ |

Table 5.2: Background in 1991 $\tau$ selection.

| Source | Background |
|---|---|
| $e^+e^-$ | $0.96 \pm 0.11\%$ |
| $\mu^+\mu^-$ | $0.27 \pm 0.04\%$ |
| $q\bar{q}$ | $0.26 \pm 0.18\%$ |
| $e^+e^-f\bar{f}$ | $0.80 \pm 0.30\%$ |
| cosmics | negligible |

All backgrounds have been calculated from Monte Carlo simulation, with the exception of the cosmic ray background. In this case, we use the Outer Detector timing for two prong events in the data set. No significant background is found in the back-to-back coincidence time differential in that region, leading one to conclude that cosmic ray background is negligible in this selection [36].

### Results of Event Selection with 1992 Monte Carlo Simulations

A similar selection has been done with Monte Carlo simulations for the 1992 DELPHI detector configuration.

Table 5.3 shows the selection efficiency in the fiducial region for each of the individual channels considered. Background from the other leptonic channels, $q\bar{q}$, cosmics and other sources are summarized in Table 5.4. Figure 5.5 displays the average overall efficiency of the selection as a function of the $E_R$ and $P_R$ variables.

Table 5.3: Selection efficiency for 1992 individual exclusive channels.

| Decay mode | Efficiency |
|---|---|
| $e\nu\bar{\nu}$ | $83.14 \pm 0.79\%$ |
| $\mu\nu\bar{\nu}$ | $85.59 \pm 0.80\%$ |
| $\pi(K)\nu$ | $79.19 \pm 0.94\%$ |
| $\rho\nu$ | $82.38 \pm 0.70\%$ |
| $a_1\nu$ | $80.76 \pm 0.83\%$ |

Table 5.4: Background in 1992 $\tau$ selection.

| Source | Background |
|---|---|
| $e^+e^-$ | $0.95 \pm 0.10\%$ |
| $\mu^+\mu^-$ | $0.24 \pm 0.04\%$ |
| $q\bar{q}$ | $0.13 \pm 0.02\%$ |
| $e^+e^-f\bar{f}$ | $0.20 \pm 0.06\%$ |
| cosmics | negligible |

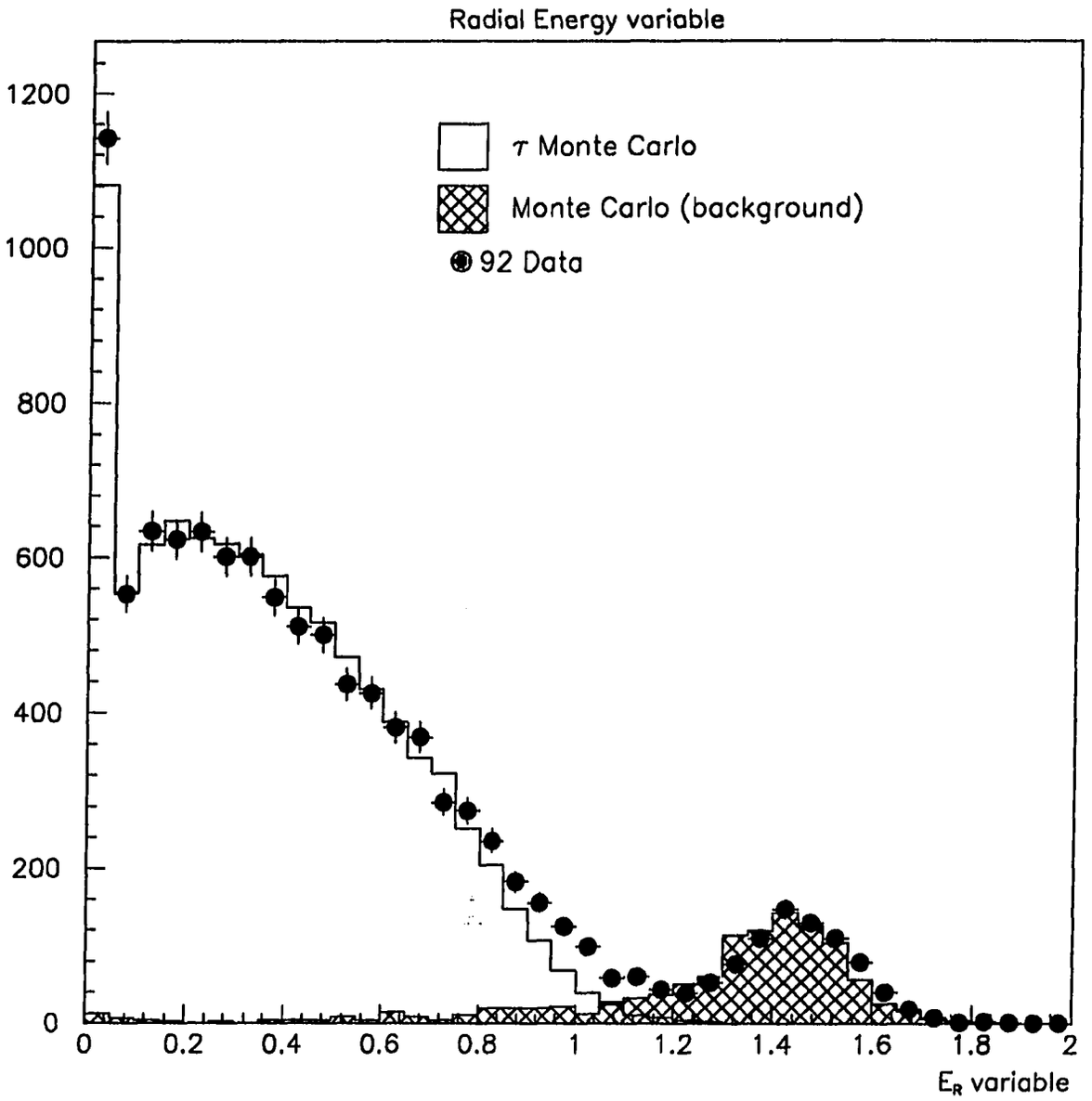


**Figure 5.3:** The $E_R$ variable. The Monte Carlo background only includes bhabhas and dimuons.

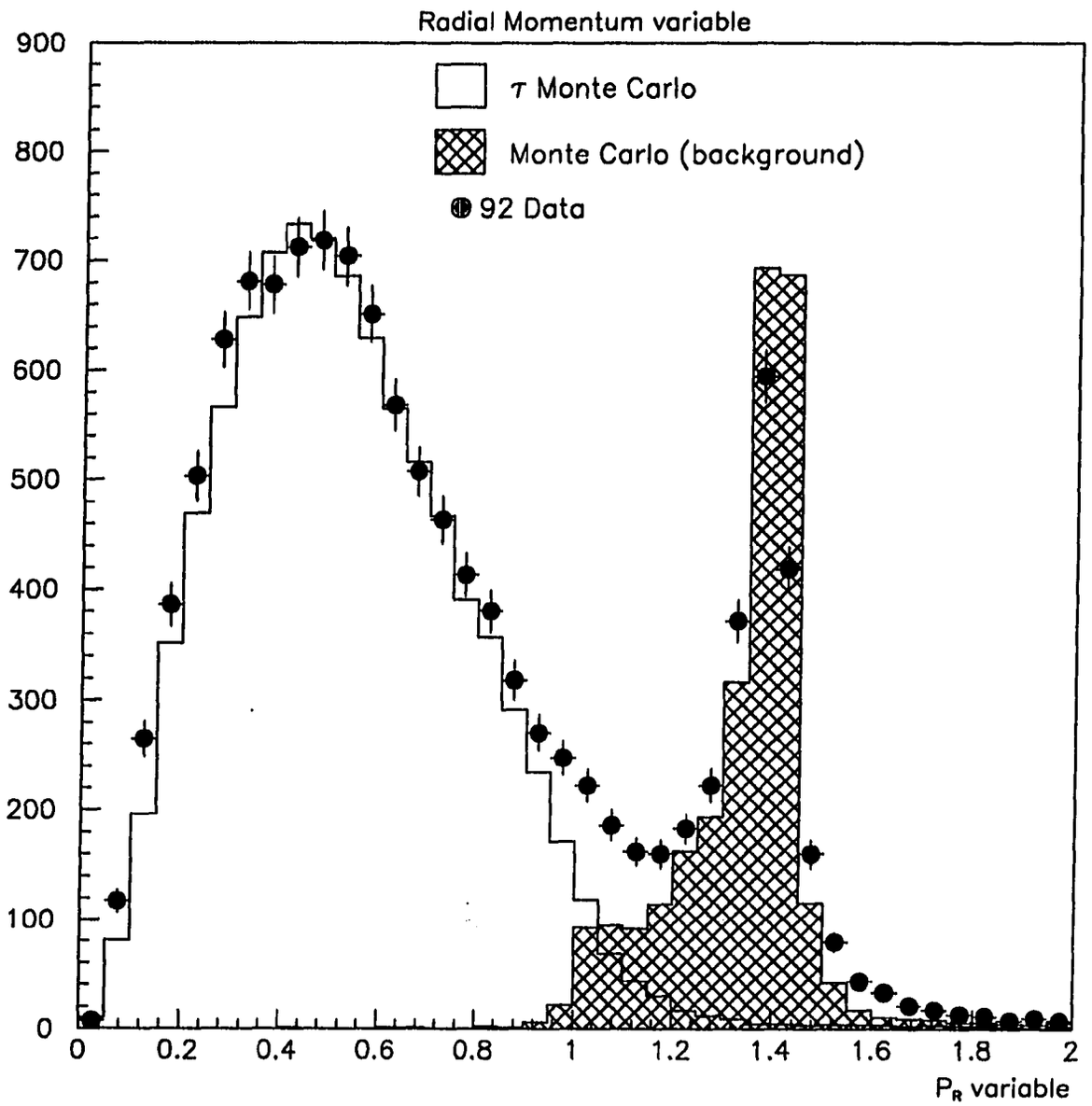


**Figure 5.4:** The $P_R$ variable. The Monte Carlo background only includes bhabhas and dimuons.

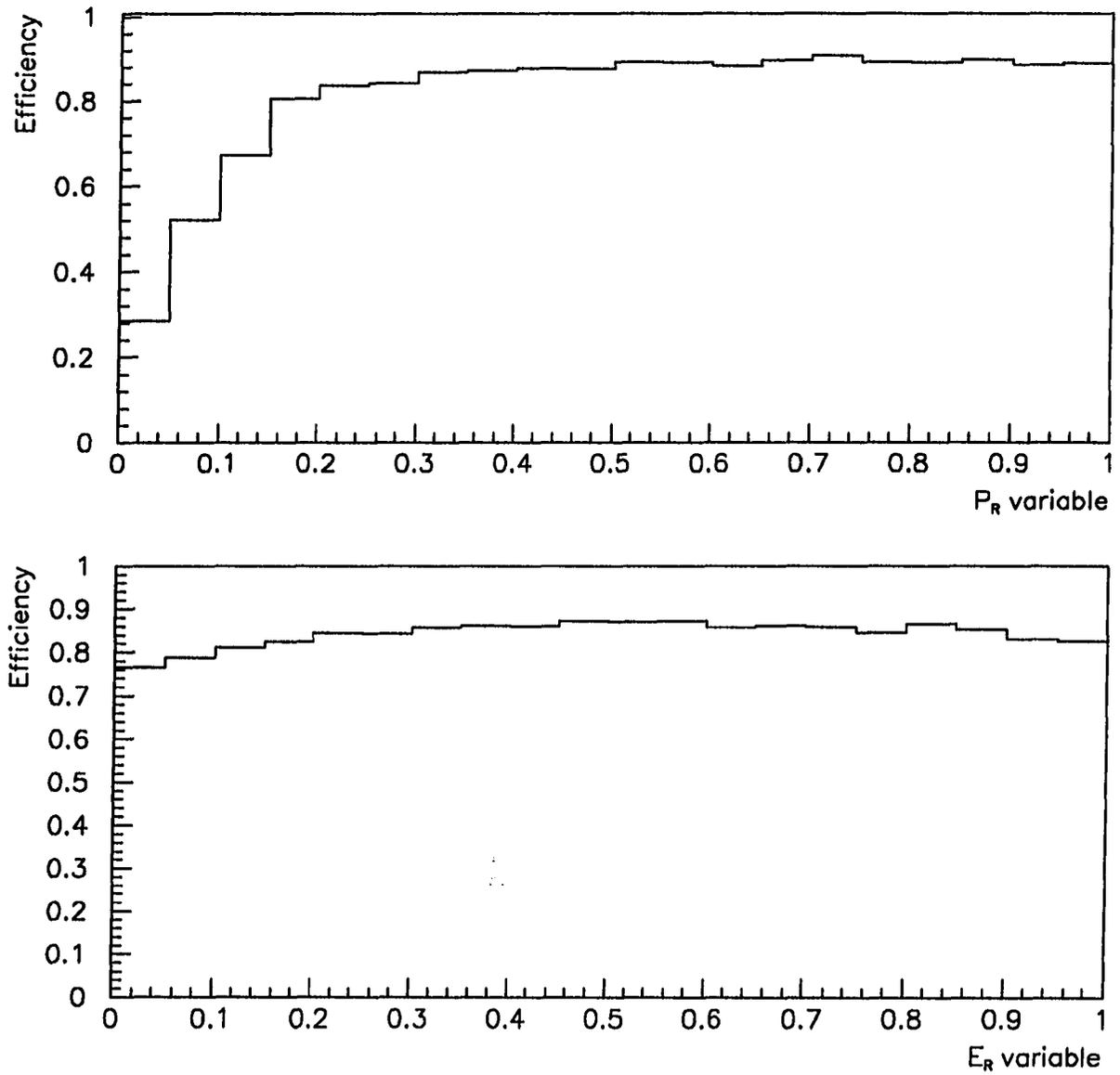


**Figure 5.5: The selection efficiency as a function of $P_R$ (top) and $E_R$ (bottom).**

# CHAPTER 6. ANALYSIS

This chapter has been divided in the following manner: a section is devoted to each channel analyzed. In each section, a brief description of the analysis techniques is presented, followed by a summary of the selection criteria and the results of the measurement. Due to slight differences in the DELPHI detector configuration during the 1991 and 1992 data acquisition periods, the 1992 selection criteria are slightly different from the 1991 selection criteria. A note is made whenever the selection criteria change from one period to another.

## The $\tau^- \longrightarrow e^-\overline{\nu}_e\nu_\tau$ Channel

Candidates for the $\tau^- \rightarrow e^-\overline{\nu}_e\nu_\tau$ channel are characterized by an isolated charged track identified as an electron (see "Electron Identification"). This analysis is based on the combined power of the TPC, HPC and HCAL in separating electron decays from $\pi$ and $\rho$ decays.

The main difficulties in this analysis are as follows:

1. electron/rho/pion separation in the HPC, in the presence of neutral activity near the track, and the particle momentum is high enough that the TPC dE/dX is not effective by itself in separating electrons from pions;

2. keeping a constant, flat selection efficiency as a function of energy, where pions are the predominant low energy background and bhabhas are the predominant high energy background;

3. suppressing the bhabha background, when one of the electrons is close to a gap between HPC modules, depositing considerably less energy and thus appearing to a be a $\tau$ event rather than a bhabha event. Bhabha background also enters

the sample from shower leakage at the edges of an HPC module, when one or both of the electrons may deposit considerably less energy in the HPC (Figure 6.1).

The dE/dX probability variable PDEDX (see "Particle Identification") is quite efficient in separating electrons and background (Figure 6.2), but its effectiveness decreases with increasing energy. On the other hand, the electron/background separation power of the $\chi^2$ of the longitudinal shower shape in the HPC is poor at low energies, but it improves rapidly with increasing energy. A combination of these two selection variables is used to obtain a flat efficiency as a function of energy.

High energy electrons will occasionally punch through the outer layer of the HPC and shower in the initial layer of the HCAL. In order to keep a minimum bias against high energy electrons, some selection criterion has to be imposed on HCAL energy. The background from bhabha events and pions is very high in the HCAL (Figure 6.3), so proper Monte Carlo simulation is crucial for a good understanding of this punch-through effect.

In order to reject $\pi$ + overlapping $\pi^0$ events (which may appear as one single, electron shower in the HPC), a selection cut is placed on the unassociated energy found in a $30^\circ$ cone (Figure 6.4) around the track extrapolation to the HPC. Electrons radiate soft (low energy) photons, whereas photons from $\pi^0$'s are usually of higher energy. Therefore, a cut on this variable rejects internal background from $\rho$, $a_1$, and K* decays.

### Selection Criteria

The procedure to select events in this channel is as follows:

- require 1-N topology, that is, 1 isolated track in one hemisphere and N tracks ($1 \leq N \leq 5$) in the other hemisphere (see "Event Selection").
- require PDEDX compatible with an electron candidate. Variations in the TPC calibration from the 1991 to the 1992 periods account for the slight difference in this selection requirement.

$$PDEDX > -2.0 \text{ (1991)};$$

$$PDEDX > -2.2 \text{ (1992)};$$

- to suppress bhabha background, require energy in HCAL < 1.0 GeV (changed to 0.5 GeV in 1992, due to the reduced sensitivity of the HCAL to low energy particles);
- require neutral energy contained in a $30^{\circ}$ cone around the track extrapolation to the HPC < 5.0 GeV, to suppress rho background (changed to 3.0 GeV in 1992 because of the increased sensitivity of the HPC to low energy particles);
- require the track to point into the fiducial region, $43^{\circ} \leq \theta \leq 137^{\circ}$;
- require $\chi^2$ of longitudinal profile of the energy deposition < 40.0 (Figure 6.5), to suppress pion background (changed to 100.0 in 1992 because of different running conditions);
- require $P_{track} > 0.05 \cdot E_{beam}$;
- require $E_{track} > 0.025 \cdot E_{beam}$.

These cuts reject $\tau^- \rightarrow \pi^- \nu_\tau$ and $\tau^- \rightarrow \rho^- \nu_\tau$ decays, the main internal background contributions. The PDEDX cut is effective against low momentum pions ($P < 10$ GeV/c). To reject high momentum pions and bhabhas, the cuts on HCAL energy and HPC longitudinal shower profile $\chi^2$ are required. The background computed from Monte Carlo simulations is found to be $1.58 \pm 0.37\%$ for 1991 data analysis. A sample of $\rho$ decays taken from 1991 data and characterized by a tagged $\pi^{\circ} \rightarrow \gamma\gamma$ in the HPC was used to check the Monte Carlo prediction. An overall correction was applied to the Monte Carlo prediction, yielding a corrected background of $3.07 \pm 0.74\%$.

Once an electron candidate was identified in the event, additional selection criteria were imposed to suppress background from bhabha events, $e^+e^- \rightarrow e^+e^-$. Bhabha events are characterized by two back-to-back jets with large electromagnetic

energy deposition in the HPC. However, events in which one of the electrons is near a gap between HPC modules can deposit considerably less energy (Figure 6.6). Because electrons radiate many low-energy photons as it travels from the interaction point to the HPC, there is a non-negligible probability that one or more photons will convert into an $e^+e^-$ pair. Depending on the conversion point, a bhabha event may be mistaken for a 1-N topology $\tau$ event. Therefore, the following additional selection cuts have been imposed on all 1-N events and not only on 1-1 topology:

- require that at least one of the leading tracks not point into a $\phi$ gap ($6^\circ < MOD(\phi, 15^\circ) < 9^\circ$);
- require that at least one of the leading tracks not point into the $\theta$ gap ($87^\circ < \theta < 93^\circ$);
- require that at least one of the leading tracks not leak out from the edges of the HPC outer modules ($43^\circ < \theta < 46^\circ$ and $134^\circ < \theta < 137^\circ$);
- require that only one leading track's PDEDX be compatible with an electron OR if both leading tracks' PDEDX are compatible with electrons, then require $(E_1 + E_2)/E_{beam} < 1.2$.

**Results from 1991 Data Analysis**

After the selection, a total of 1204 $\tau^- \to e^-\bar{\nu}_e\nu_\tau$ candidates remained in the 1991 data sample. The overall efficiency of this selection is $60.56 \pm 0.85\%$ ($P > 0.05 \cdot E_{beam}$), as computed from Monte Carlo simulation (Figure 6.7). The bhabha background estimated from Monte Carlo is $0.15 \pm 0.20\%$. A subsample of 1991 data containing bhabha events was used to correct the Monte Carlo prediction, and the corrected bhabha background is $0.28 \pm 0.24\%$.

The 1-dimensional fit to $E_{cone}/E_{beam}$ (Figure 6.8) yields

$$P_\tau = -0.223 \pm 0.111(stat.) \pm 0.080(syst.).$$

Table 6.1 summarizes the sources of background in this analysis, and Table 6.2 summarizes the correction factors to background and efficiency derived from selected 1991 data samples. The sources of the systematic errors are described in Table 6.3.

**Results from 1992 Data Analysis**

The selection yields 3358 events with an overall efficiency of $65.40 \pm 0.80\%$ ($P > 0.05 \cdot E_{beam}$) in the fiducial region, as computed from Monte Carlo simulation (Figures 6.9 and 6.10). The internal background, as computed from Monte Carlo simulation, yields $2.07 \pm 0.14\%$ (Figure 6.11). Using the same bhabha rejection criteria as in the 1991 analysis, the bhabha background, computed from bhabhas selected from the 1992 data sample, is $0.23 \pm 0.04\%$.

A 1-dimensional fit to $E_{cone}/E_{beam}$ (Figure 6.12) gives

$$P_\tau = -0.134 \pm 0.075(stat.) \pm 0.062(syst.).$$

Table 6.4 summarizes the background sources for the 1992 $\tau^- \rightarrow e^-\bar{\nu}_e\nu_\tau$ analysis, and Table 6.5 summarizes the corrections applied to background and efficiency. These corrections have been determined from 1992 data samples. The major sources of systematics are summarized in Table 6.6.

**The $\tau^- \longrightarrow \pi^-(K^-)\nu_\tau$ Channel**

The identification of $\tau^- \rightarrow \pi^-(K^-)\nu_\tau$ decays is more difficult, since most other tau decay channels are potential sources of background. The separation of electrons and $\rho$'s from pions relies on the fine granularity and hermeticity of the HPC. The separation of pions from muons requires redundancy between HCAL and MUB, which occurs only in the region $51^\circ < \theta < 129^\circ$.

In this analysis, the major difficulties are:

1. to keep good efficiency for high momentum pions which have a tendency to leave energy deposits deep in the HCAL or in the MUB, while removing background from $\tau^- \rightarrow \mu^-\bar{\nu}_\mu\nu_\tau$ decays;

2. to remove low energy muons which may leave no signal in the MUB and may appear to be a $\tau^- \rightarrow \pi^-\nu_\tau$ decay in the HCAL;

3. to remove background from $\tau^- \rightarrow \rho^-\nu_\tau$ decays when one or both photons from the $\pi^0$ is lost, either because it escapes through a gap between HPC modules,

Table 6.1: Background sources for the 1991 $\tau^- \rightarrow e^-\overline{\nu}_e\nu_\tau$ analysis.

| Decay mode | Background |
|---|---|
| $\mu\nu\overline{\nu}$ | $0.02 \pm 0.14\%$ |
| $\pi\nu$ | $1.11 \pm 0.40\%$ |
| $\rho\nu$ | $1.50 \pm 0.43\%$ |
| $a_1\nu$ | $0.25 \pm 0.27\%$ |
| $K\nu$ | $0.02 \pm 0.14\%$ |
| $K*\nu$ | $0.05 \pm 0.19\%$ |
| multi-$\pi\nu$ | $0.12 \pm 0.23\%$ |
| $e^+e^-$ | $0.28 \pm 0.24\%$ |
| $\mu^+\mu-$ | negligible |

Table 6.2: Correction factors to Monte Carlo predictions for the 1991 $\tau^- \rightarrow e^-\overline{\nu}_e\nu_\tau$ analysis.

| $E_{cone}/E_{beam}$ | Internal background | Bhabha background | efficiency |
|---|---|---|---|
| $0.0 \rightarrow 0.1$ | 4.68 | 1.00 | 1.00 |
| $0.1 \rightarrow 0.2$ | 1.58 | 1.00 | 0.95 |
| $0.2 \rightarrow 0.3$ | 1.18 | 1.00 | 0.95 |
| $0.3 \rightarrow 0.4$ | 0.76 | 1.00 | 0.92 |
| $0.4 \rightarrow 0.5$ | 0.58 | 1.00 | 1.07 |
| $0.5 \rightarrow 0.6$ | 0.90 | 1.01 | 1.00 |
| $0.6 \rightarrow 0.7$ | 0.68 | 1.00 | 1.00 |
| $0.7 \rightarrow 0.8$ | 0.87 | 1.11 | 1.00 |
| $0.8 \rightarrow 0.9$ | 0.67 | 1.04 | 1.00 |
| $0.9 \rightarrow 1.0$ | 1.00 | 0.85 | 1.00 |

Table 6.3: Summary of systematic errors for the 1991 $\tau^- \rightarrow e^-\overline{\nu}_e\nu_\tau$ analysis.

| Source | Systematic Error |
|---|---|
| Electron Identification | 0.036 |
| Bhabha background | 0.045 |
| Internal background | 0.032 |
| Effc. energy dependence | 0.018 |
| Monte Carlo statistics | 0.042 |

Table 6.4: Background sources for the 1992 $\tau^- \rightarrow e^-\bar{\nu}_e\nu_\tau$ analysis.

| Decay mode | Background |
|---|---|
| $\mu\nu\bar{\nu}$ | negligible |
| $\pi\nu$ | $1.07 \pm 0.10\%$ |
| $\rho\nu$ | $0.77 \pm 0.08\%$ |
| $a_1\nu$ | $0.15 \pm 0.04\%$ |
| $K\nu$ | $0.02 \pm 0.01\%$ |
| $K*\nu$ | $0.03 \pm 0.02\%$ |
| multi-$\pi\nu$ | $0.03 \pm 0.02\%$ |
| $e^+e^-$ | $0.23 \pm 0.04\%$ |
| $\mu^+\mu-$ | negligible |

Table 6.5: Correction factors to Monte Carlo predictions for the 1992 $\tau^- \rightarrow e^-\bar{\nu}_e\nu_\tau$ analysis.

| $E_{cone}/E_{beam}$ | Bhabha background | efficiency |
|---|---|---|
| $0.0 \rightarrow 0.1$ | 1.00 | 1.05 |
| $0.1 \rightarrow 0.2$ | 1.00 | 1.02 |
| $0.2 \rightarrow 0.3$ | 1.00 | 0.98 |
| $0.3 \rightarrow 0.4$ | 1.00 | 0.97 |
| $0.4 \rightarrow 0.5$ | 1.00 | 0.95 |
| $0.5 \rightarrow 0.6$ | 1.00 | 1.05 |
| $0.6 \rightarrow 0.7$ | 1.40 | 1.00 |
| $0.7 \rightarrow 0.8$ | 1.62 | 1.00 |
| $0.8 \rightarrow 0.9$ | 1.08 | 1.00 |
| $0.9 \rightarrow 1.0$ | 1.00 | 1.00 |

Table 6.6: Summary of systematic errors for the 1992 $\tau^- \rightarrow e^-\bar{\nu}_e\nu_\tau$ analysis.

| Source | Systematic Error |
|---|---|
| Electron Identification | 0.021 |
| Bhabha background | 0.042 |
| Internal background | 0.014 |
| Effc. energy dependence | 0.006 |
| Monte Carlo statistics | 0.037 |

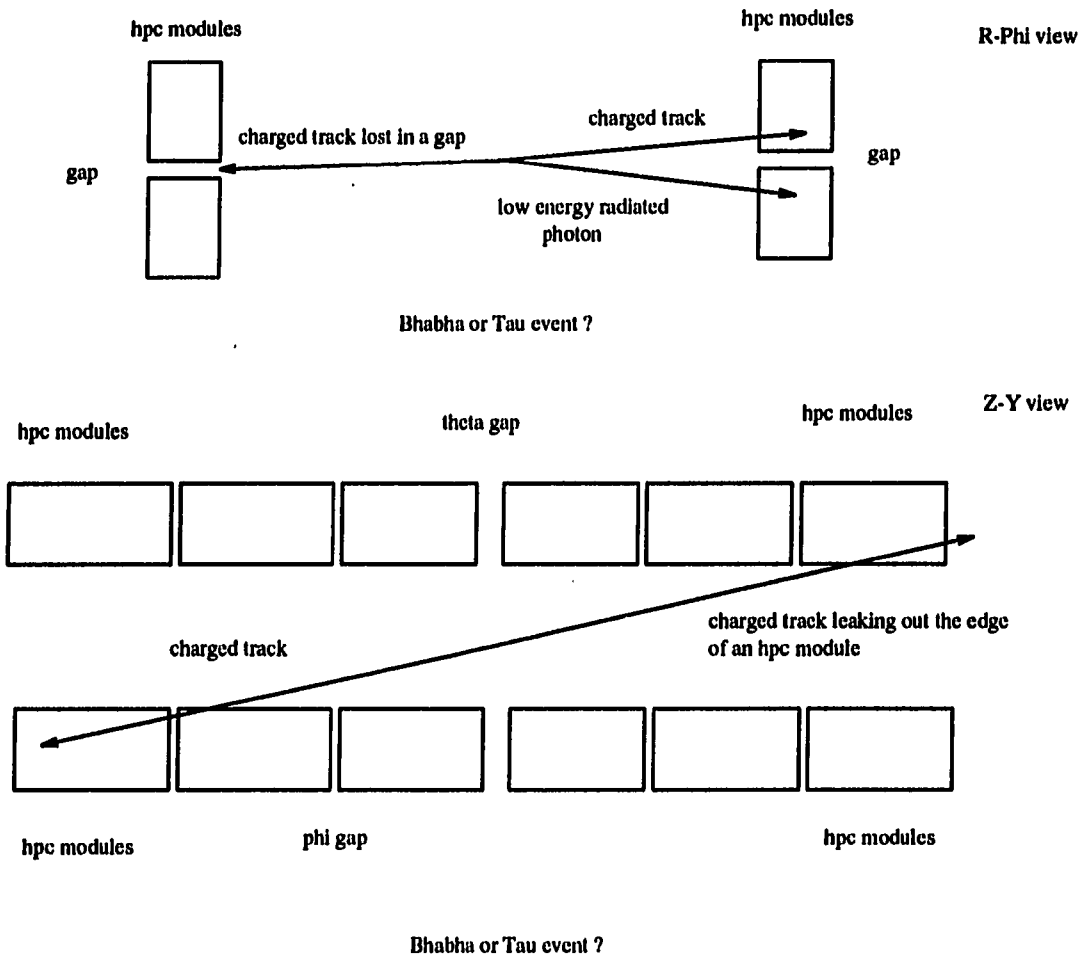


**Figure 6.1: Main difficulties in identifying $\tau^- \rightarrow e^- \overline{\nu}_e \nu_\tau$ events at DELPHI.**

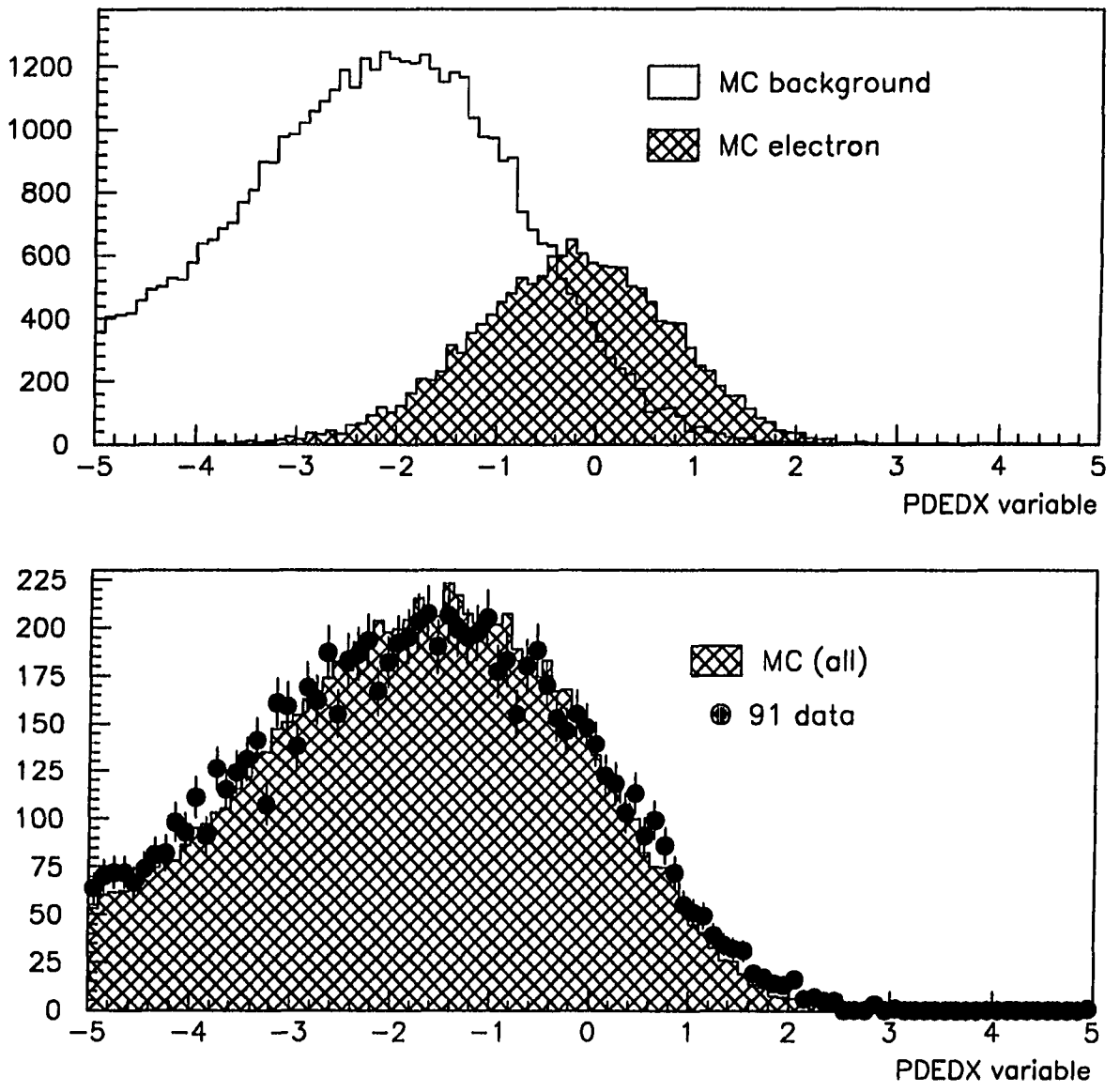


**Figure 6.2:** PDEDX variable. Tau Monte Carlo electron and background for electron mass expectation (top). 1991 data and tau Monte Carlo superimposed (bottom).

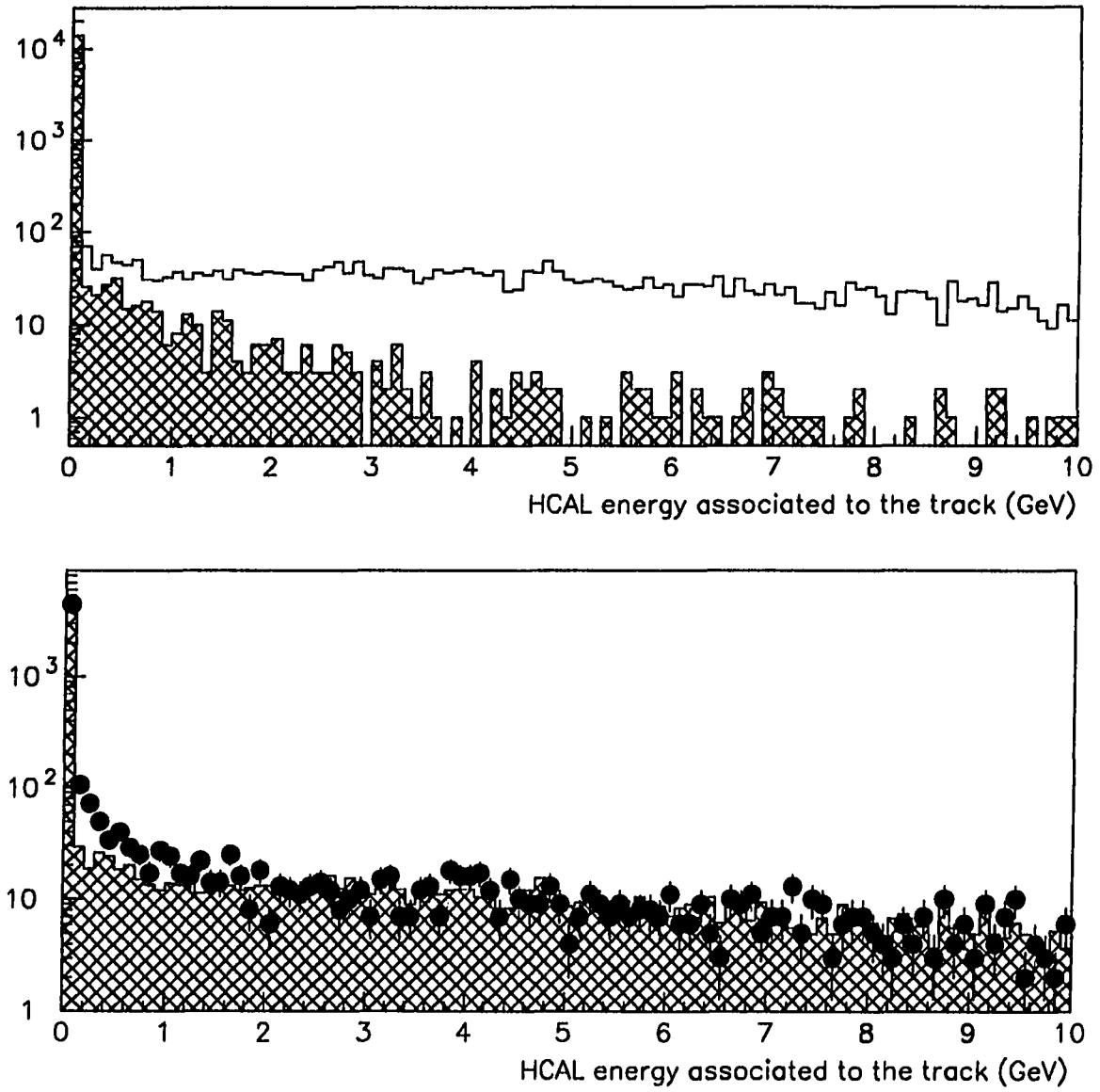


**Figure 6.3:** Tau Monte Carlo prediction for electrons (hatched) and internal background (solid line) in the HCAL (top). 1992 data (dots) and tau Monte Carlo (hatched) superimposed (bottom).

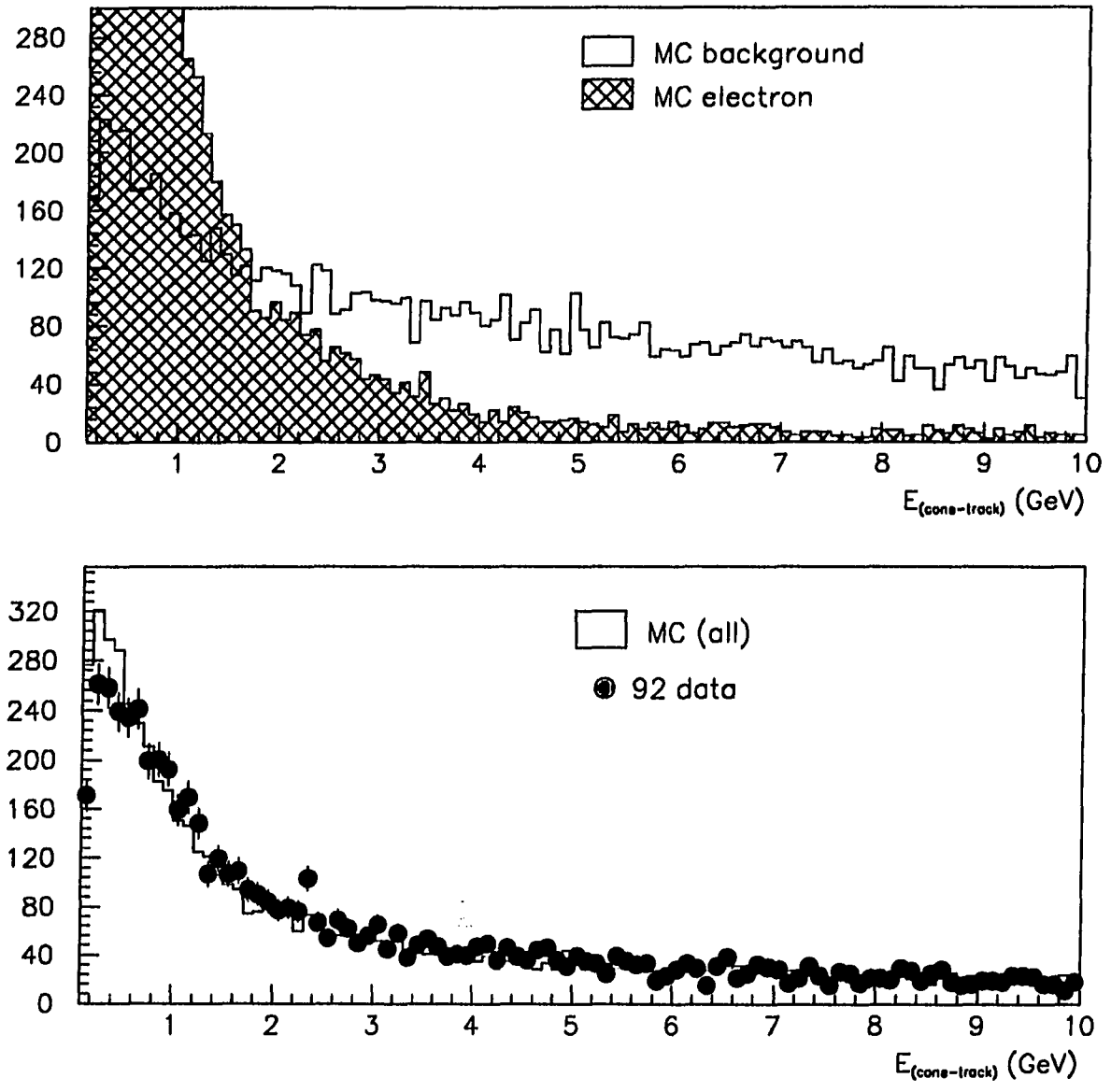


**Figure 6.4:** Unassociated energy in 30° cone. Tau Monte Carlo prediction for electron and background (top). 1992 data and tau Monte Carlo prediction superimposed (bottom).

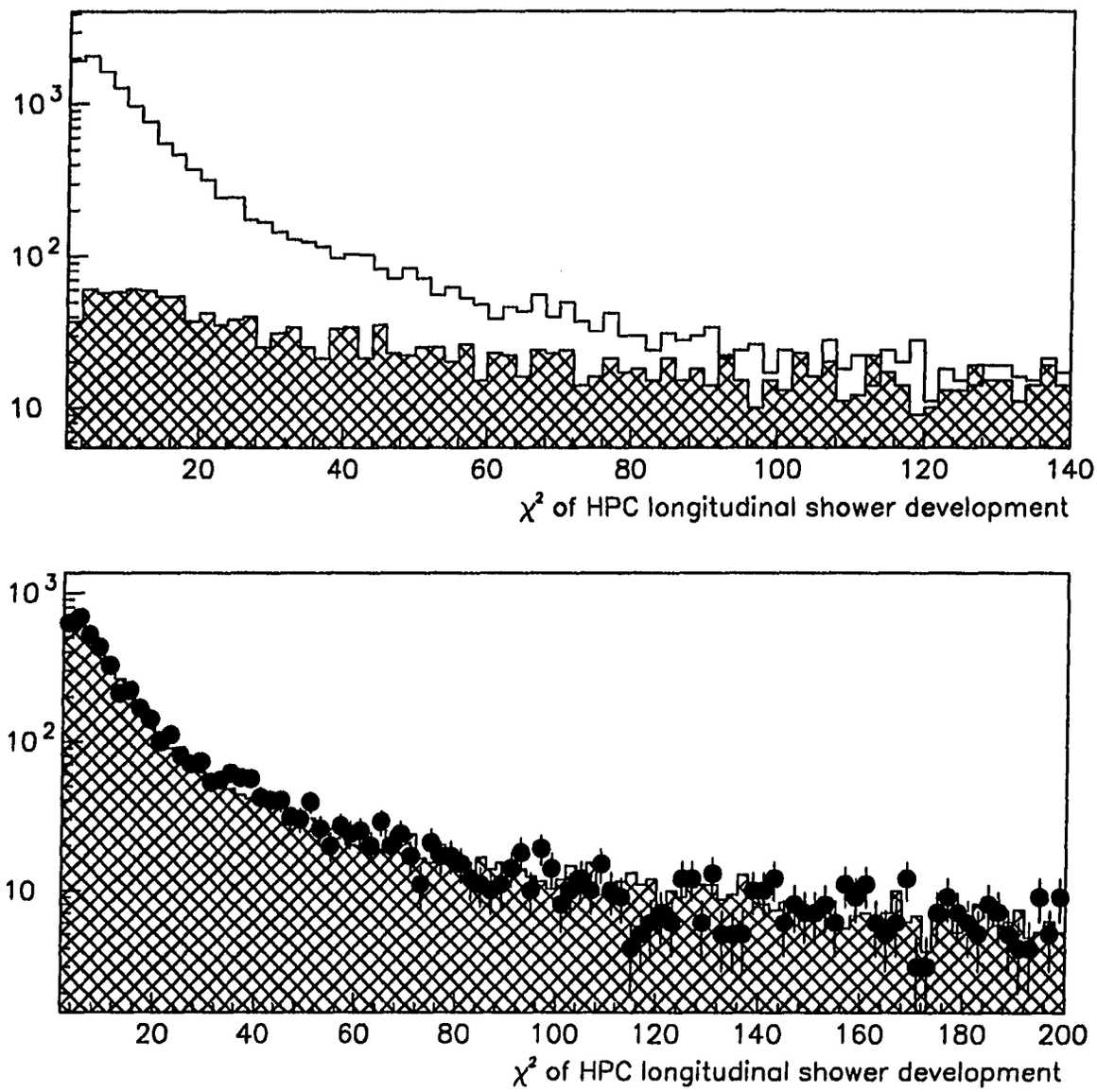


**Figure 6.5:** The $\chi^2$ of the shower profile. Tau Monte Carlo prediction for electron (solid line) and background (hatched) (top). 1992 data (dots) and tau Monte Carlo prediction (hatched) superimposed (bottom).

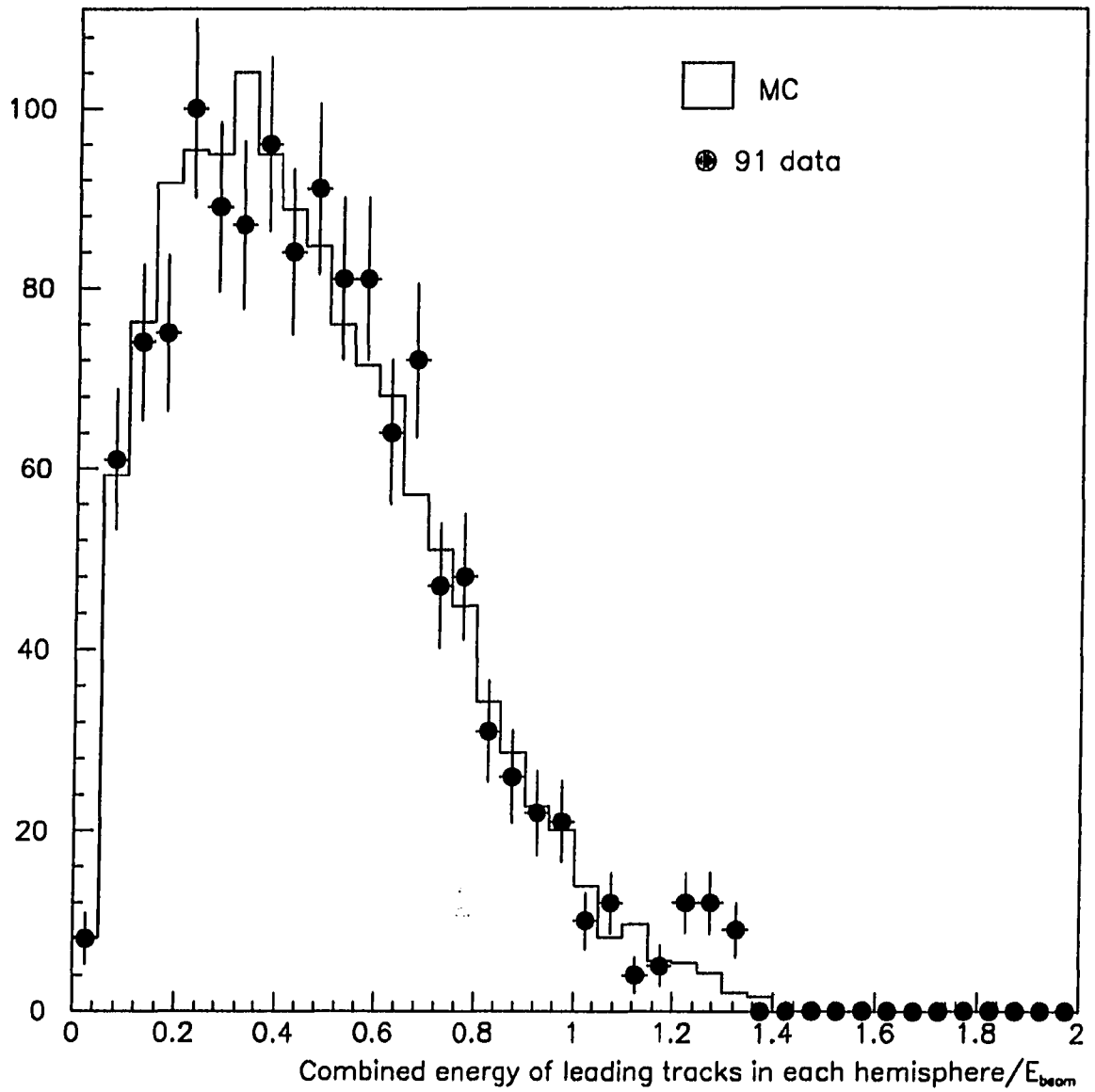


**Figure 6.6:** **Combined energies of the two leading tracks, before the rejection criteria for bhabhas are applied.**

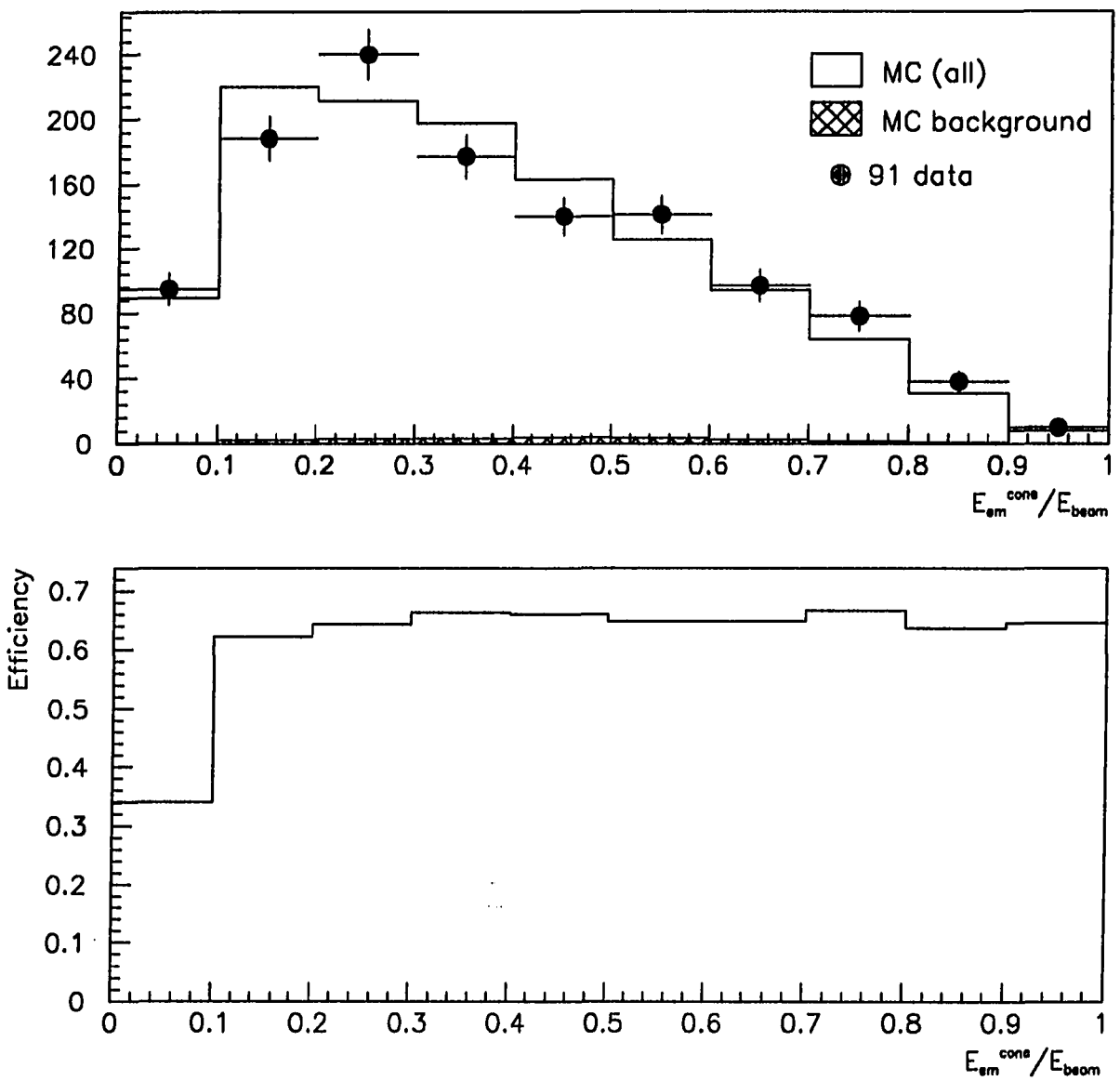


**Figure 6.7:** $E_{cone}/E_{beam}$ spectrum for 1991 data for $\tau^- \rightarrow e^-\overline{\nu}_e\nu_\tau$ candidates (top). Efficiency as a function of $E_{cone}/E_{beam}$ (bottom).

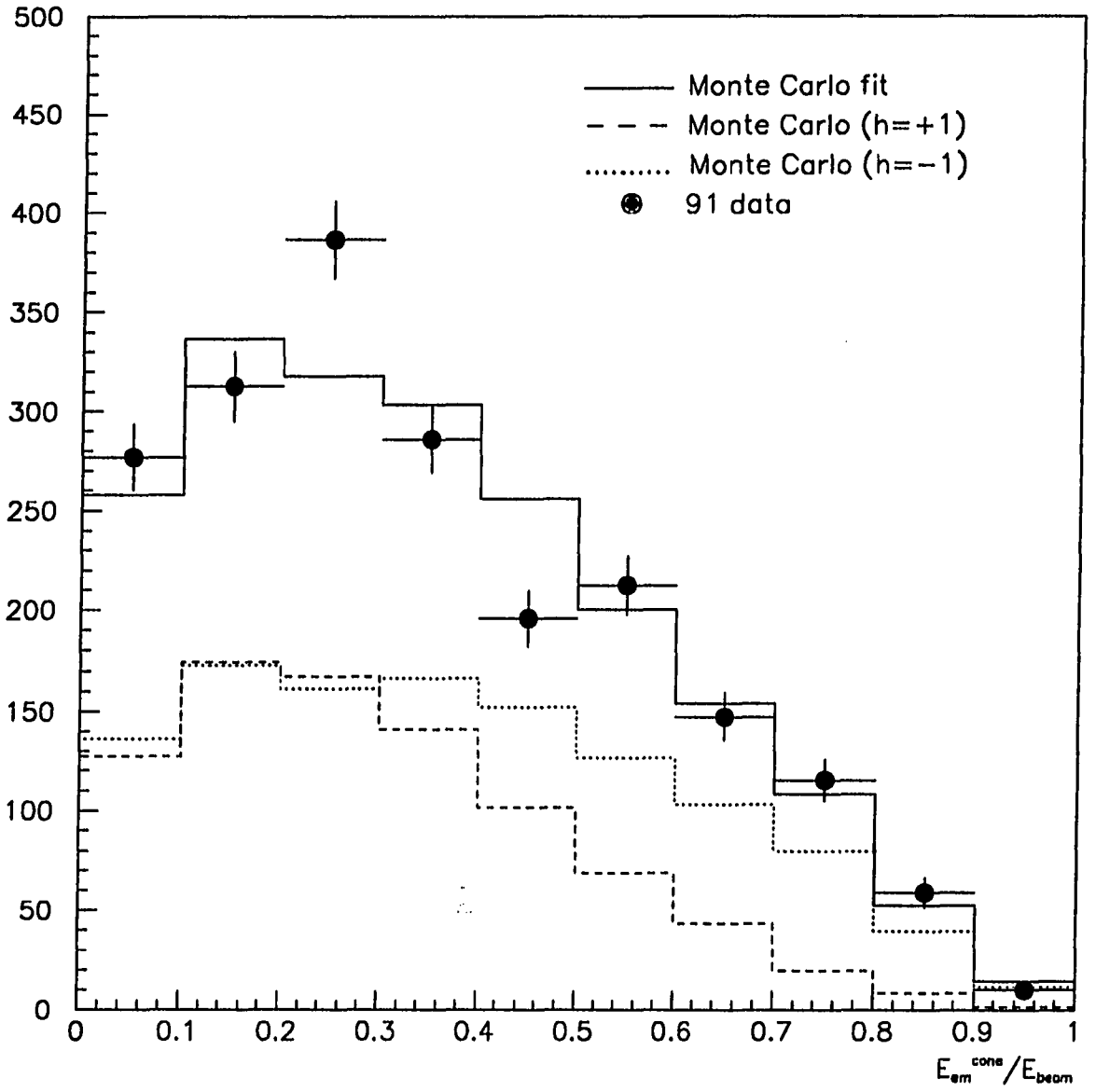


**Figure 6.8:** 1991 data fitted with tau Monte Carlo for electron candidates. The Monte Carlo positive and negative helicity components are also shown.

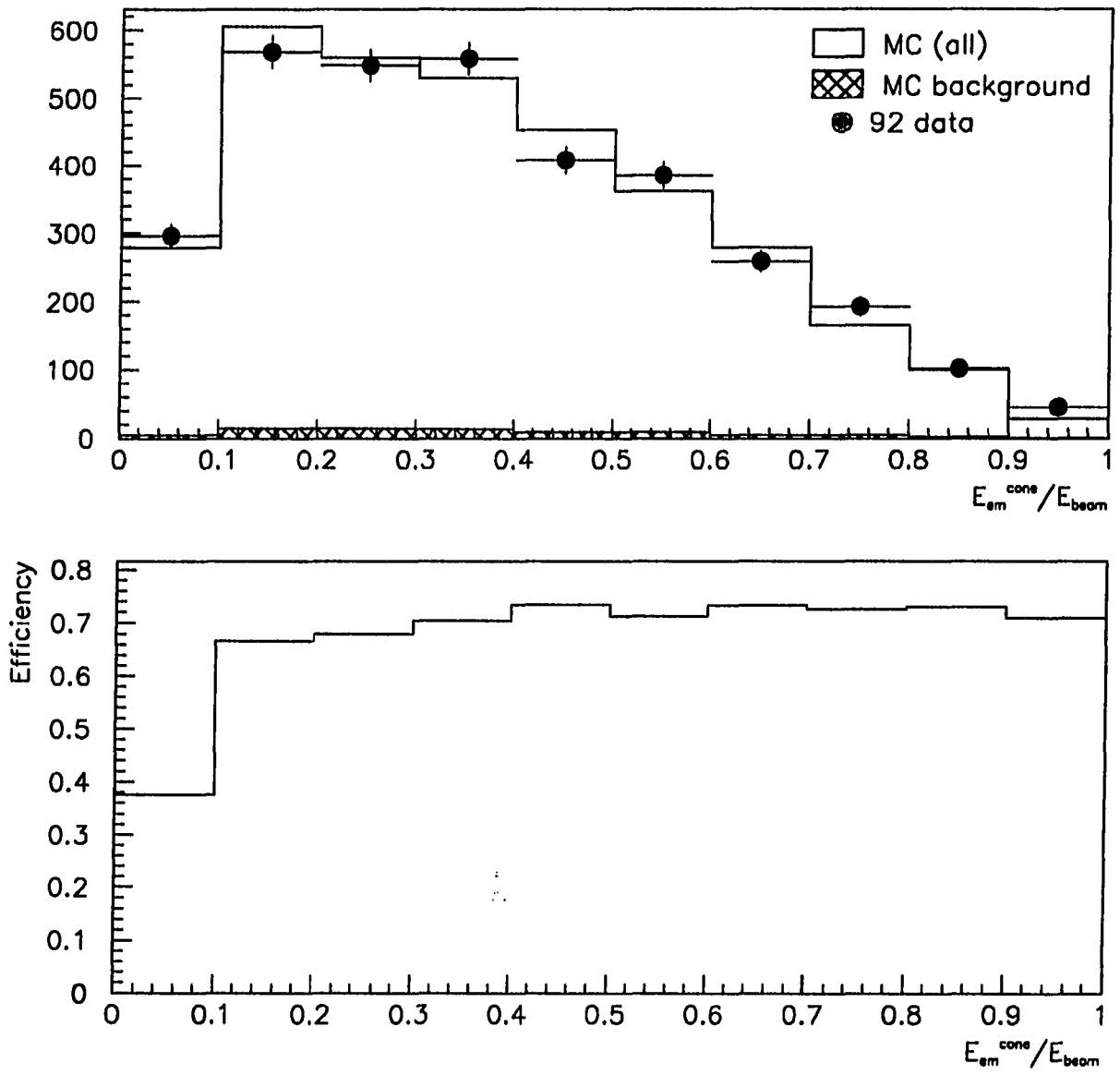


**Figure 6.9:** $E_{cone}/E_{beam}$ spectrum for 1992 data for $\tau^- \rightarrow e^-\overline{\nu}_e\nu_\tau$ candidates (top). Efficiency as a function of $E_{cone}/E_{beam}$ (bottom).

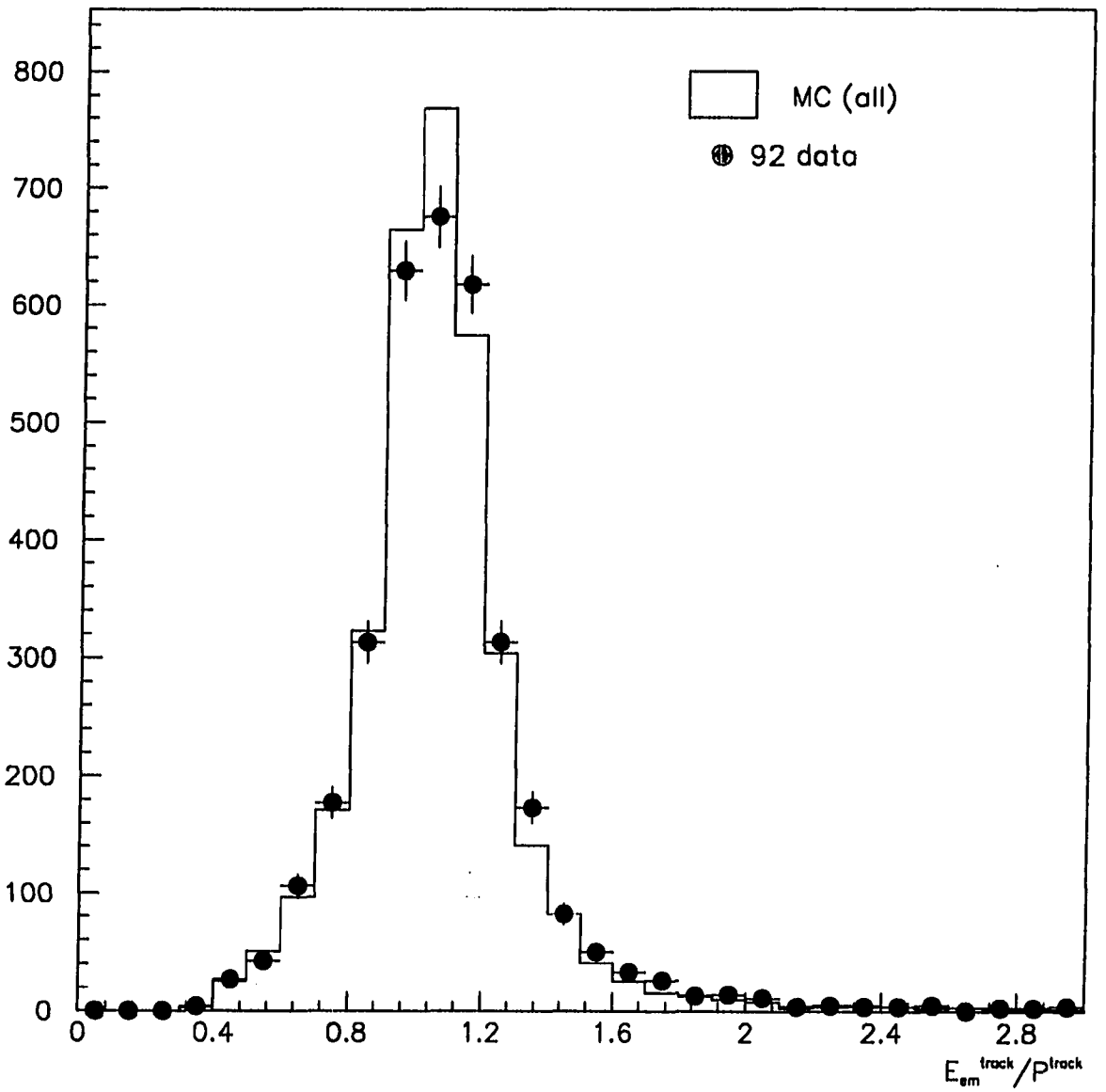


**Figure 6.10: E/P distribution for 1992 data for tau electron candidates.**

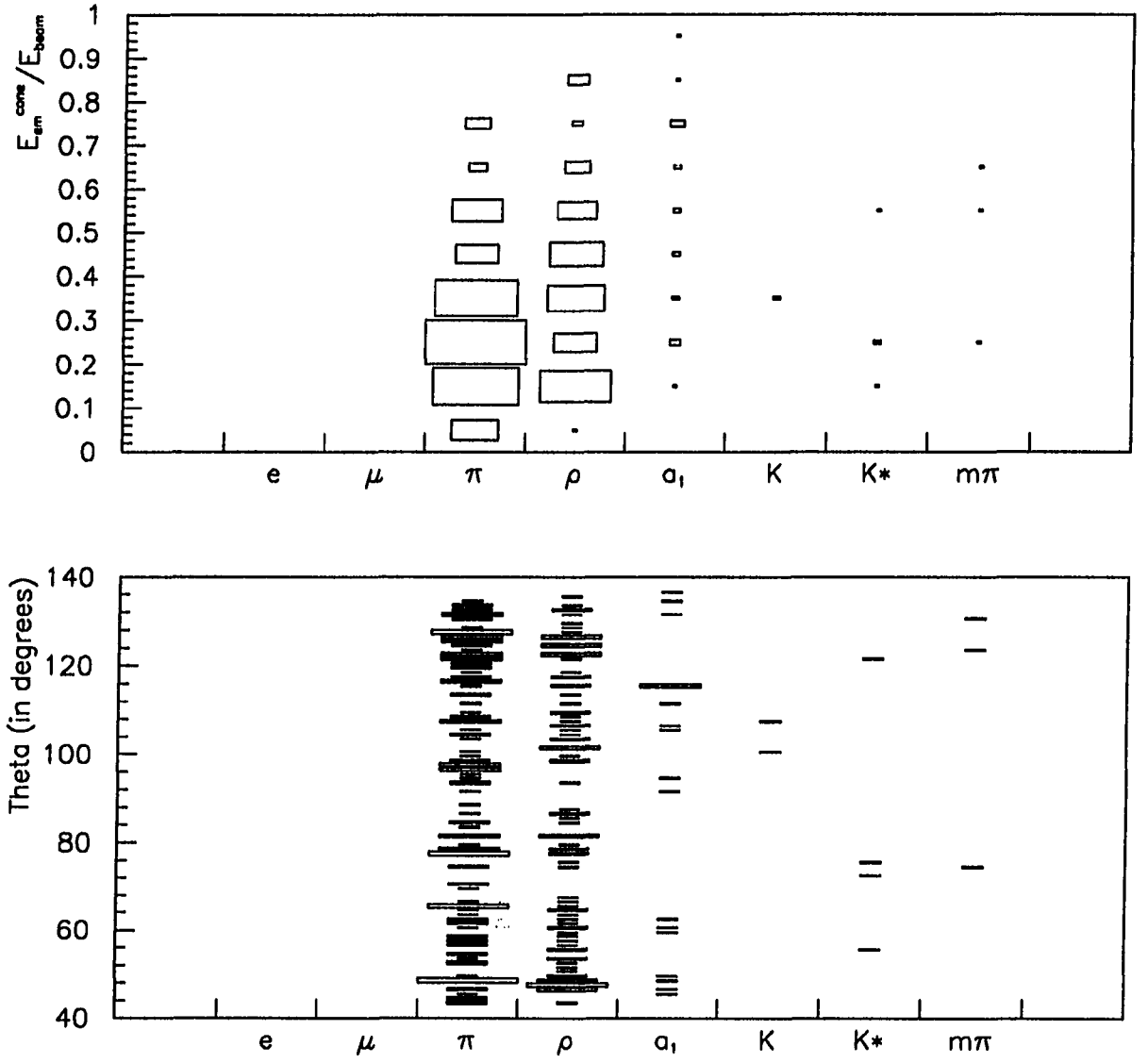


Figure 6.11: Tau Monte Carlo prediction for background as a function of $E_{em}^{cone}/E_{beam}$ (top) and as a function of $\theta$ (bottom).

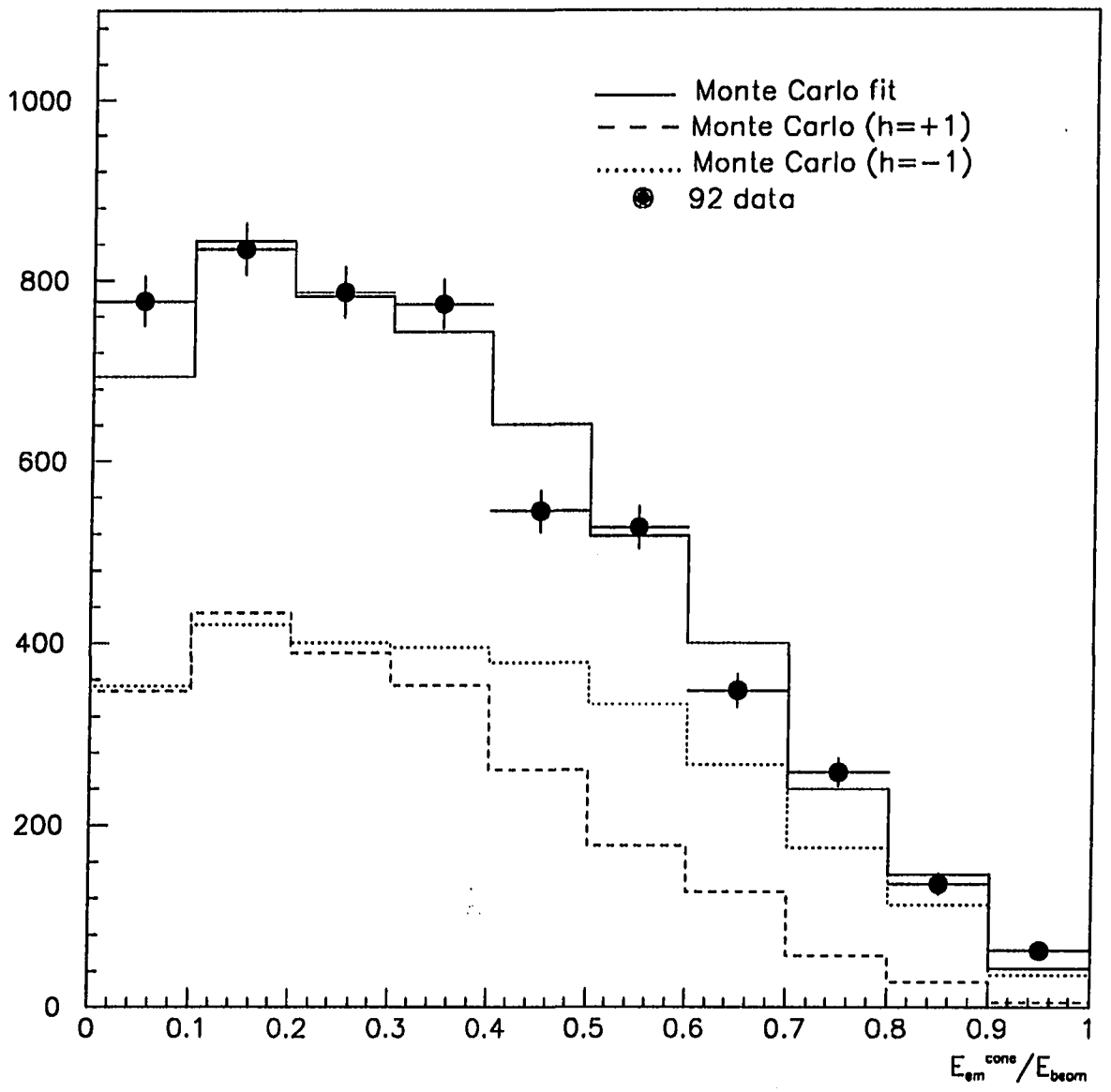


**Figure 6.12:** 1992 data fitted with tau Monte Carlo for electron candidates. The Monte Carlo positive and negative helicity components are also shown.

or because its energy is too low to be reconstructed or because it has converted into a low-energy $e^+e^-$ pair.

4. to remove background from $\tau^- \rightarrow e^-\overline{\nu}_e\nu_\tau$ decays when the track goes near or through a gap between HPC modules (Figure 6.13).

In order to insure a good understanding of the selection criteria, events whose tracks extrapolate to within 0.5° of the $\phi$-gaps between HPC modules have been excluded. In this case, the major background consists of low energy electrons that deposit little energy when they go through or near a $\phi$-gap, simulating a m.i.p. in the HPC (Figure 6.14). In addition, many rho events with low energy $\pi^0$'s (which may or may not leave a signal in the HPC) leave large signals in the OD when one or more photons convert, as opposed to the m.i.p. signal characteristic of pion events. This feature has been used to further suppress rho background in this channel.

Another problem with the angular coverage of the HPC occurs in the region near $\theta = 90^\circ$ (Figure 6.15). In this region, no calorimeter information exists, and electron/pion identification is very difficult. Therefore, tracks that extrapolate to within 3° of this gap are not selected.

The *EMIP* variable is defined as the sum of the energy deposited in the $1^{st}$ four layers of the HPC (corresponding to about $8X_0$)

$$EMIP = \sum_{i=1}^{i=4} E_{layer}. \tag{6.1}$$

Typically, a m.i.p. will deposit about 100 *MeV* in the HPC, uniformily across the layers. An electron, on the other hand, showers immeadiately, beginning usually in the very first layer (Figures 6.16 and 6.17). Therefore, this selection cut (which is dependent on the energy of the incident particle) is a powerful discriminator and allows for good $e/\pi$ separation. In addition, the unassociated energy around the charged track also provides a good separation between pions and background (electrons and rhos), since most of this unassociated energy belongs to radiated photons or daughter particles from $\pi^0$ decays. However, due to radiation from $\pi$ decays, this selection criterion is quite severe on the selection efficiency.

Arguably, the hardest task is the $\pi/\mu$ separation in the HCAL. High energy pions do not suffer from significant muon background, but low energy pions must overcome a very large, low-energy muon background, because these muons may not leave a signal in the MUB. The longitudinal segmentation of the HCAL is useful in separating pions and muons. Even at low energies, most muons will deposit energy in the outer layers of the HCAL, while low energy pions will rarely behave similarly. Therefore, a combination of *EPION* (see "Pion Identification"), energy deposition in the outer layers of the HCAL and MUB signal is used to separate the pion signal from the muon background (Figures 6.18, 6.19 and 6.20). Furthermore, muons of any energy may "leak out" at the edges of the MUB angular acceptance and leave no signal, faking a pion signature.

The background is dominated by muons at the edges of the MUB angular acceptance and by low momentum $\rho$'s and K*'s, whose photons were either lost in the $\phi$-gaps between HPC modules or were not reconstructed because their energies were too low.

### Selection Criteria

The procedure to select events in this channel is as follows:

- require 1-N topology, that is, 1 isolated track in one hemisphere and N tracks ($1 \leq N \leq 5$) in the other hemisphere (see "Event Selection");
- require PDEDX **NOT** compatible with an electron candidate,

$$PDEDX < 0.0 \quad (1991);$$

- require PDEDX compatible with a pion candidate (Figure 6.21). To keep the selection bias against high energy pions to a minimum, the selection requirement on PDEDX has been changed from the 1991 to the 1992 periods.

$$PDEDX < 1.86 \quad (1992);$$

- require track to point to the fiducial region, $51^\circ < \theta < 129^\circ$ (changed to $52^\circ < \theta < 128^\circ$ in 1992, because of the uncertainty in the HCAL edge effects);
- require $P > 0.05 \cdot E_{beam}$;
- require track extrapolation to HPC **NOT** point to a $\phi$ gap between modules, $(7^\circ < MOD(\phi, 15^\circ) < 8^\circ)$;
- require track extrapolation to HPC **NOT** point to the $\theta$ gap, $(87^\circ < \theta < 93^\circ)$;
- for further suppression of electron background, require <u>either</u> $E_{HPC} < 1.0$ GeV <u>or</u> $E_{HPC} > 1.0$ GeV and $EMIP < 0.4$ GeV;
- to suppress muon background, require <u>either</u> $EPION > 3.0$ GeV and no tracks in MUB beyond the $1^{st}$ layer <u>or</u> $EPION < 3.0$ GeV and no tracks in MUB and no energy deposition in the last HCAL layer;
- to suppress rho and electron background, require no unassociated energy be found in a $30^\circ$ cone around the track extrapolation to the HPC;
- to further suppress rho and electron background in the 1992 analysis, require OD tracks associated to TPC track $< 15$ (Figure 6.22).

### Results from 1991 Data Analysis

These selection criteria resulted in a sample of 605 $\tau^- \rightarrow \pi^-(K^-)\nu_\tau$ candidates in the 1991 data sample, with an overall efficiency in the fiducial region ($P > 0.05 \cdot E_{beam}$) of $52.55 \pm 1.14\%$ (Figure 6.23). The total internal background computed from Monte Carlo simulation is $8.99 \pm 0.50\%$, while the background from $\mu^+\mu^- \rightarrow \mu^+\mu^-$ events is $0.34 \pm 0.05\%$.

A selected sample of $\tau^- \rightarrow \mu^-\overline{\nu}_\mu\nu_\tau$ from 1991 data has been used to correct the internal muon background in this analysis. An overall correction factor of 1.026 to the total internal background has been applied, and the corrected internal background is $9.22 \pm 0.51\%$.

A 1-dimensional fit to the momentum spectrum ($X_p > 0.1$) (Figure 6.24) gives

$$P_\tau = -0.128 \pm 0.074(stat.) \pm 0.057(syst.).$$

Table 6.7 summarizes the sources of background in this analysis, and Table 6.8 summarizes the correction factors to background derived from a selected 1991 $\tau^- \rightarrow \mu^- \bar{\nu}_\mu \nu_\tau$ sample. The sources of systematic errors are described in Table 6.9.

### Results from 1992 Data Analysis

After these requirements, a total sample of 1613 $\tau^- \rightarrow \pi^-(K^-)\nu_\tau$ candidates are selected from the 1992 data. The overall efficiency in the fiducial region ($P > 0.05 \cdot E_{beam}$) is $56.35 \pm 1.0\%$ (Figure 6.25). The internal background computed from Monte Carlo is $8.97 \pm 0.47\%$ (Figure 6.26). The background from the other leptonic channels is negligible.

A 1-dimensional fit to the momentum spectrum (Figure 6.27) yields

$$P_\tau = -0.180 \pm 0.046(stat.) \pm 0.037(syst.).$$

Table 6.10 describes the background sources in this analysis, and the sources of the systematic errors are shown in Table 6.11.

## The $\tau^- \longrightarrow \rho^- \nu_\tau$ Channel

The criteria used to select $\tau^- \rightarrow \rho^- \nu_\tau$ candidates are based on the excellent spatial resolution of the HPC. Since the $\pi^0$ produced in the decay $\rho \rightarrow \pi\pi^0$ decays into two photons, the ability to detect and separate neutral electromagnetic showers is essential for this analysis. The ideal signature of the channel occurs when the two photons can be separated, their invariant mass reconstructed and found to be compatible with the mass of the $\pi^0$ (Figure 6.28), and the invariant mass of the $\pi - \pi^0$ system found to be compatible with the mass of the $\rho$. This requires that both photons be identified in the HPC, which in turn requires the $\pi^0$ to have sufficiently low energy so that the two photons are far apart enough to be reconstructed as two separate showers (Figure 6.29). About 60% of all $\rho$ candidates satisfy this requirement. These events have a $\pi\gamma\gamma$ topology. In the remaining 40% of the $\tau^- \rightarrow \rho^- \nu_\tau$

Table 6.7: Background sources for the 1991 $\tau^- \to \pi^-(K^-)\nu_\tau$ analysis.

| Decay mode | Background |
|---|---|
| $e\nu\overline{\nu}$ | $0.64 \pm 0.13\%$ |
| $\mu\nu\overline{\nu}$ | $1.57 \pm 0.21\%$ |
| $\rho\nu$ | $3.84 \pm 0.33\%$ |
| $a_1\nu$ | $0.14 \pm 0.06\%$ |
| $K*\nu$ | $2.80 \pm 0.28\%$ |
| multi-$\pi\nu$ | negligible |
| $e^+e^-$ | negligible |
| $\mu^+\mu-$ | $0.34 \pm 0.05\%$ |

Table 6.8: Correction factors to Monte Carlo predictions for the 1991 $\tau^- \to \pi^-(K^-)\nu_\tau$ analysis.

| $P_{track}/E_{beam}$ | Muon background |
|---|---|
| $0.0 \to 0.1$ | 1.70 |
| $0.1 \to 0.2$ | 1.23 |
| $0.2 \to 0.3$ | 1.03 |
| $0.3 \to 0.4$ | 1.04 |
| $0.4 \to 0.5$ | 2.16 |
| $0.5 \to 0.6$ | 0.70 |
| $0.6 \to 0.7$ | 0.68 |
| $0.7 \to 0.8$ | 1.00 |
| $0.8 \to 0.9$ | 1.00 |
| $0.9 \to 1.0$ | 1.00 |

Table 6.9: Summary of systematic errors for the 1991 $\tau^- \to \pi^-(K^-)\nu_\tau$ analysis.

| Source | Systematic Error |
|---|---|
| Pion Identification | 0.031 |
| Internal background | 0.034 |
| Acceptance | 0.029 |
| Pion simulation | 0.017 |

Table 6.10: Background sources for the 1992 $\tau^- \rightarrow \pi^-(K^-)\nu_\tau$ analysis.

| Decay mode | Background |
|---|---|
| $e\nu\overline{\nu}$ | $0.71 \pm 0.12\%$ |
| $\mu\nu\overline{\nu}$ | $2.86 \pm 0.27\%$ |
| $\rho\nu$ | $2.68 \pm 0.26\%$ |
| $a_1\nu$ | $0.18 \pm 0.06\%$ |
| $K*\nu$ | $2.52 \pm 0.25\%$ |
| multi-$\pi\nu$ | $0.02 \pm 0.02\%$ |
| $e^+e^-$ | negligible |
| $\mu^+\mu-$ | negligible |

Table 6.11: Summary of systematic errors for the 1992 $\tau^- \rightarrow \pi^-(K^-)\nu_\tau$ analysis.

| Source | Systematic Error |
|---|---|
| Pion Identification | 0.015 |
| Internal background | 0.019 |
| Acceptance | 0.018 |
| Pion simulation | 0.020 |

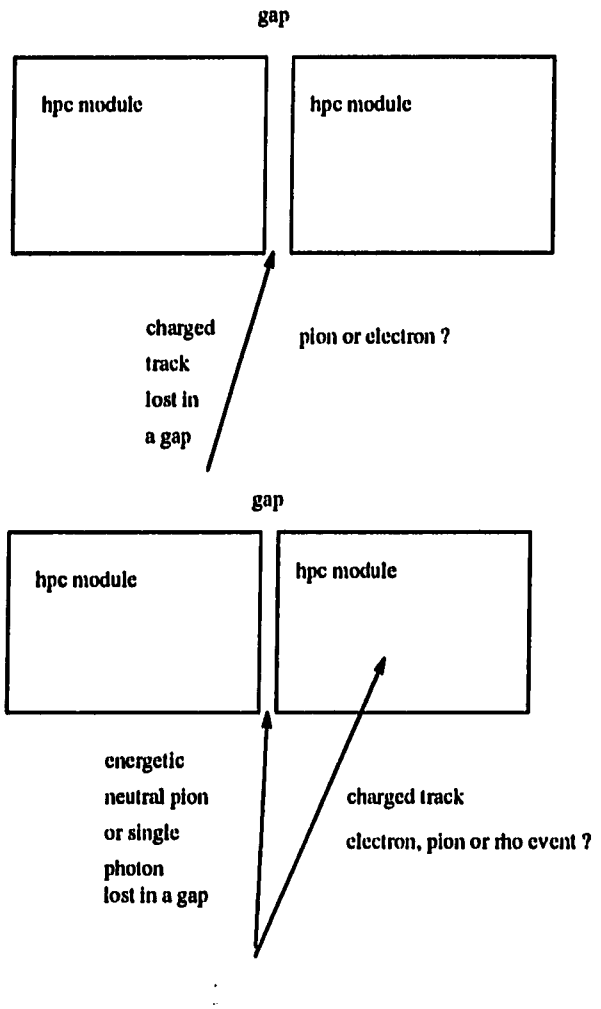


**Figure 6.13: Main difficulties in identifying $\tau^- \rightarrow \pi^- \nu_\tau$ events at DELPHI.**

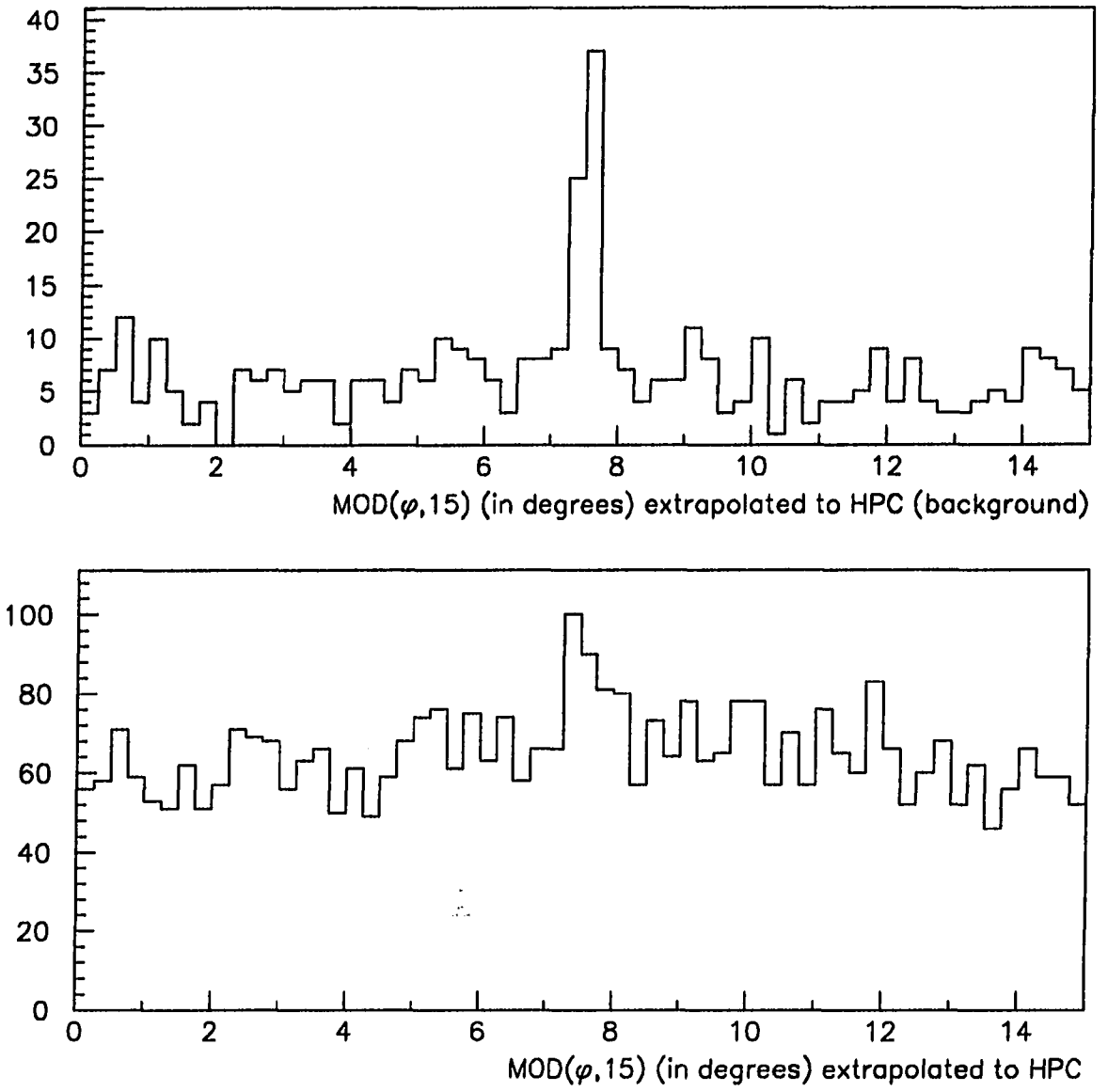


**Figure 6.14:** **Tau Monte Carlo prediction for background (top) and overall signal (bottom) as a function of $\phi$ angle.**

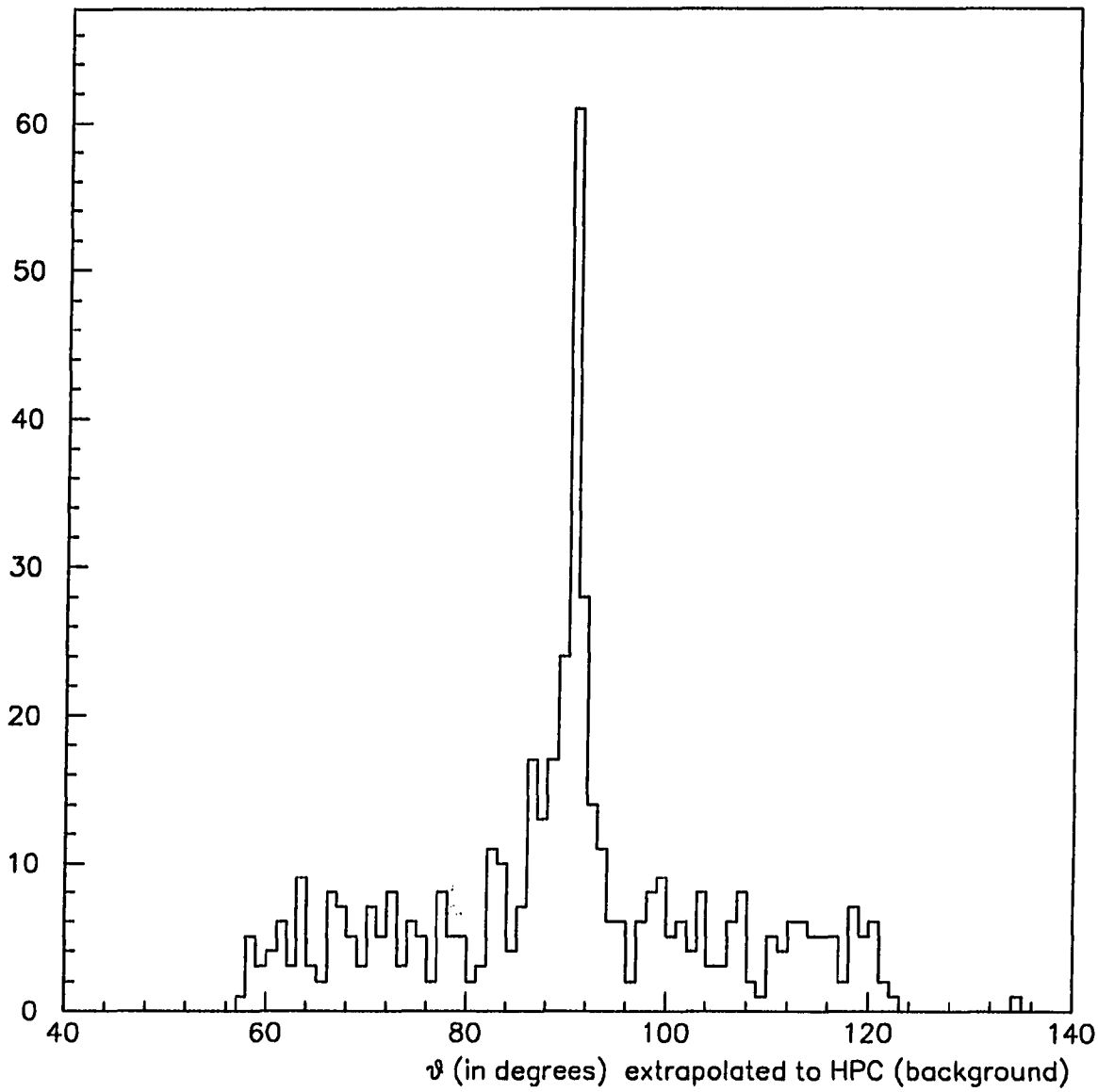


**Figure 6.15:** Tau Monte Carlo prediction for internal background to the $\tau^- \to \pi^- \nu_\tau$ channel as a function of $\theta$ angle.

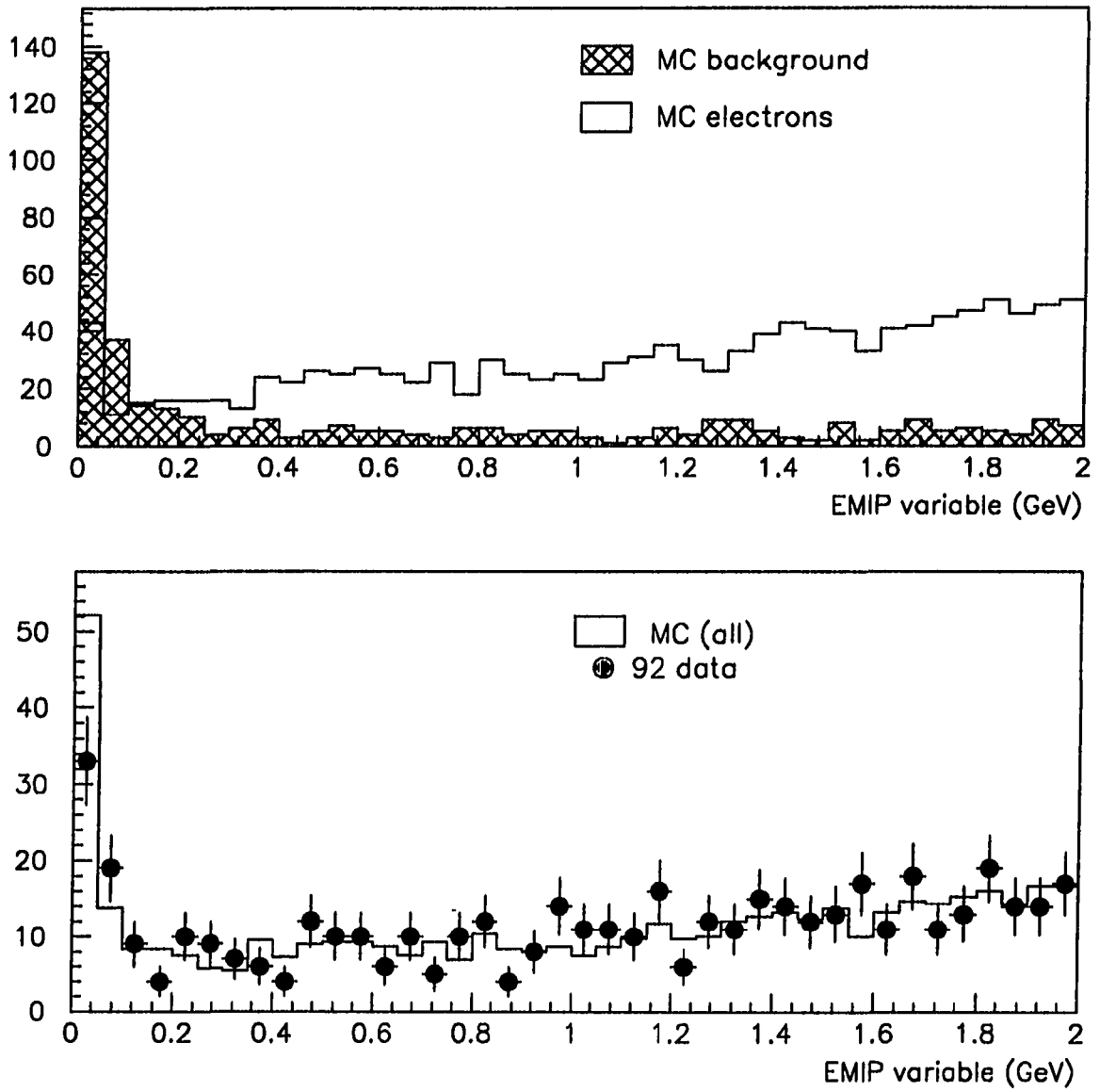


**Figure 6.16:** The EMIP variable. Tau Monte Carlo expectation for electrons and background (top). 1992 data superimposed with tau Monte Carlo prediction (bottom).

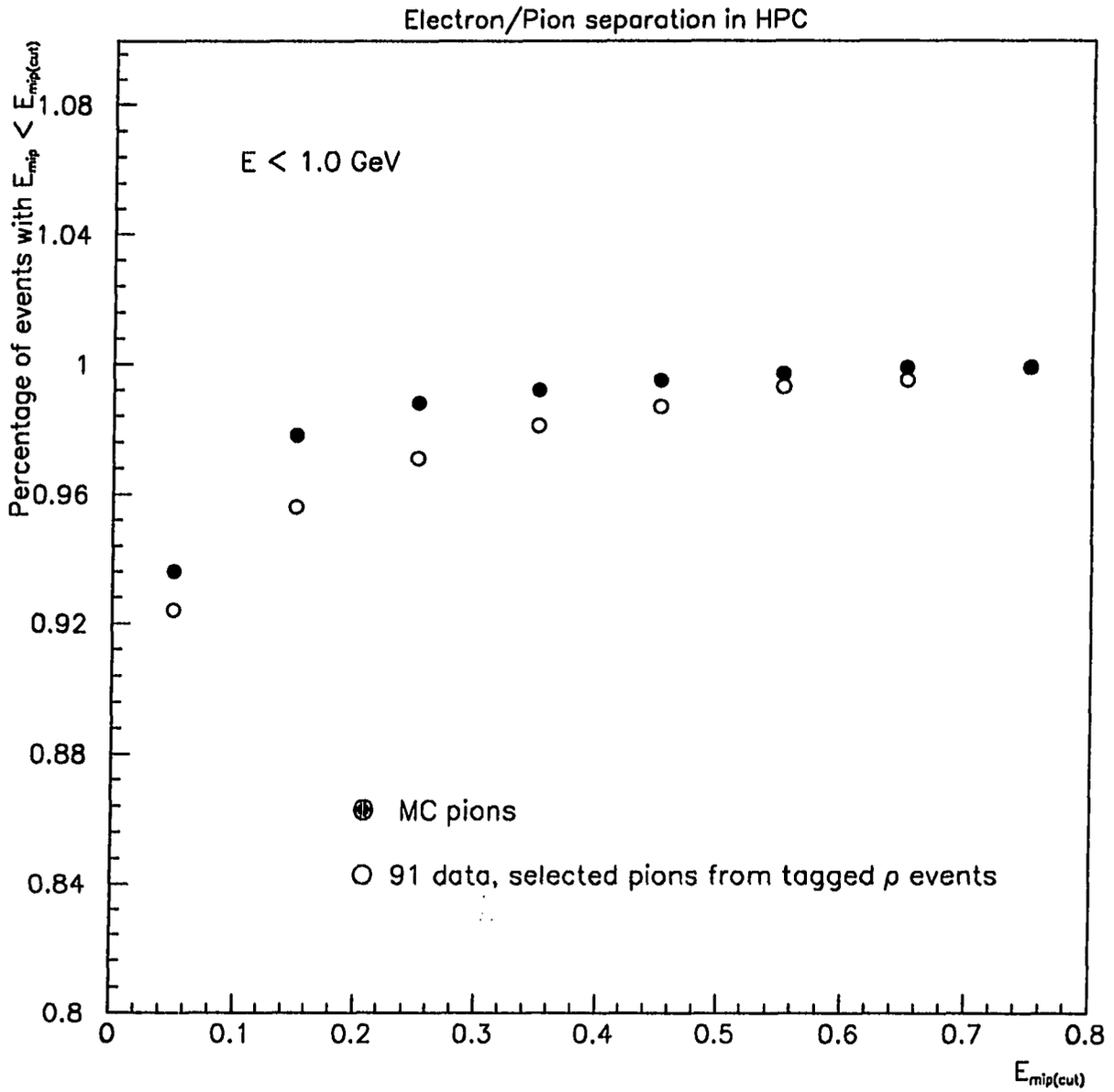


**Figure 6.17:** 1991 data and tau Monte Carlo prediction for the EMIP variable for pions in the HPC.

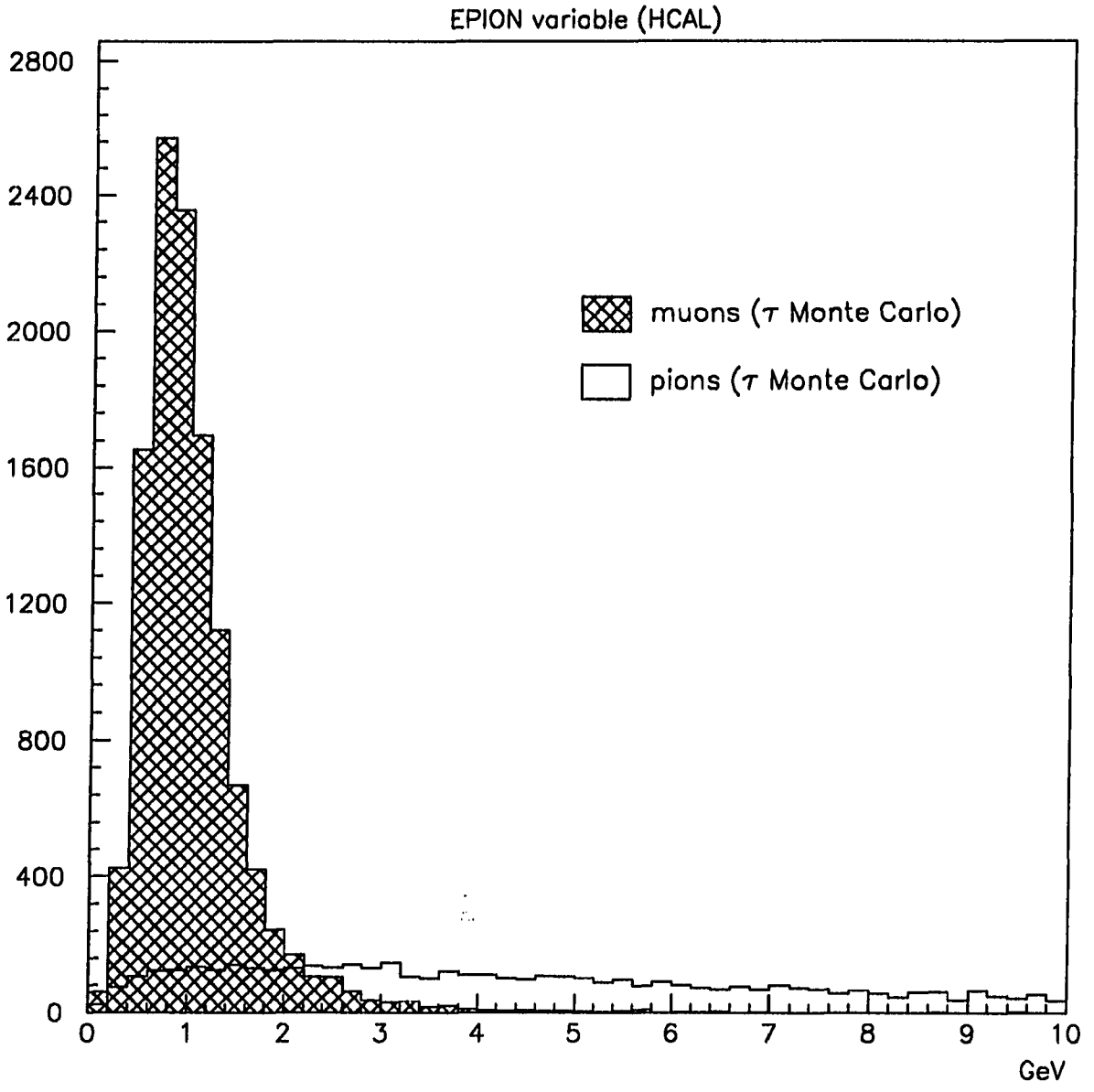


**Figure 6.18:** Tau Monte Carlo prediction of the EPION variable for muons and pions.

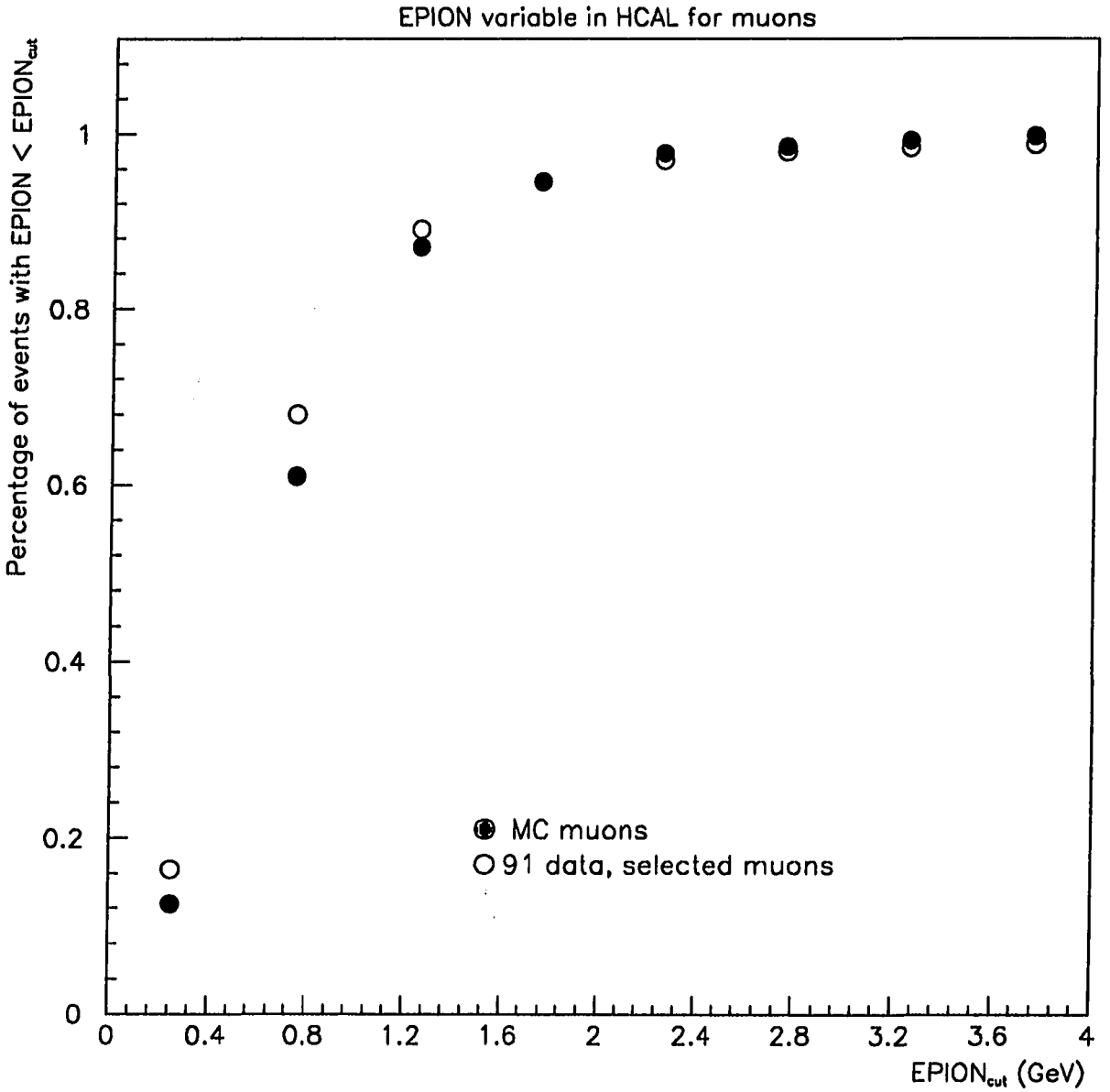


**Figure 6.19:** **1991 data and tau Monte Carlo prediction for the EPION variable for muons.**

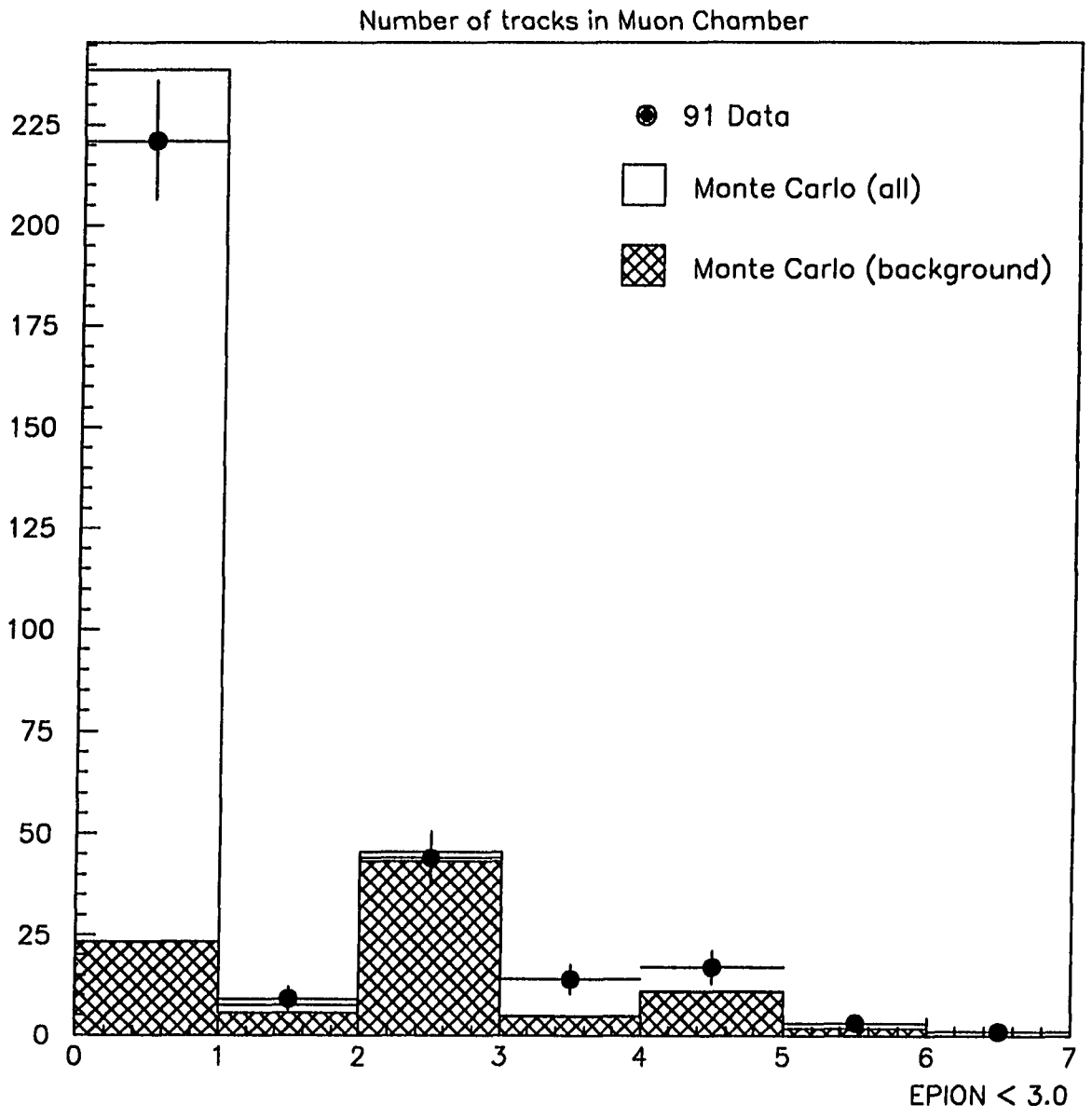


**Figure 6.20:** 1991 data and tau Monte Carlo prediction for signal and background superimposed for low momentum (EPION < 3.0 GeV) MUB tracks.

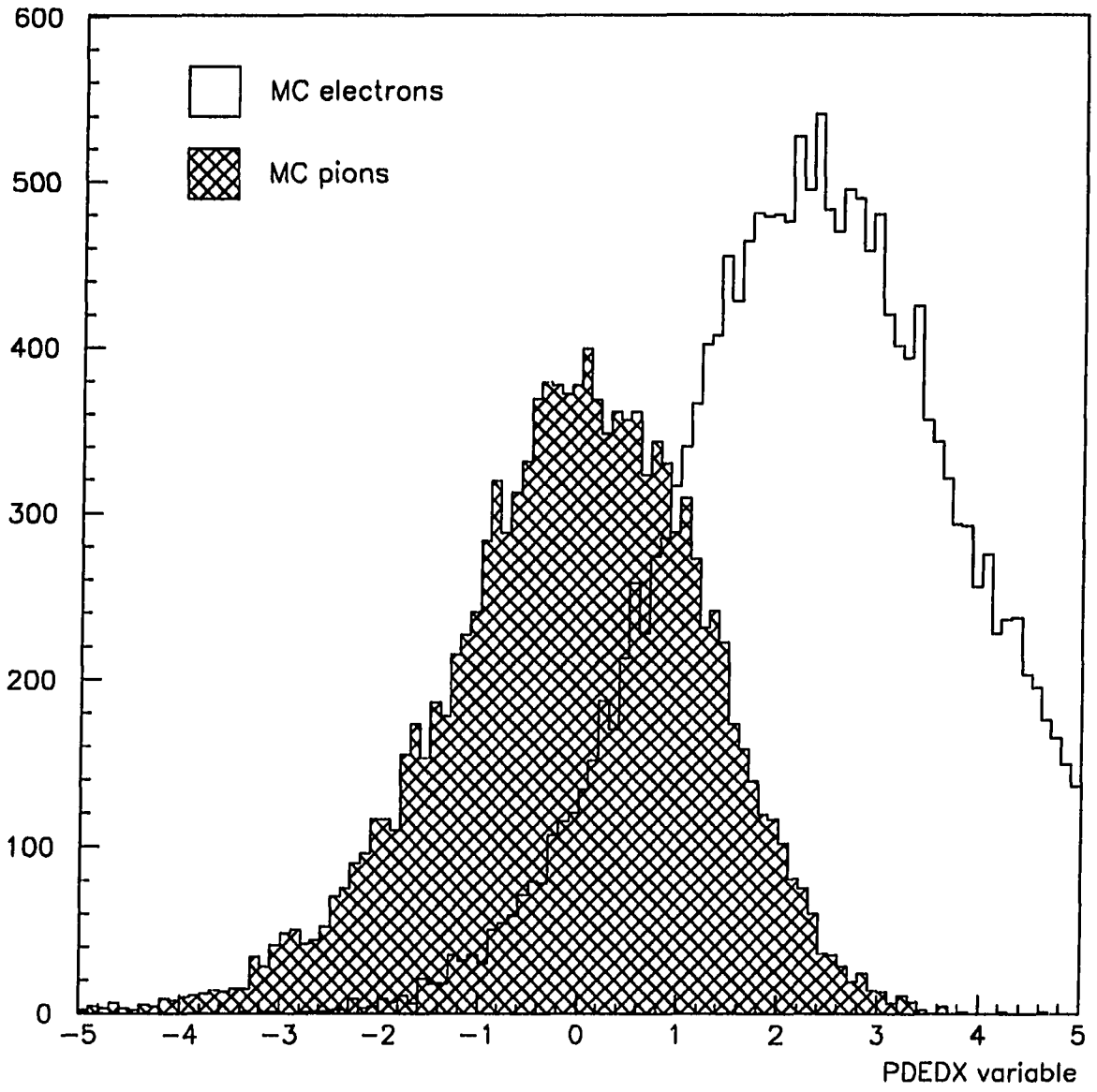


**Figure 6.21:** PDEDX variable. Tau Monte Carlo electron and pion prediction for pion mass expectation.

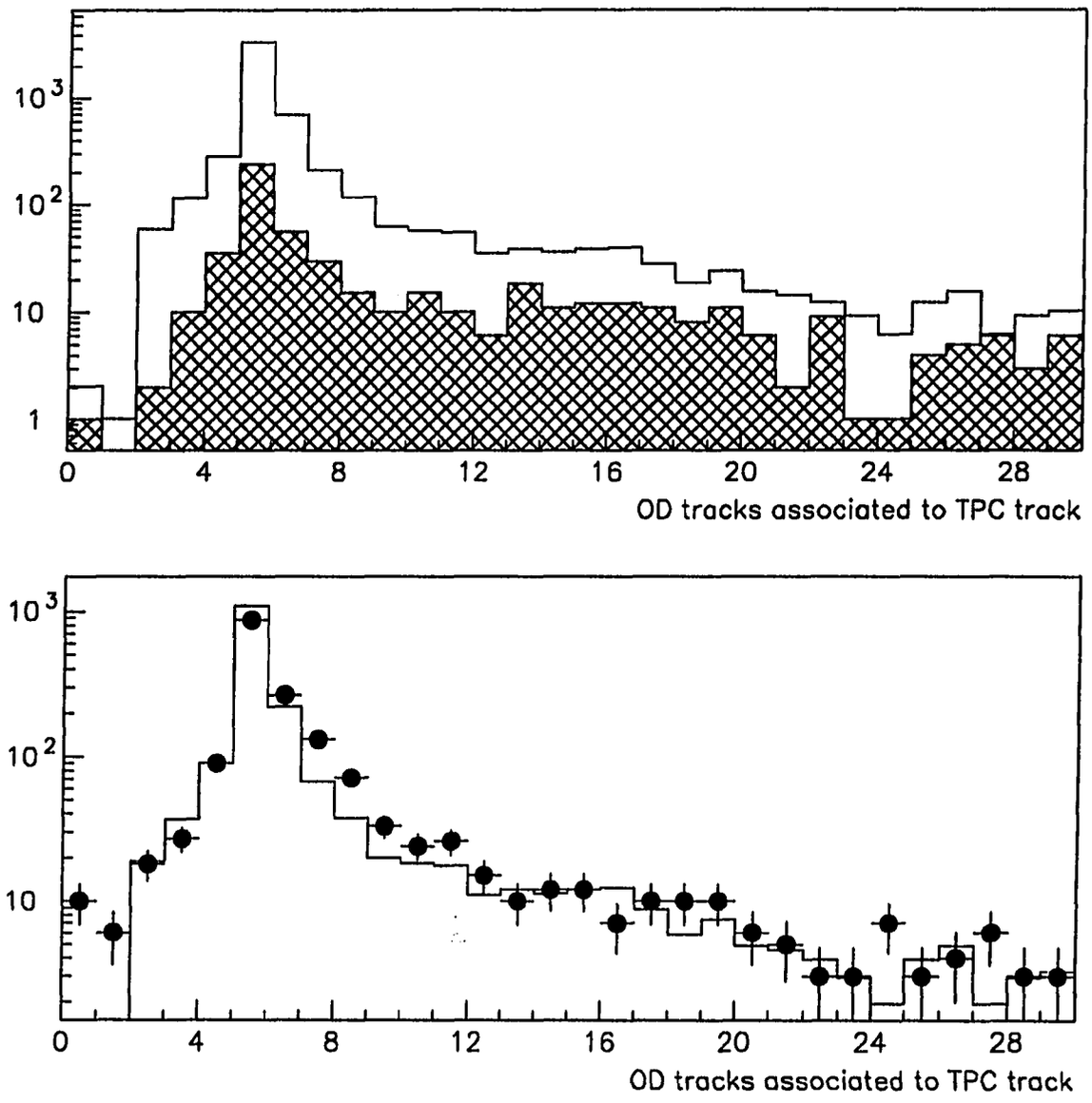


**Figure 6.22:** Tau Monte Carlo prediction for pion (solid line) and background (hatched) for OD tracks (top) and 1992 data (dots) and tau Monte Carlo (solid line) prediction after selection (bottom).

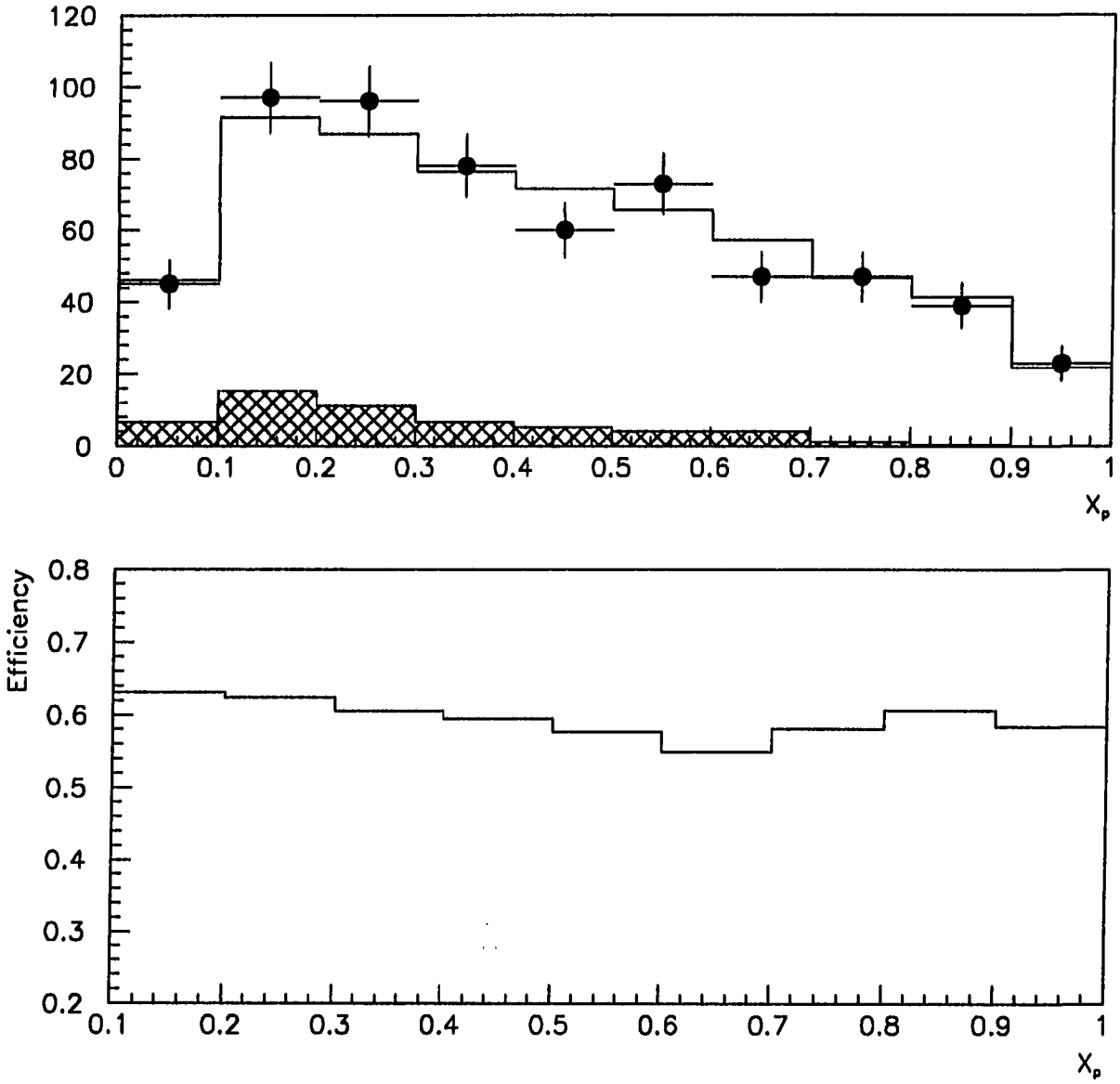


Figure 6.23: 1991 data (dots) $X_p = P_{track}/E_{beam}$ spectrum for $\tau^- \rightarrow \pi^-\nu_\tau$ candidates (top), superimposed with tau Monte Carlo prediction for signal (solid line) and background (hatched). Efficiency as a function of $X_p = P_{track}/E_{beam}$ (bottom).

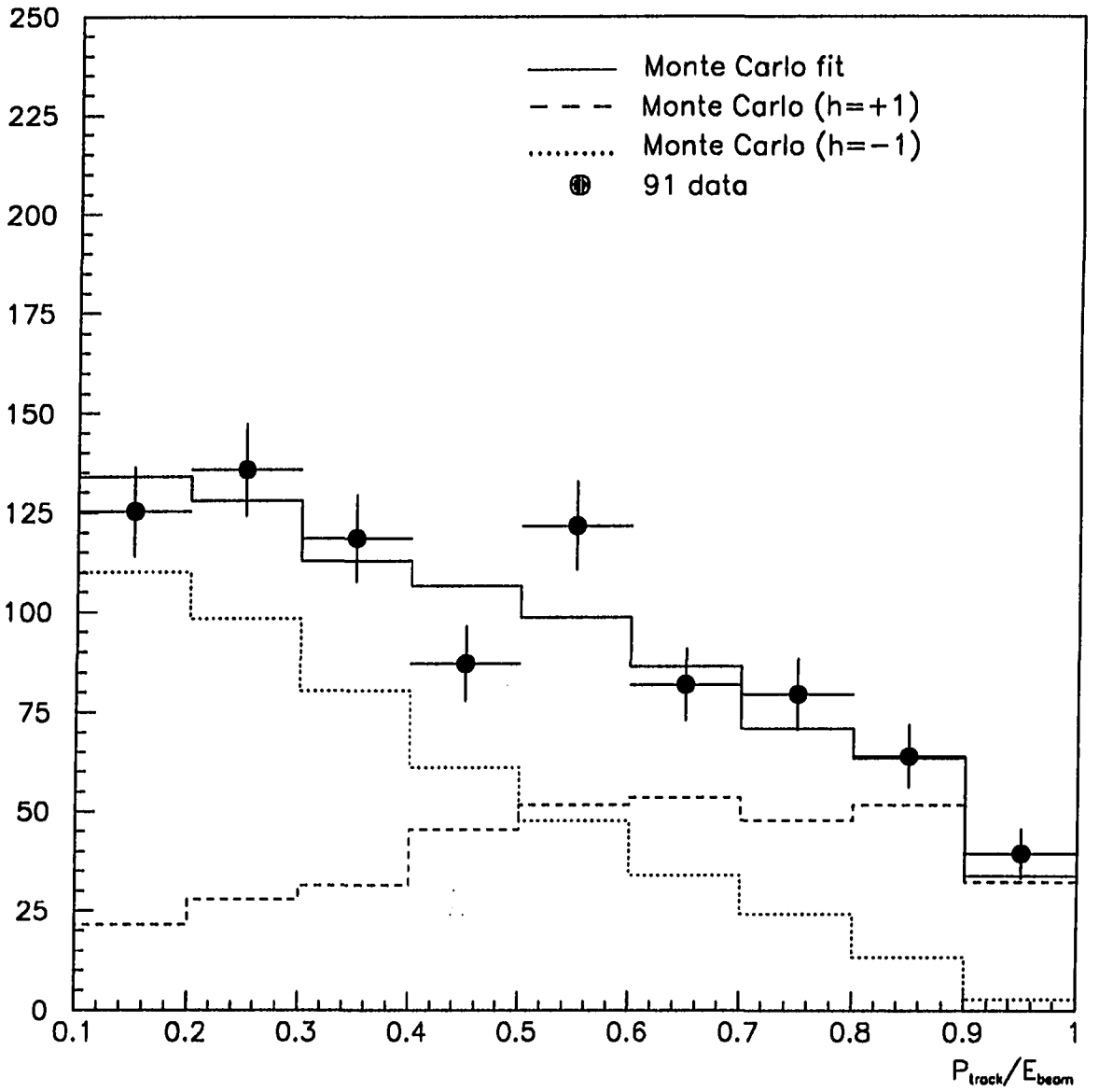


**Figure 6.24:** 1991 data fitted with tau Monte Carlo for pion candidates. The Monte Carlo positive and negative helicity components are also shown.

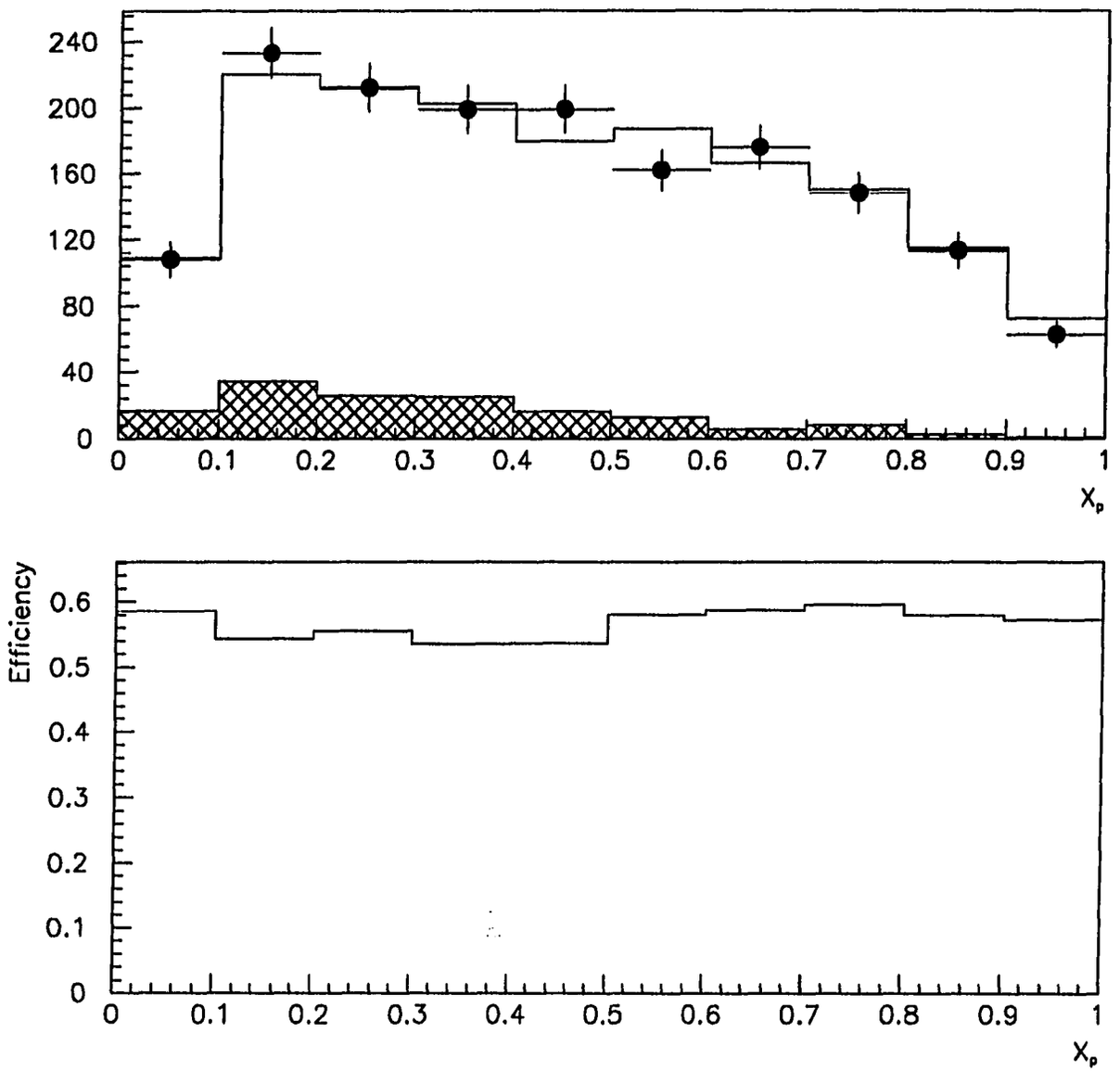


Figure 6.25: 1992 data (dots) $X_p = P_{track}/E_{beam}$ spectrum for $\tau^- \to \pi^-\nu_\tau$ candidates (top), superimposed with tau Monte Carlo prediction for signal (solid line) and background (hatched). Efficiency as a function of $X_p = P_{track}/E_{beam}$ (bottom).

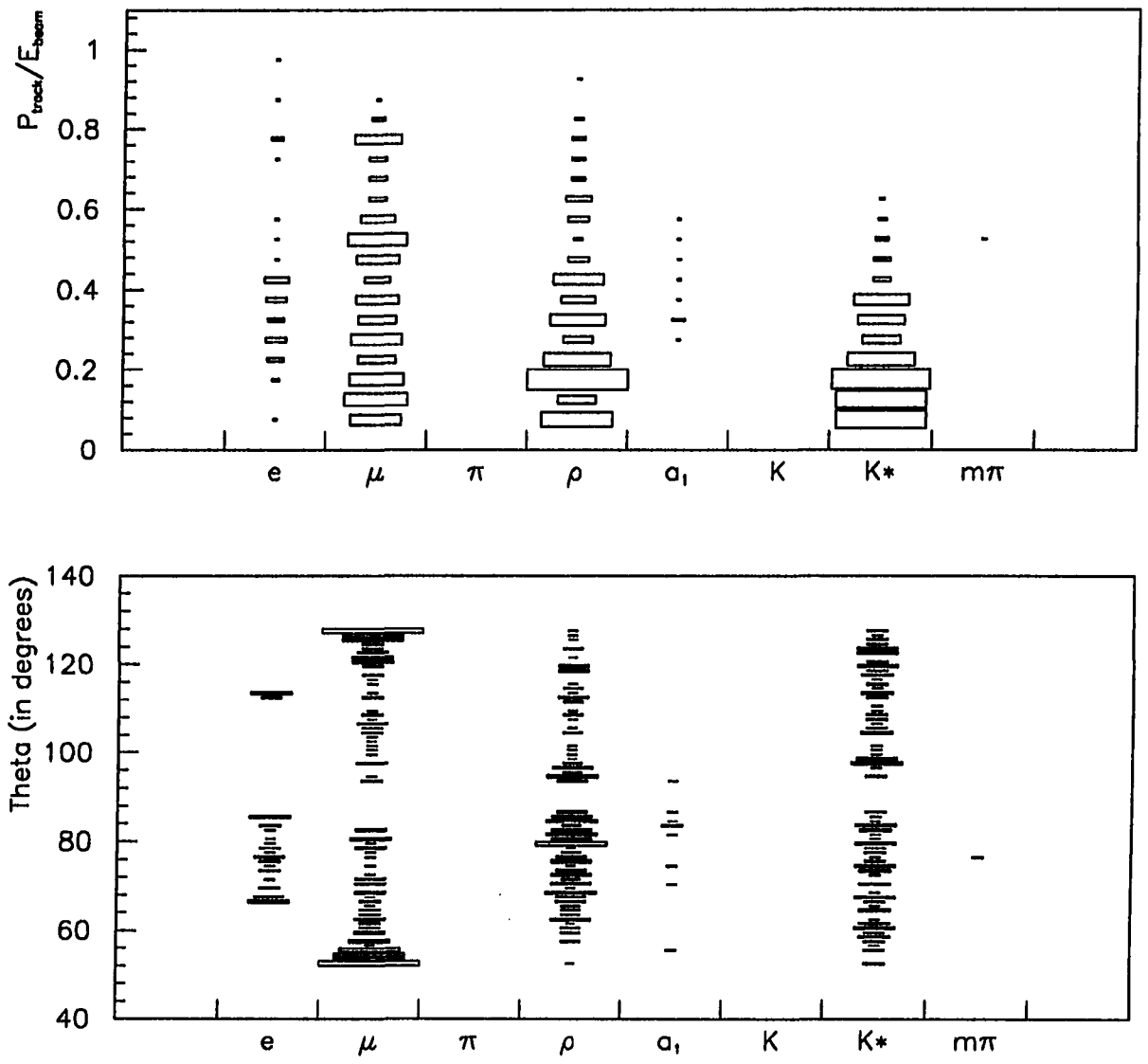


**Figure 6.26:** Background as a function of $P_{track}/E_{beam}$ (top) and $\theta$ (bottom) per individual internal channel.

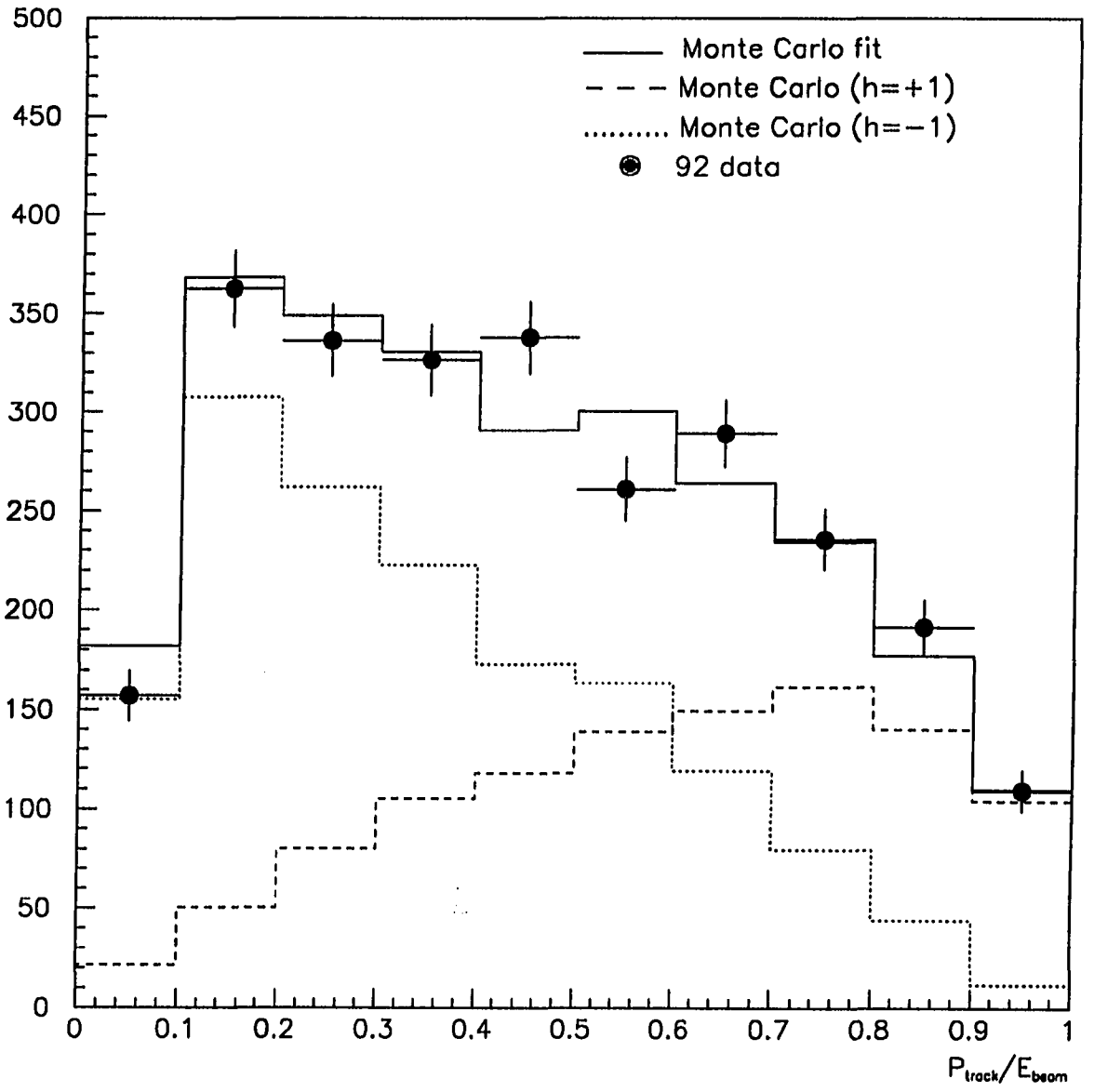


**Figure 6.27:** 1992 data fitted with tau Monte Carlo for pion candidates. The Monte Carlo positive and negative helicity components are also shown.

candidates, one of the photons was lost either because it entered one of the gaps between HPC modules or because it could not be reconstructed due to a late conversion (beyond the TPC outer wall) into a $e^+e^-$ pair or due to having too low an energy to be reconstructed in the HPC. These events have a $\pi\gamma$ topology. In addition, events with energetic $\pi^o$'s that decay into two photons which are too close to be separated as two separate neutrals in the HPC also appear with a $\pi\gamma$ signature (Figure 6.30).

In selecting photons from $\pi^o$ decays, one expects them to move close to the original flight path of the parent particle due to the Lorentz boost at LEP energies. The same reasoning applies to the daughter particles of the $\rho$ decay, so one can conclude that the photons move close to the flight path of the charged pion. Therefore, an imaginary cone of $30^o$ built around the track extrapolation to the HPC is used in the selection criteria to remove extraneous neutrals and other background events.

A combination of a PDEDX (for low energy particles) and a EMIP (for high energy particles) cut is necessary, to insure a reliable identification of the charged track as a pion. Moreover, because of the potential overlapping of $\pi$'s with photons from $\pi^o$'s in the HPC (resembling an electron shower), the cut on the EMIP variable must be very loose, to avoid losing too many candidates.

To minimize electron and $a_1$ background, a cut has been placed on reconstructed $M_{\pi^o}$ (1992 analysis only) and $M_\rho$ invariant masses. In addition, to further suppress $a_1$ background, cuts have been imposed on the energy of each photon (1991 analysis only).

A photon is defined as any neutral shower that meets the following requirements (Figure 6.31):

1. $E_{neutral} > 0.5$ GeV;

2. the neutral shower deposits energy in at least 3 consecutive layers in the HPC.

The background in this analysis comes mainly from various internal channels. Low energy electrons that radiate one or more photons will appear as a low energy charged particle accompanied by a one or more neutral particles, which is the expected signature of a $\tau^- \rightarrow \rho^-\nu_\tau$ event. The ideal signature of the $a_1^- \rightarrow \pi^-\pi^o\pi^o \rightarrow \pi^-\gamma\gamma\gamma\gamma$ decay is one identified charged track and 4 neutral showers in the HPC.

However, due to gaps between HPC modules and an average of 1 radiation length of material in front of the HPC, one or more photons from an $a_1$ decay can be lost or converted, so an $a_1$ decay may appear in the HPC as a $\rho$ decay. Additional internal background comes from $\pi$ decays with radiated photons, from $\tau^- \rightarrow K*^- \nu_\tau \rightarrow K^-\pi^0\nu_\tau$ decays (since $\pi$'s and K's are indistinguishable without the BRICH) and from non-resonant $\tau^- \rightarrow \pi^-(m)\pi^0\nu_\tau$ $(m \geq 2)$ decays.

### Selection Criteria

After selecting all events with neutrals that meet the photon requirements, the following selection criteria are applied to the data sample to obtain the $\rho$-enriched sample:

- require 1-N topology, that is, 1 isolated track in one hemisphere and N tracks $(1 \leq N \leq 5)$ in the other hemisphere (see "Event Selection");
- require the track to point into the fiducial region, $43^\circ \leq \theta \leq 137^\circ$;
- require one track + N photons $(1 \leq N \leq 2)$ in the hemisphere of interest, to suppress $a_1$ background (Figure 6.32);
- require photons to lie inside a 3 dimensional $30^\circ$ cone around the track, to minimize the misidentification of $\pi^0$ photons;
- require PDEDX NOT compatible with an electron candidate,

$$PDEDX < -0.1 \text{ (1991)};$$

- require PDEDX compatible with a pion candidate (Figure 6.33). To keep the selection bias against high energy pions to a minimum, the selection requirement on PDEDX has been changed from the 1991 to the 1992 periods.

$$PDEDX < 2.2 \text{ (1992)};$$

- to maximize selection efficiency for energetic rhos, require $EMIP < 5.0$ GeV (Figure 6.34);

- require either $EPION > 3.0$ GeV or $EPION < 3.0$ GeV and no tracks in MUB beyond the $1^{st}$ layer (Figure 6.35);
- require $M_\rho < 2.0\ GeV/c^2$ (Figures 6.36 and 6.37);
- for events with $\pi\gamma\gamma$ topology, require most energetic photon to have $E < 20.0$ GeV and second photon to have $E < 3.5$ GeV (Figure 6.38) in the 1991 analysis, to suppress $a_1$ background;
- require $0.04\ GeV/c^2 < M_{\pi^0} < 0.40$ and $GeV/c^2$ (Figure 6.39) in the 1992 analysis, to suppress the background from radiative pions and electrons which have been enhanced by the increased sensitivity to low energy showers in the HPC;
- require $E_{\pi^0} < 35.0$ GeV in the 1992 analysis, to suppress hard radiative events;
- to minimize electron background in events with $\pi\gamma$ topology, require that $E_{neutral} > 3.0$ GeV AND require that the first layer of energy deposition $< 4$.

### Results from 1991 Data Analysis

These selection criteria resulted in a sample of 1431 $\rho$ candidates for the 1991 data sample, with an overall efficiency of $47.65 \pm 0.66\%$ in the fiducial region (Figure 6.40). The total internal background computed from Monte Carlo simulation is $19.77 \pm 0.47\%$, and the background from $e^+e^- \to e^+e^-$ is $0.1 \pm 0.03\%$.

A 2-dimensional fit to the cosine angles distribution (Figure 6.41) yields

$$P_\tau = -0.181 \pm 0.061(stat.) \pm 0.055(syst.).$$

Table 6.12 summarizes the sources of background in this analysis, while the sources of the systematic errors are described in Table 6.13. The largest source of systematic uncertainty is the photon identification criteria, mostly from the requirement on energy deposition in HPC layers.

**Results from 1992 Data Analysis**

These selection criteria resulted in a sample of 3702 $\rho$ candidates for the 1992 data sample, with an overall efficiency of $42.62 \pm 0.54\%$ in the fiducial region (Figure 6.42). The total internal background computed from Monte Carlo simulation is $20.97 \pm 0.39\%$, and the background from $e^+e^- \to e^+e^-$ is $0.1 \pm 0.03\%$.

A 2-dimensional fit to the cosine angles distribution (Figure 6.43) yields

$$P_\tau = -0.189 \pm 0.036(stat.) \pm 0.034(syst.).$$

Table 6.14 summarizes the sources of background in this analysis, and the sources of the systematic errors are shown in Table 6.15. Though greatly reduced in 1992, the largest systematic uncertainty is still found in the photon identification criteria, especially the requirement on energy deposition in HPC layers.

Table 0.1: Background sources for the 1991 $\tau^- \to \rho^- \nu_\tau$ analysis.

| Decay mode | Background |
|---|---|
| $e\nu\overline{\nu}$ | $3.56 \pm 0.20\%$ |
| $\mu\nu\overline{\nu}$ | $0.64 \pm 0.08\%$ |
| $\pi\nu$ | $2.60 \pm 0.17\%$ |
| $a_1\nu$ | $8.61 \pm 0.31\%$ |
| $K\nu$ | $0.29 \pm 0.06\%$ |
| $K*\nu$ | $1.94 \pm 0.14\%$ |
| multi-$\pi\nu$ | $2.13 \pm 0.15\%$ |
| $e^+e^-$ | $0.10 \pm 0.03\%$ |
| $\mu^+\mu-$ | negligible |

Table 6.13: Systematic errors for the 1991 $\tau^- \rightarrow \rho^- \nu_\tau$ analysis.

| Source | Systematic Error |
|---|---|
| Rho ($\pi$) Identification | 0.012 |
| Photon Identification | 0.050 |
| Internal background | 0.017 |
| Monte Carlo simulation | 0.009 |

Table 6.14: Background sources for the 1992 $\tau^- \rightarrow \rho^- \nu_\tau$ analysis.

| Decay mode | Background |
|---|---|
| $e\nu\overline{\nu}$ | $2.12 \pm 0.11\%$ |
| $\mu\nu\overline{\nu}$ | $0.35 \pm 0.04\%$ |
| $\pi\nu$ | $2.31 \pm 0.12\%$ |
| $a_1\nu$ | $11.15 \pm 0.30\%$ |
| $K\nu$ | $0.17 \pm 0.03\%$ |
| $K*\nu$ | $1.75 \pm 0.10\%$ |
| multi-$\pi\nu$ | $3.12 \pm 0.14\%$ |
| $e^+e^-$ | $0.06 \pm 0.03\%$ |
| $\mu^+\mu-$ | negligible |

Table 6.15: Systematic errors for the 1992 $\tau^- \rightarrow \rho^- \nu_\tau$ analysis.

| Source | Systematic Error |
|---|---|
| Rho ($\pi$) Identification | 0.004 |
| Photon Identification | 0.028 |
| Internal background | 0.016 |
| Monte Carlo simulation | 0.007 |

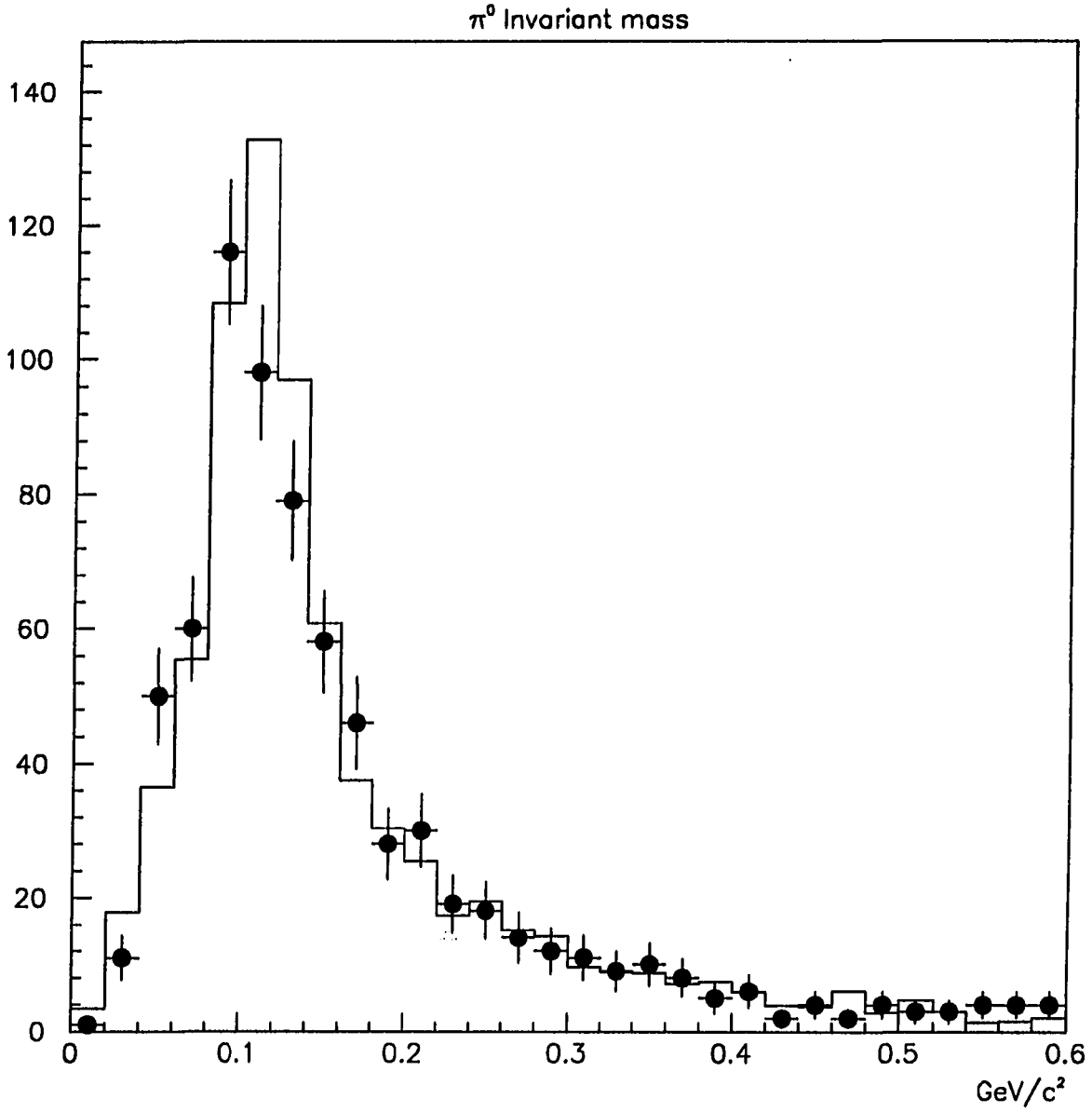


Figure 6.28: 1991 data (dots) with tau Monte Carlo (solid line) prediction superimposed for $\pi^0$ invariant mass.

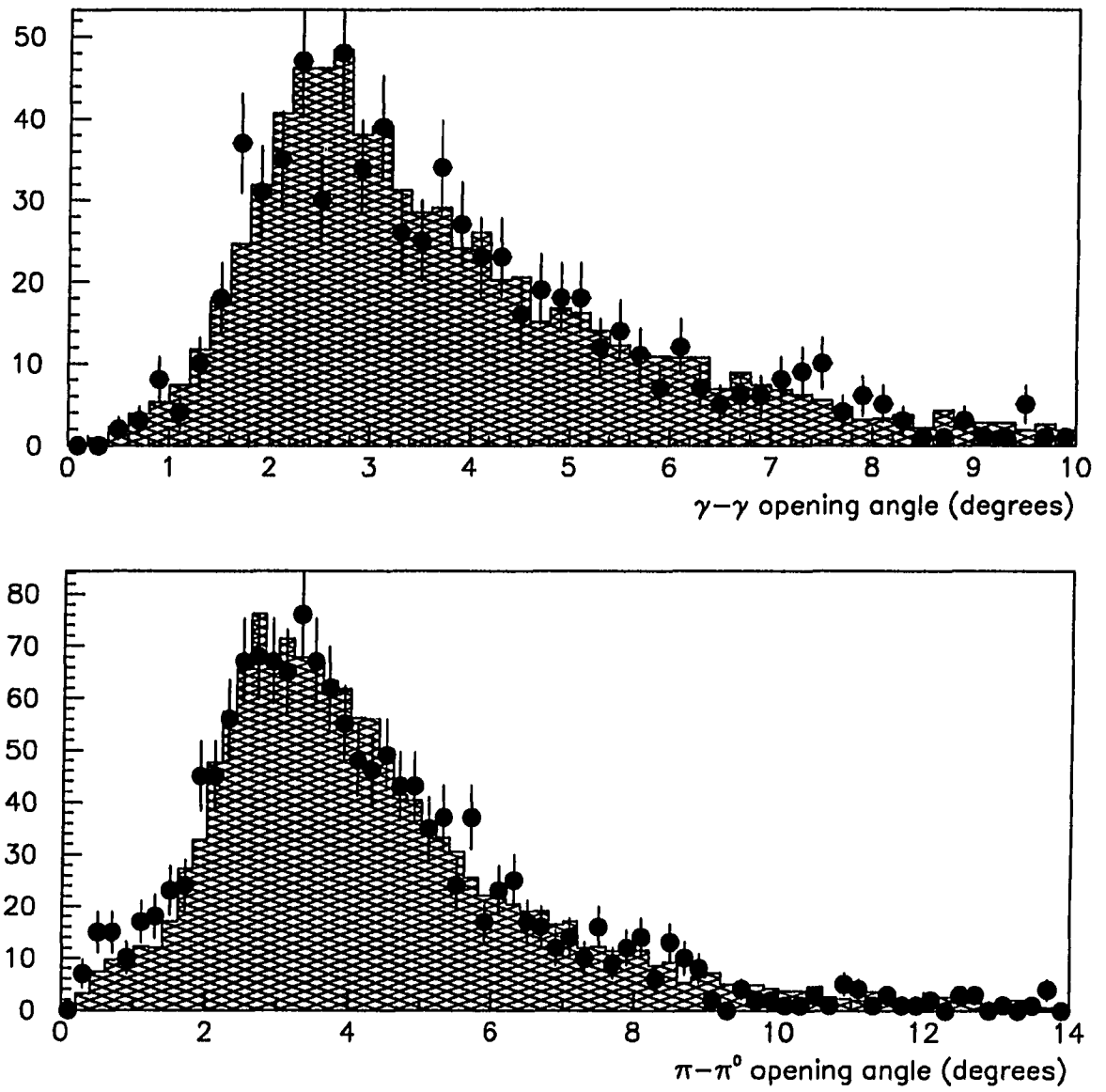


**Figure 6.29:** 1991 data (dots) with tau Monte Carlo (hatched) prediction superimposed for $\gamma$-$\gamma$ opening angle (top) and $\pi$-$\pi^0$ opening angle (bottom).

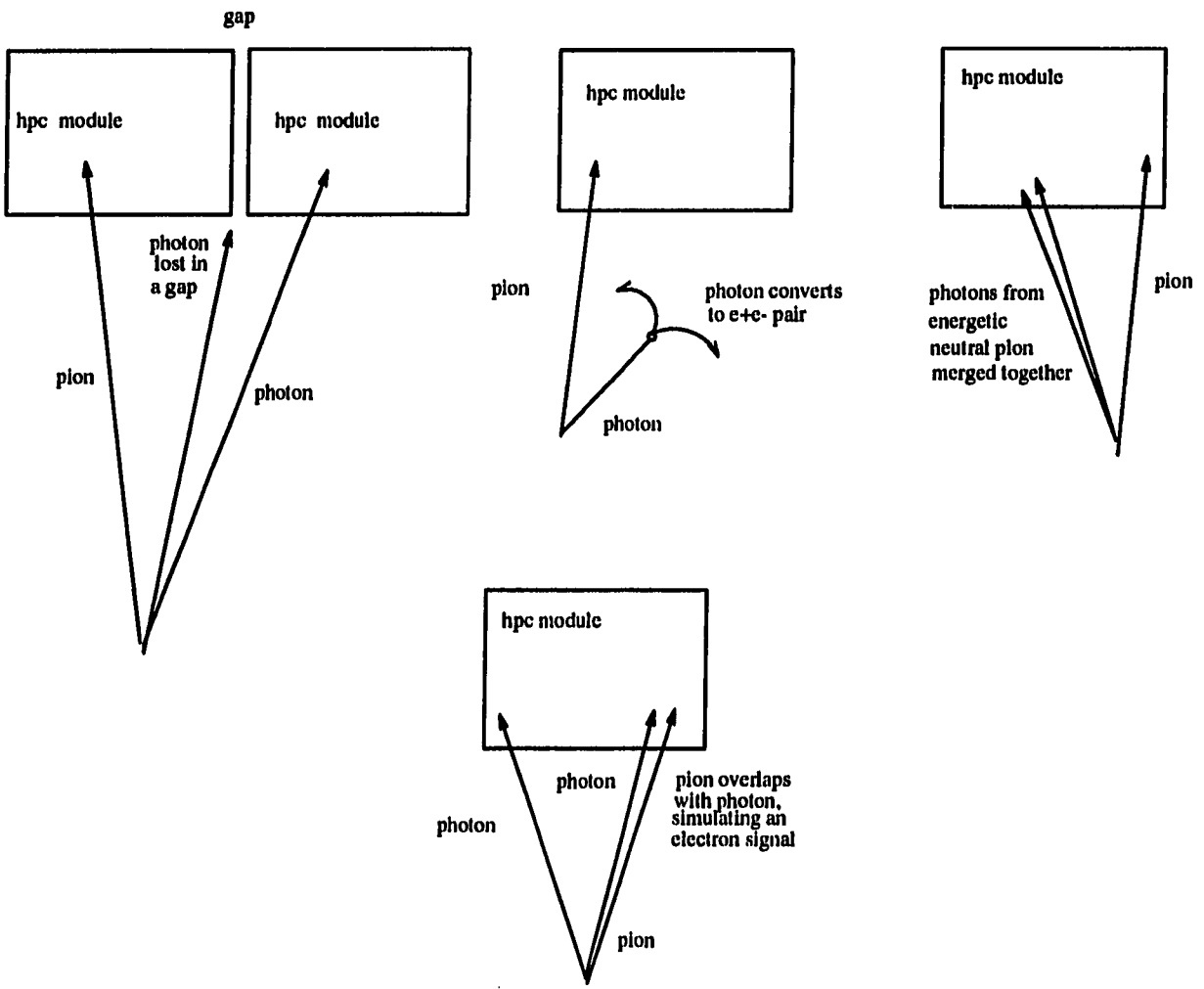


Figure 6.30: Main difficulties in identifying $\tau^- \rightarrow \rho^- \nu_\tau$ events at DELPHI.

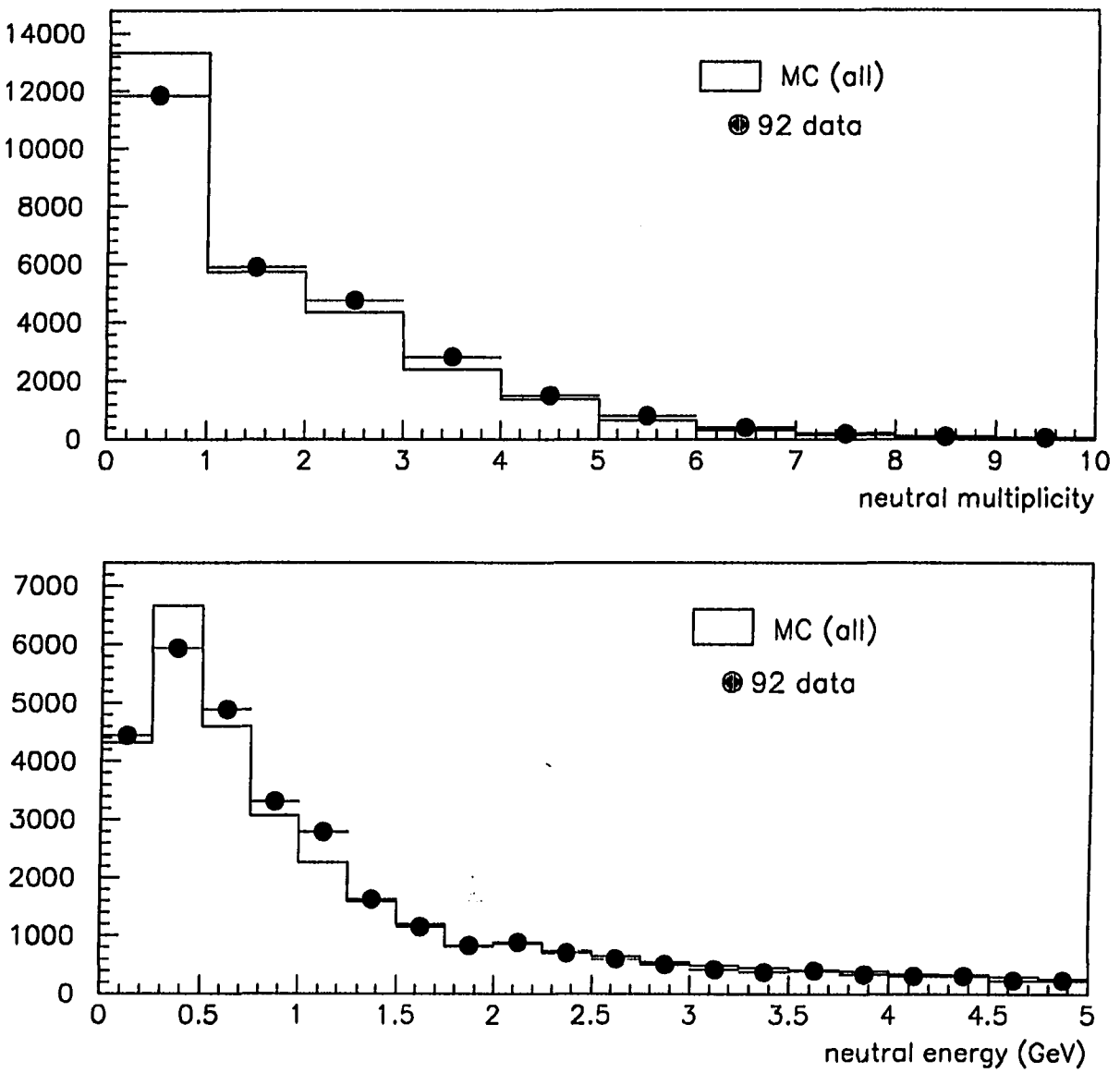


**Figure 6.31:** 1992 data with tau Monte Carlo superimposed for neutral multiplicity (top) and neutral energy (bottom).

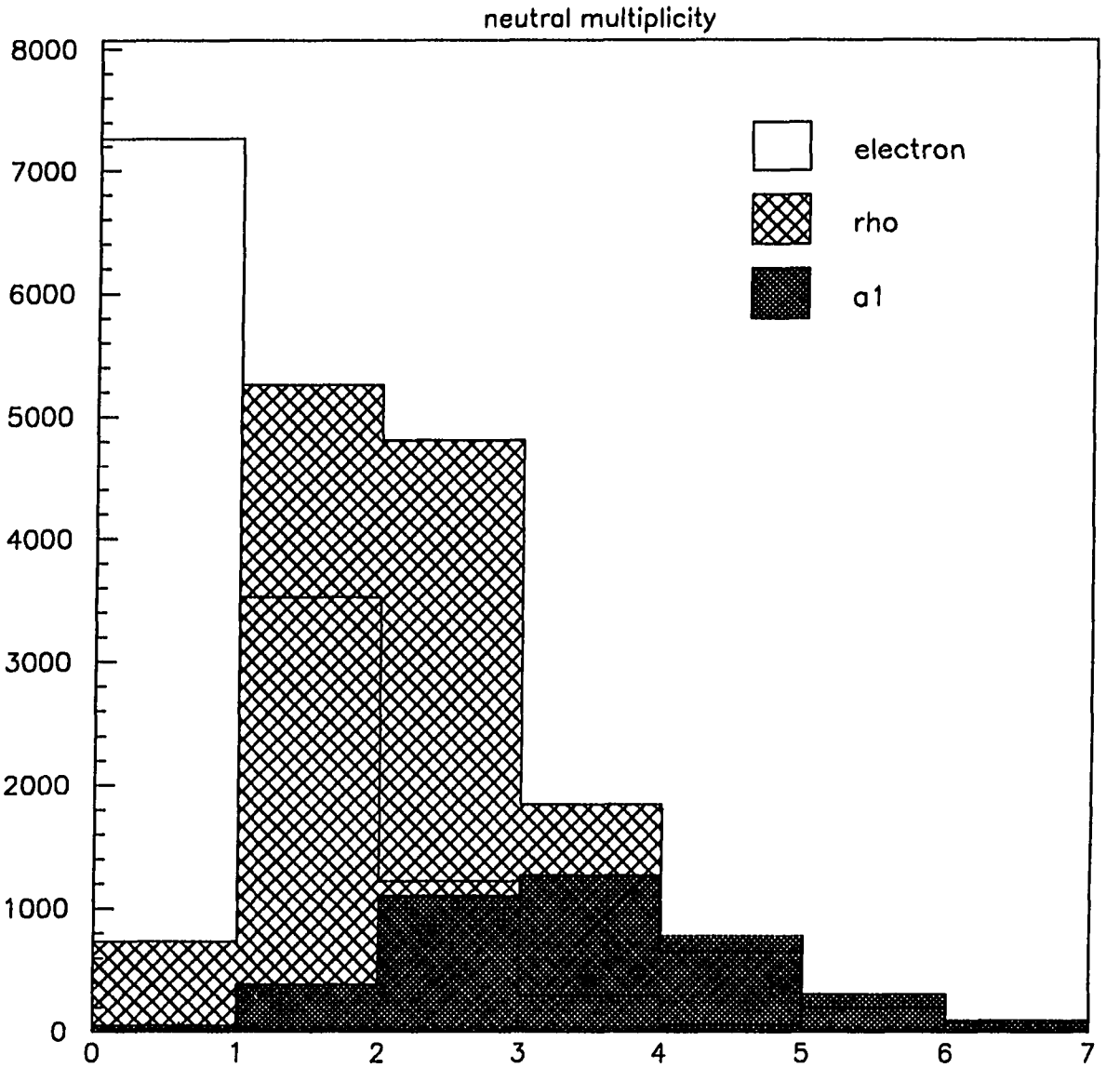


**Figure 6.32: Tau Monte Carlo prediction for neutral multiplicity.**

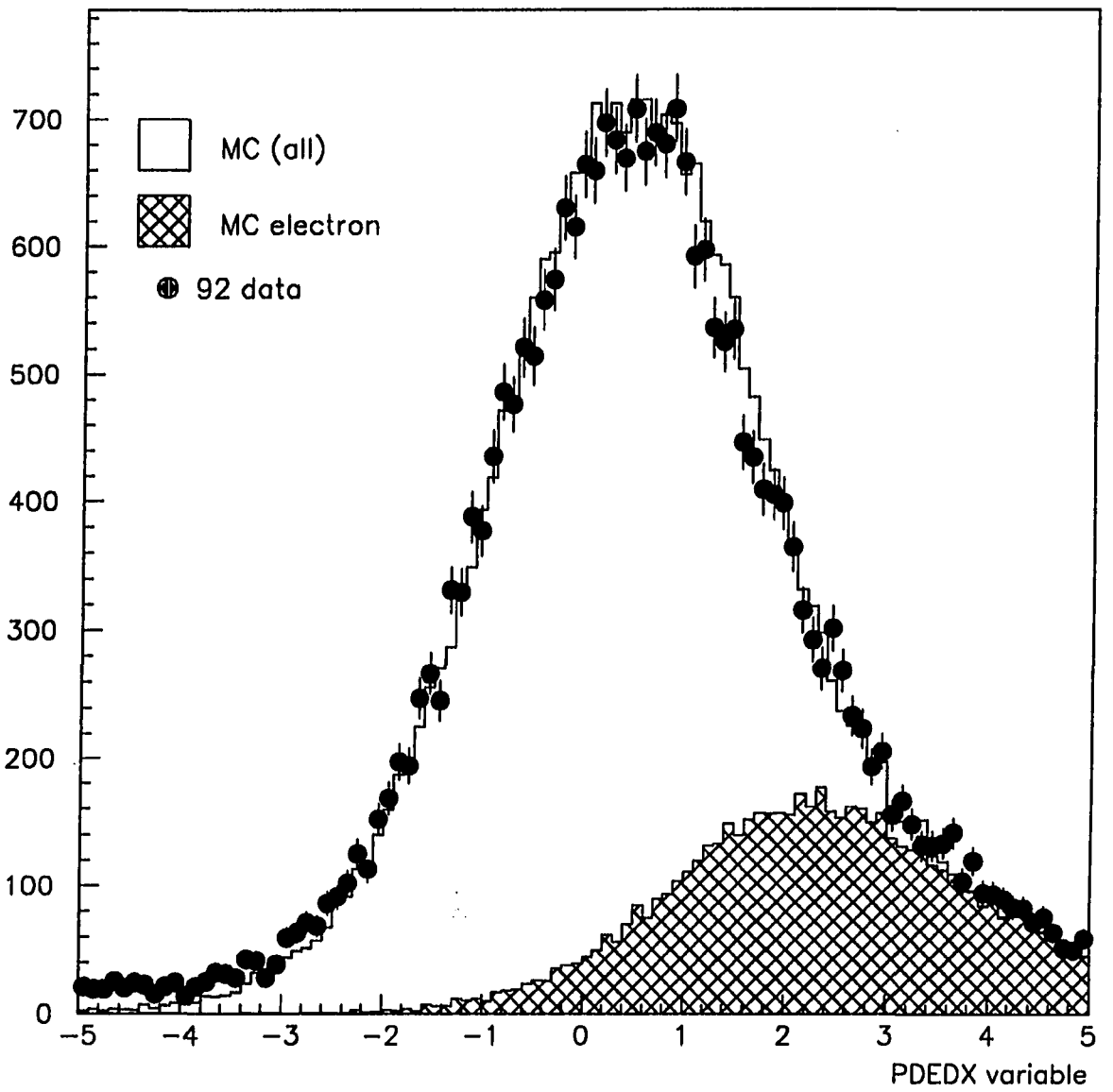


**Figure 6.33:** PDEDX variable. Overall tau Monte Carlo prediction, with 1992 data and tau Monte Carlo prediction for electrons superimposed .

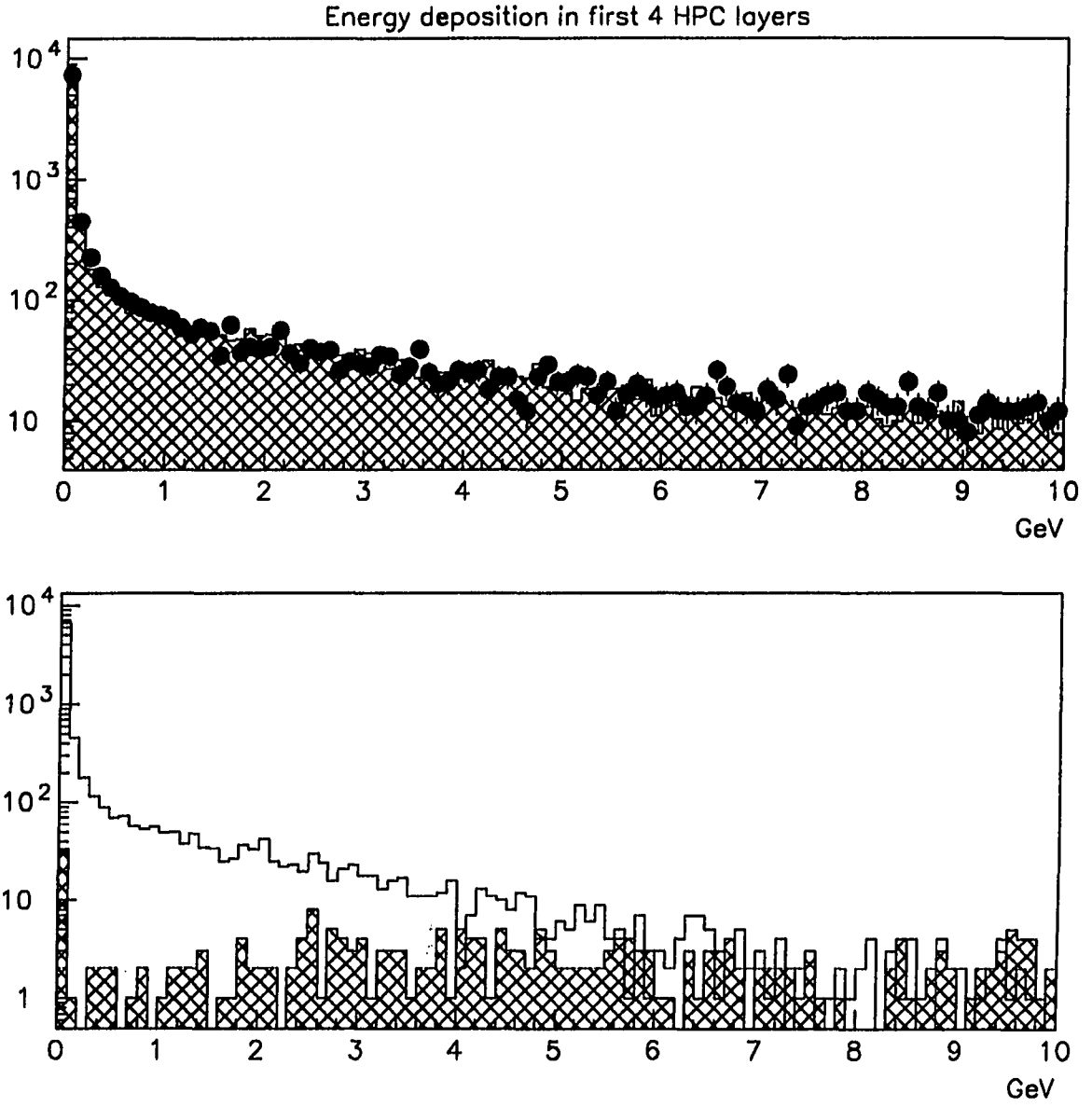


**Figure 6.34:** 1992 data (*dots*) with tau Monte Carlo (hatched) prediction superimposed (top) and tau Monte Carlo prediction for rho (hatched) and background (solid line) signals (bottom).

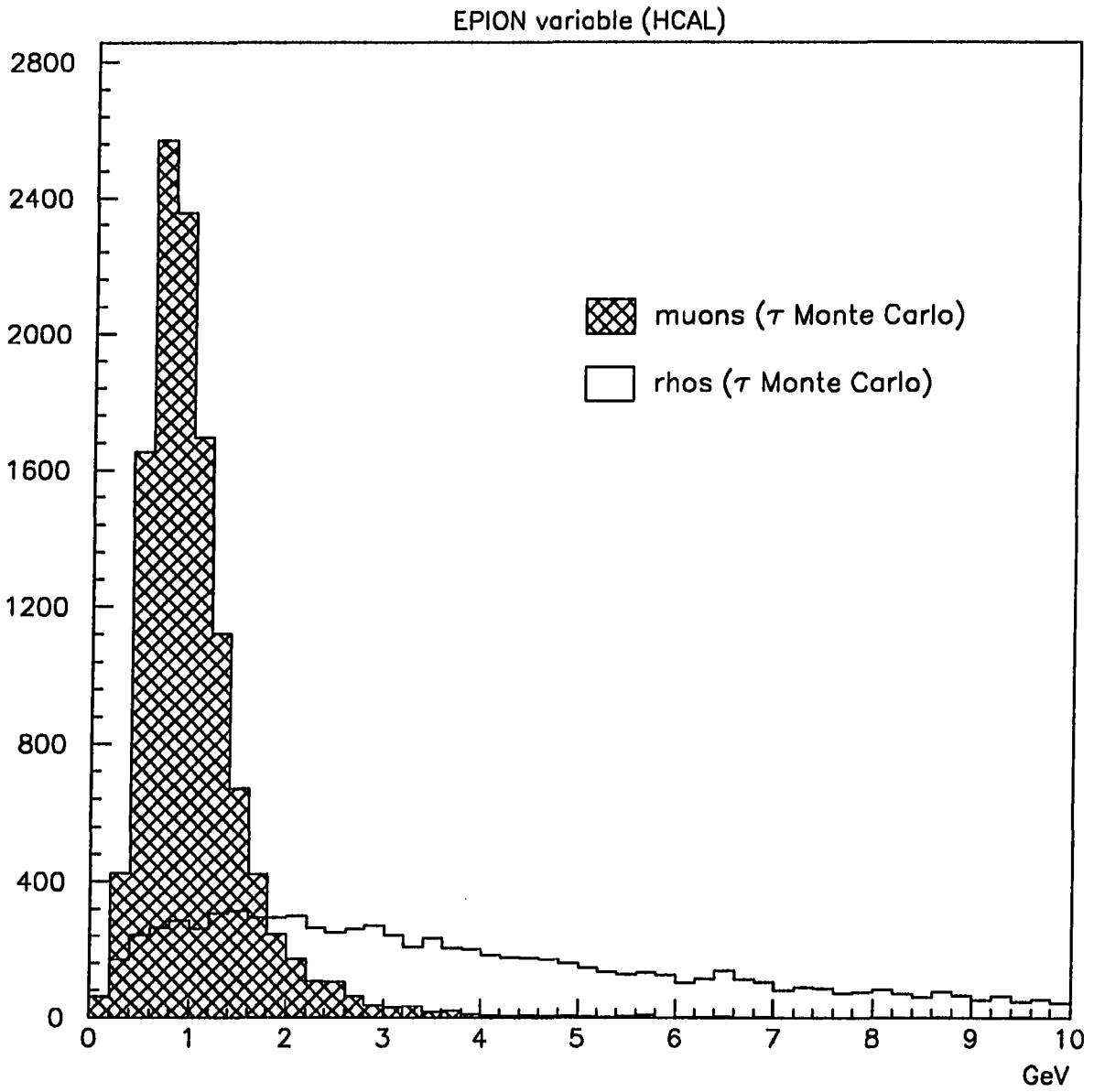


**Figure 6.35:** Tau Monte Carlo prediction for the EPION variable for muons and rhos.

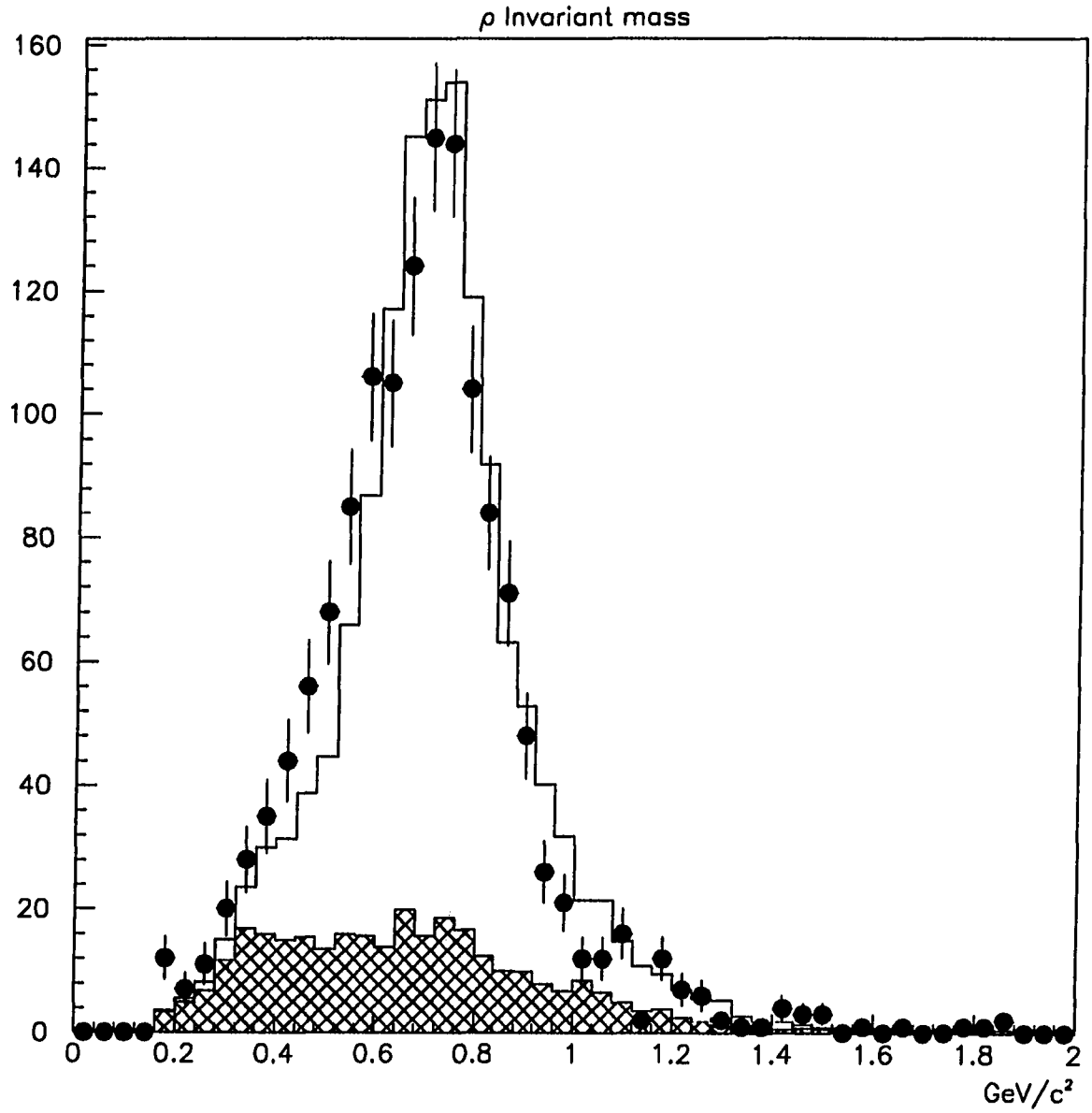


**Figure 6.36:** 1991 data (dots) and tau Monte Carlo prediction for signal (solid line) and background (hatched) for $\rho$ invariant mass.

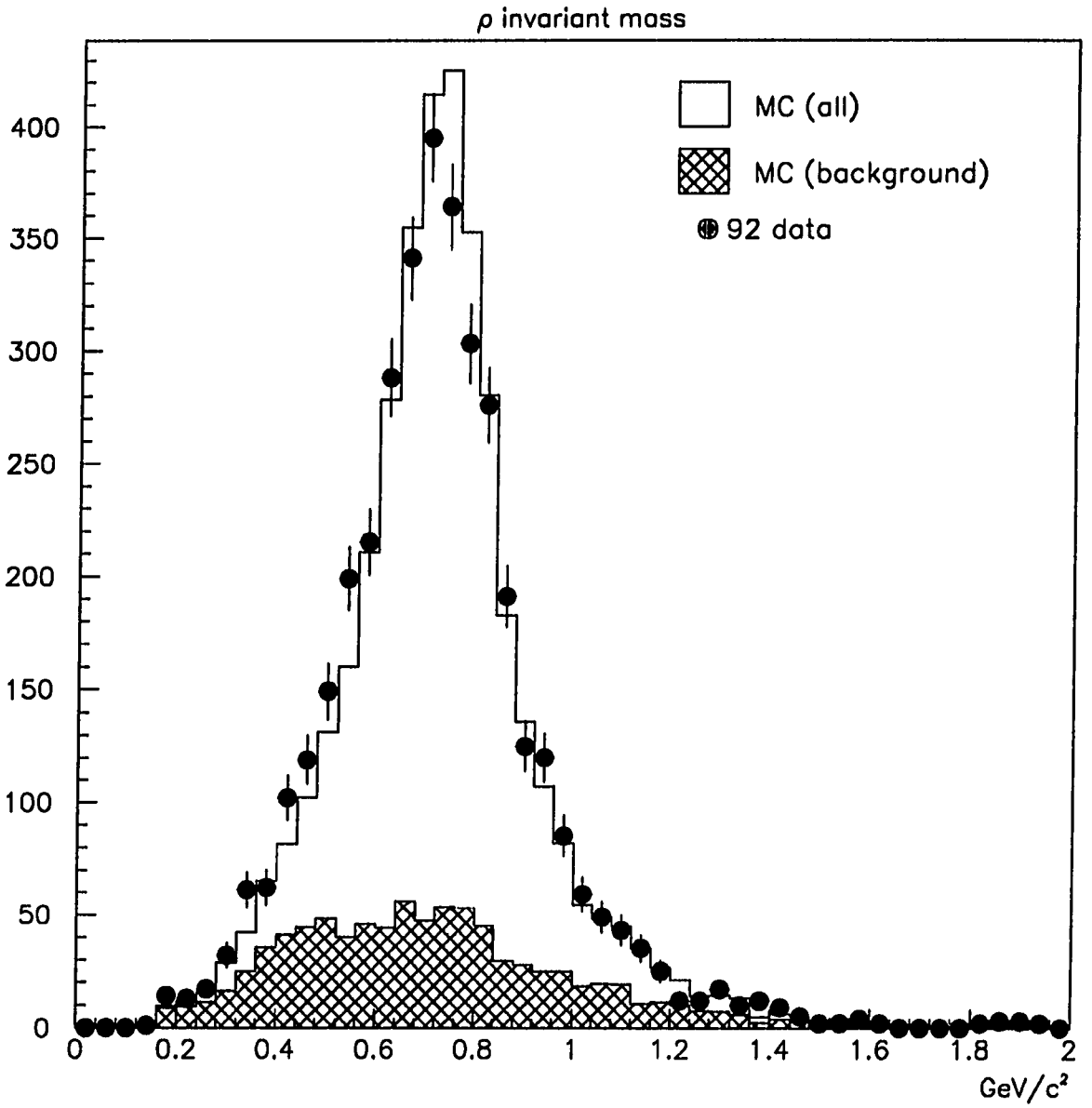


**Figure 6.37:** 1992 data and tau Monte Carlo prediction for signal and background superimposed for $\rho$ invariant mass.

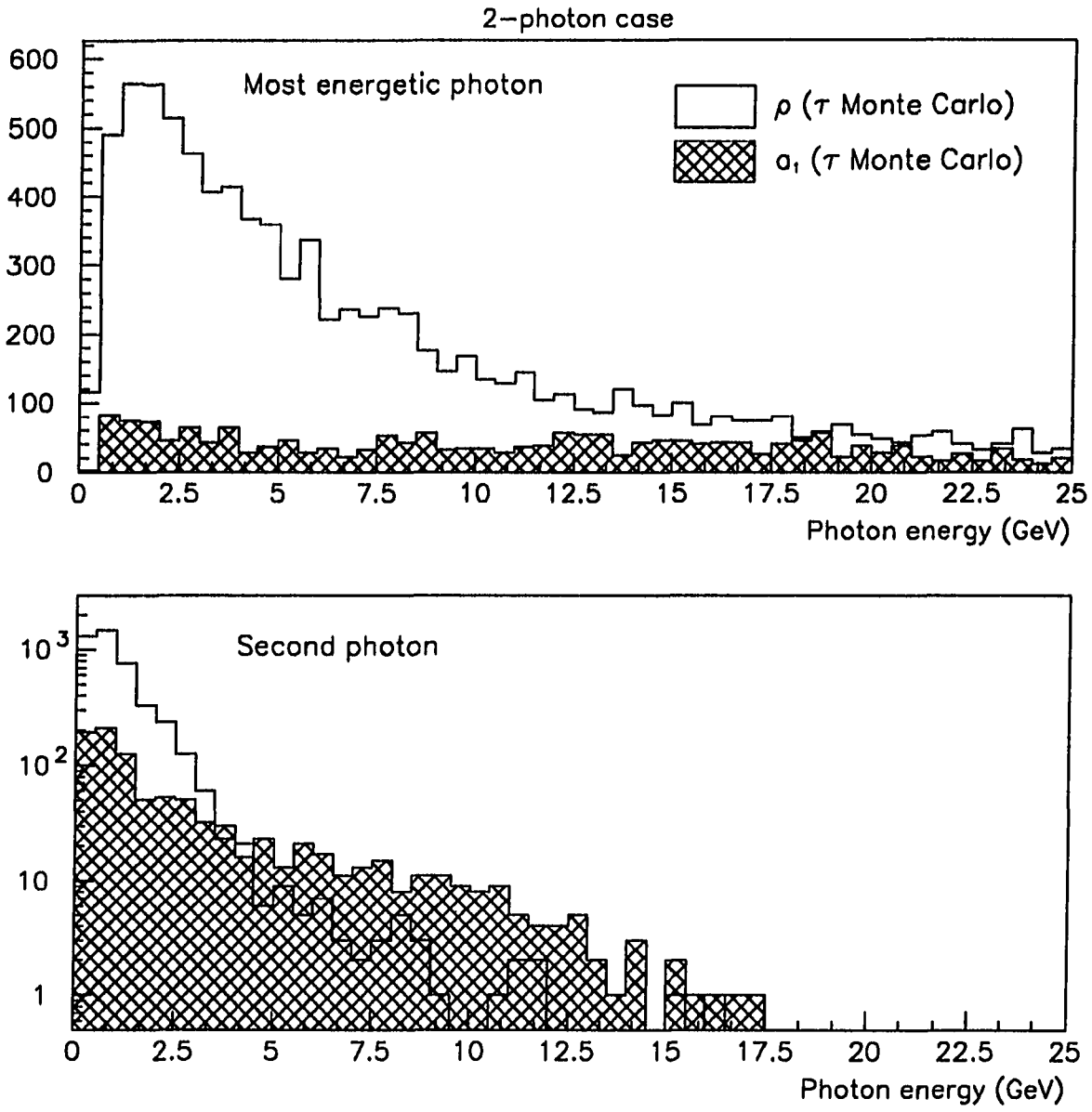


**Figure 6.38:** Tau Monte Carlo prediction for rho and $a_1$ for most energetic photon (top) and the second photon (bottom).

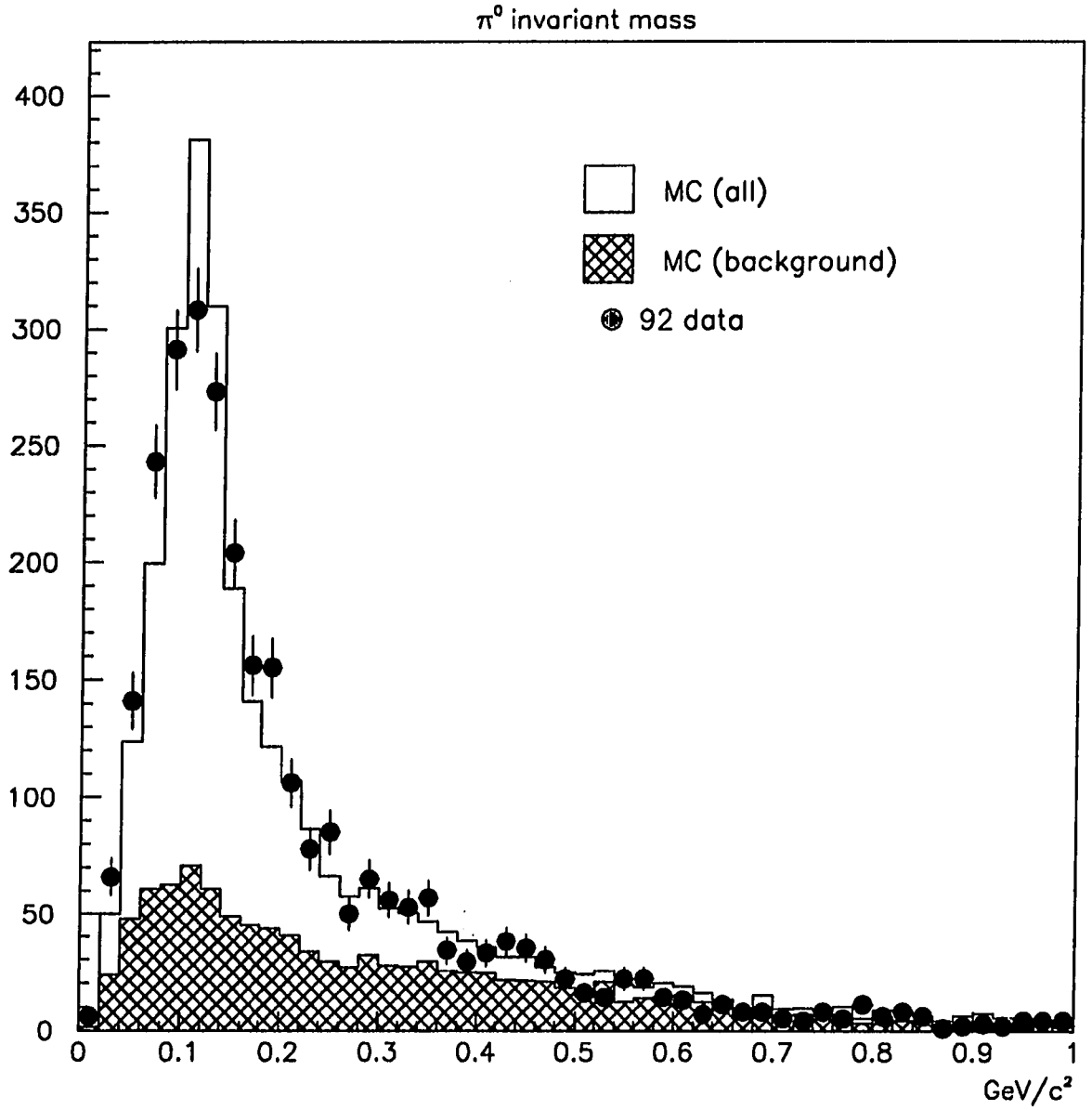


**Figure 6.39:** 1992 data with tau Monte Carlo prediction for signal and background superimposed for $\pi^0$ invariant mass.

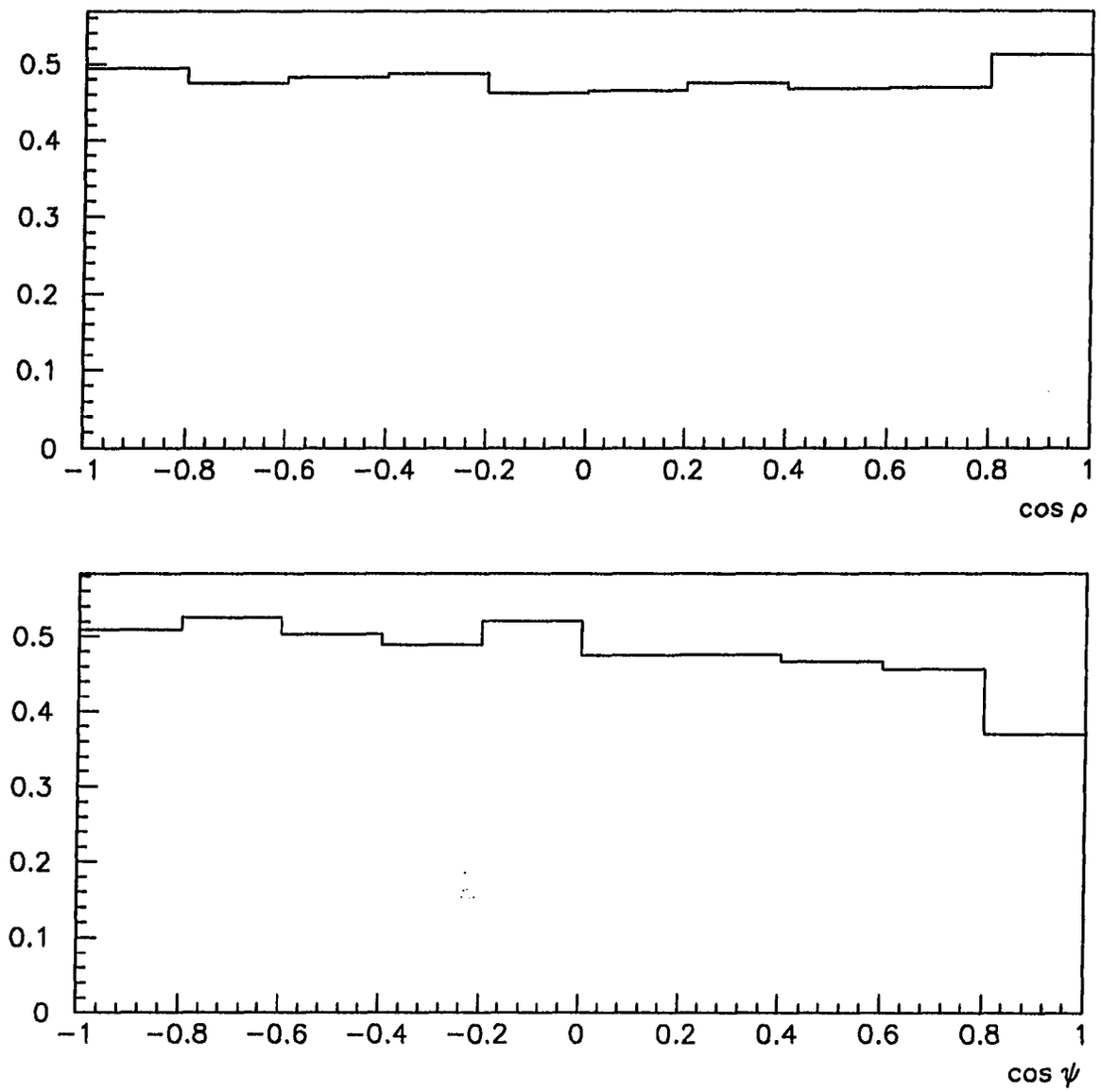


**Figure 6.40: Rho selection efficiency for 1991 data as a function of the cosine angles.**

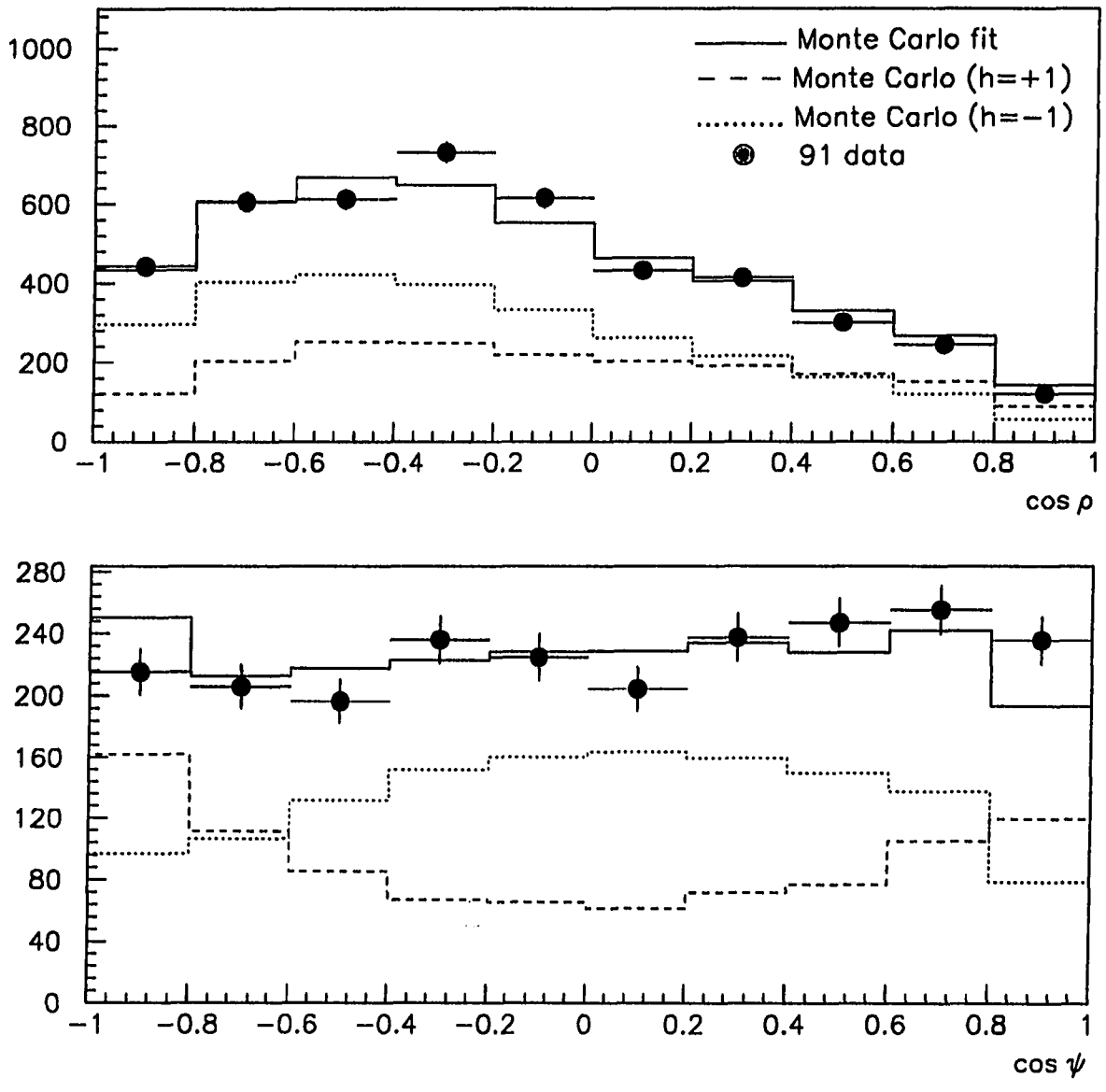


**Figure 6.41:** Two dimensional fit on the cosine angles of tau Monte Carlo to 1991 data for rho candidates. The Monte Carlo positive and negative helicity components are also shown.

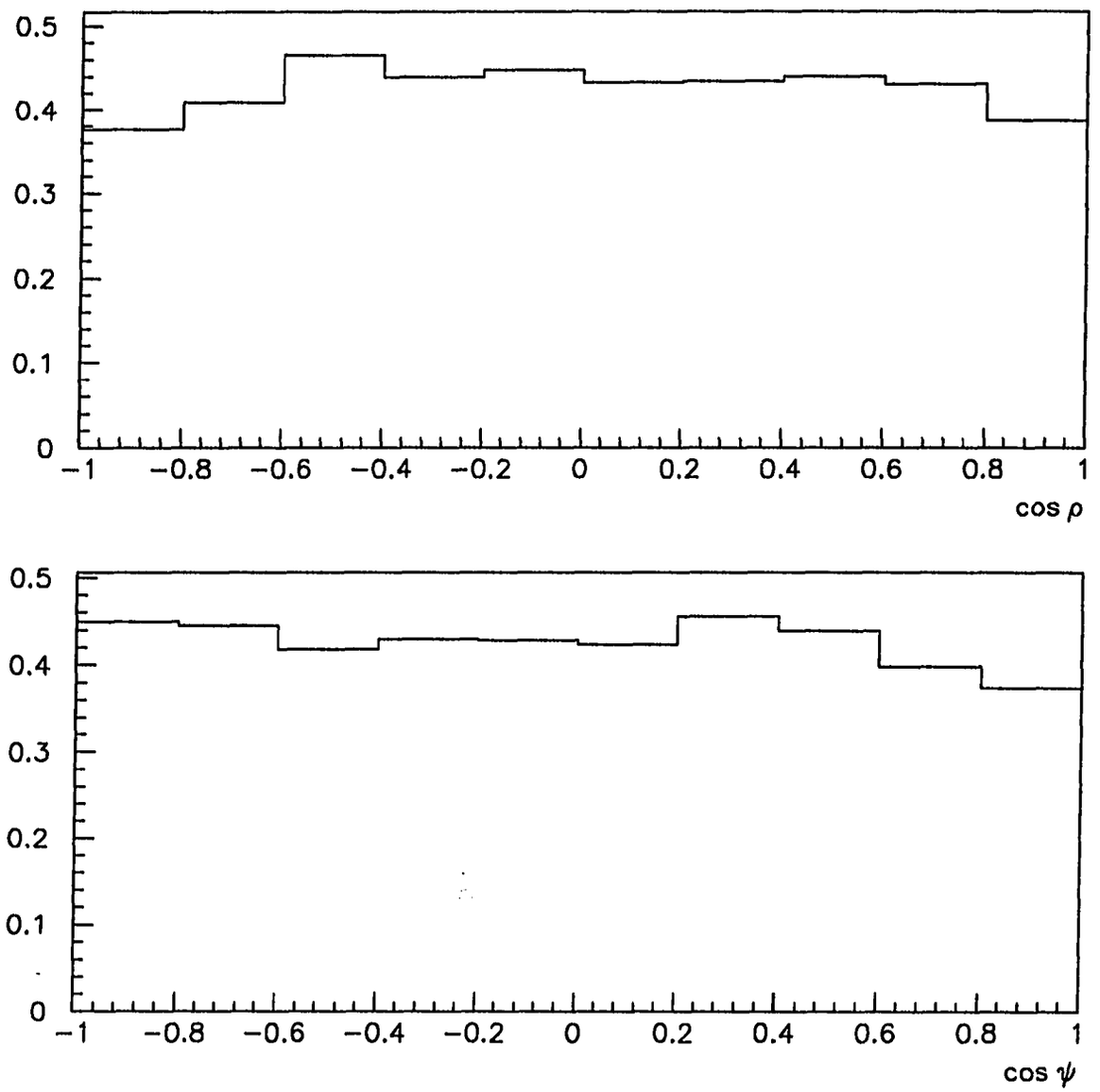


**Figure 6.42: Rho selection efficiency for 1992 data as a function of the cosine angles.**

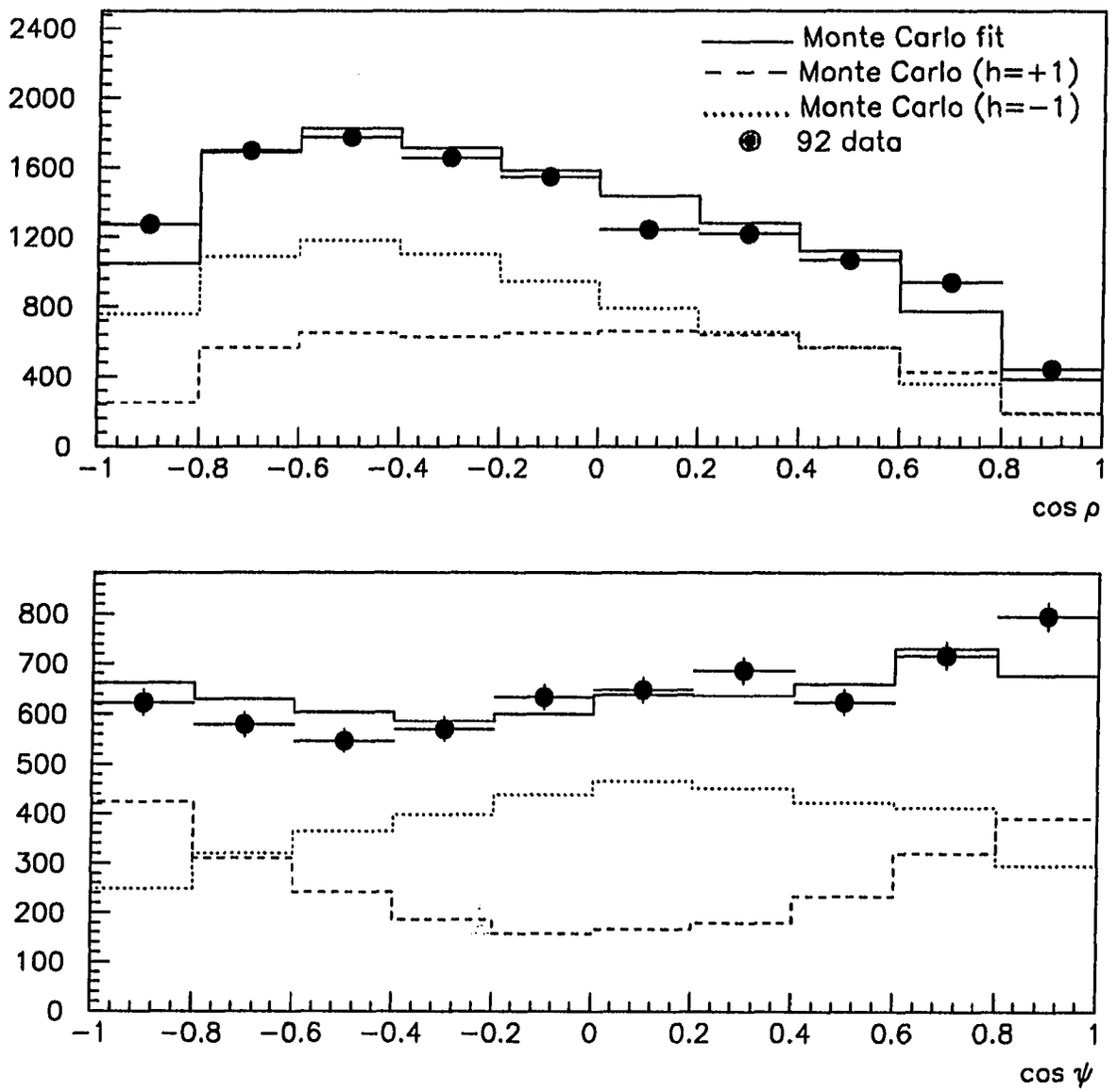


**Figure 6.43:** Two dimensional fit on the cosine angles of tau Monte Carlo to 1992 data for rho candidates. The Monte Carlo positive and negative helicity components are also shown.

## Analysis Summary

The statistical data for each of the channels studied in this analysis are summarized in Table 6.16. Table 6.17 summarizes the different acceptances for the two helicity states and the resulting acceptance corrections to the raw fit. The acceptance corrections are necessary to obtain a measurement of the polarization of the full data sample. Without them, the polarization measurement is only valid for the selected data sample.

Table 6.16: Summary of analysis statistics.

| Decay mode | Number of Decays | Selection Efficiency | Background |
|---|---|---|---|
| $e^-\overline{\nu}\nu$ (1991 data) | 1204 | 0.6056 | 0.0348 |
| $\pi^-\nu$ (1991 data) | 605 | 0.5255 | 0.0956 |
| $\rho^-\nu$ (1991 data) | 1431 | 0.4765 | 0.1987 |
| $e^-\overline{\nu}\nu$ (1992 data) | 3358 | 0.6540 | 0.0230 |
| $\pi^-\nu$ (1992 data) | 1613 | 0.5635 | 0.0897 |
| $\rho^-\nu$ (1992 data) | 3702 | 0.4262 | 0.2097 |

Table 6.17: Summary of acceptance corrections.

| Decay mode | Acceptance ($h = +1$) | Acceptance ($h = -1$) | Corr. Factor |
|---|---|---|---|
| $e^-\overline{\nu}\nu$ (1991 data) | 0.4790 | 0.4796 | 1.0004 |
| $\pi^-\nu$ (1991 data) | 0.2605 | 0.3031 | 1.0620 |
| $\rho^-\nu$ (1991 data) | 0.3933 | 0.4417 | 1.0480 |
| $e^-\overline{\nu}\nu$ (1992 data) | 0.4864 | 0.5181 | 1.0280 |
| $\pi^-\nu$ (1992 data) | 0.2997 | 0.3289 | 1.0400 |
| $\rho^-\nu$ (1992 data) | 0.3569 | 0.4041 | 1.0530 |

# CHAPTER 7. CONCLUSIONS

The parity violating nature of the weak neutral current has been demonstrated by a precise measurement of the non-zero polarization of $\tau$ leptons produced in $Z^0$ decays. The $\tau$ sample was selected from events collected in 1991 and 1992, corresponding to $1 \times 10^6$ $Z^0$ hadronic decays.

The results for each of the channels studied in this analysis are summarized in Table 7.1. The weighted mean of all the decay modes analyzed is

$$P_\tau = -0.176 \pm 0.029.$$

The statistical and systematic errors have been added in quadrature, neglecting small correlations between systematic errors of the different decay channels analyzed.

Table 7.1: Summary of $\tau$ polarization measurements.

| Decay mode | $P_\tau$ | $\Delta P_\tau$ (stat.) | $\Delta P_\tau$ (syst.) |
|---|---|---|---|
| $e^-\bar{\nu}\nu$ (1991 data) | −0.223 | 0.111 | 0.080 |
| $\pi^-\nu$ (1991 data) | −0.128 | 0.074 | 0.057 |
| $\rho^-\nu$ (1991 data) | −0.181 | 0.061 | 0.055 |
| $e^-\bar{\nu}\nu$ (1992 data) | −0.134 | 0.075 | 0.062 |
| $\pi^-\nu$ (1992 data) | −0.180 | 0.046 | 0.037 |
| $\rho^-\nu$ (1992 data) | −0.189 | 0.036 | 0.034 |

This measured value of the $\tau$ polarization differs from zero by more than six standard deviations, confirming the non-zero polarization of $\tau$ leptons produced at LEP [37].

These results imply that parity is violated in the weak neutral current process $e^+e^- \rightarrow Z^0 \rightarrow \tau^+\tau^-$. Parity violation in the weak neutral current has been

previously reported in polarized electron inelastic scattering and in atomic transitions [38,39], in keeping with both lepton universality and the SM electroweak theory.

In the context of the SM, this value for the average polarization implies a ratio of the weak neutral current vector to axial-vector couplings

$$\frac{v_\tau}{a_\tau} = 0.088 \pm 0.014.$$

Note that the sign of the ratio is determined by this measurement and that the $Z \rightarrow \tau^+\tau^-$ decay is dominated by the axial-vector current.

This result can be recast to yield a value of the effective mixing angle

$$sin^2\theta_W(M_Z^2) = 0.2280 \pm 0.0036,$$

a measurement with a 1.6% uncertainty.

Figure 7.1 compares this result for $sin^2\theta_W$ with previous measurements by various different non-LEP experiments, along with recent LEP measurements [8,43]. The low-energy, non-LEP measurements have been evolved to $M_Z^2$ for comparison with LEP data. The improved accuracy of the LEP measurements and the power of the $\tau$ polarization methods are evident. This result is in good agreement with previously published results [6,41,42] in the hadronic and leptonic forward-backward asymmetry measurements, from the study of the $Z^\circ$ lineshape and from measurements performed at fixed target experiments and hadron colliders.

The mass of the $W^\pm$ boson is related to $sin^2\theta_W$ through the following expression, assuming that $\rho = 1$ in (1.14):

$$M_W = M_Z \cdot \sqrt{(1 - sin^2\theta_W)} \ . \qquad (7.1)$$

Using the combined LEP value for the mass of the $Z^\circ$ boson, $M_Z = 91.188 \pm 0.007$ $GeV/c^2$ [16] and the result obtained in this analysis for $\sin^2\theta_W$, we obtain

$$M_W = 80.121 \pm 0.633 \ \ GeV/c^2,$$

in excellent agreement with recent measurements of $M_W$ [8].

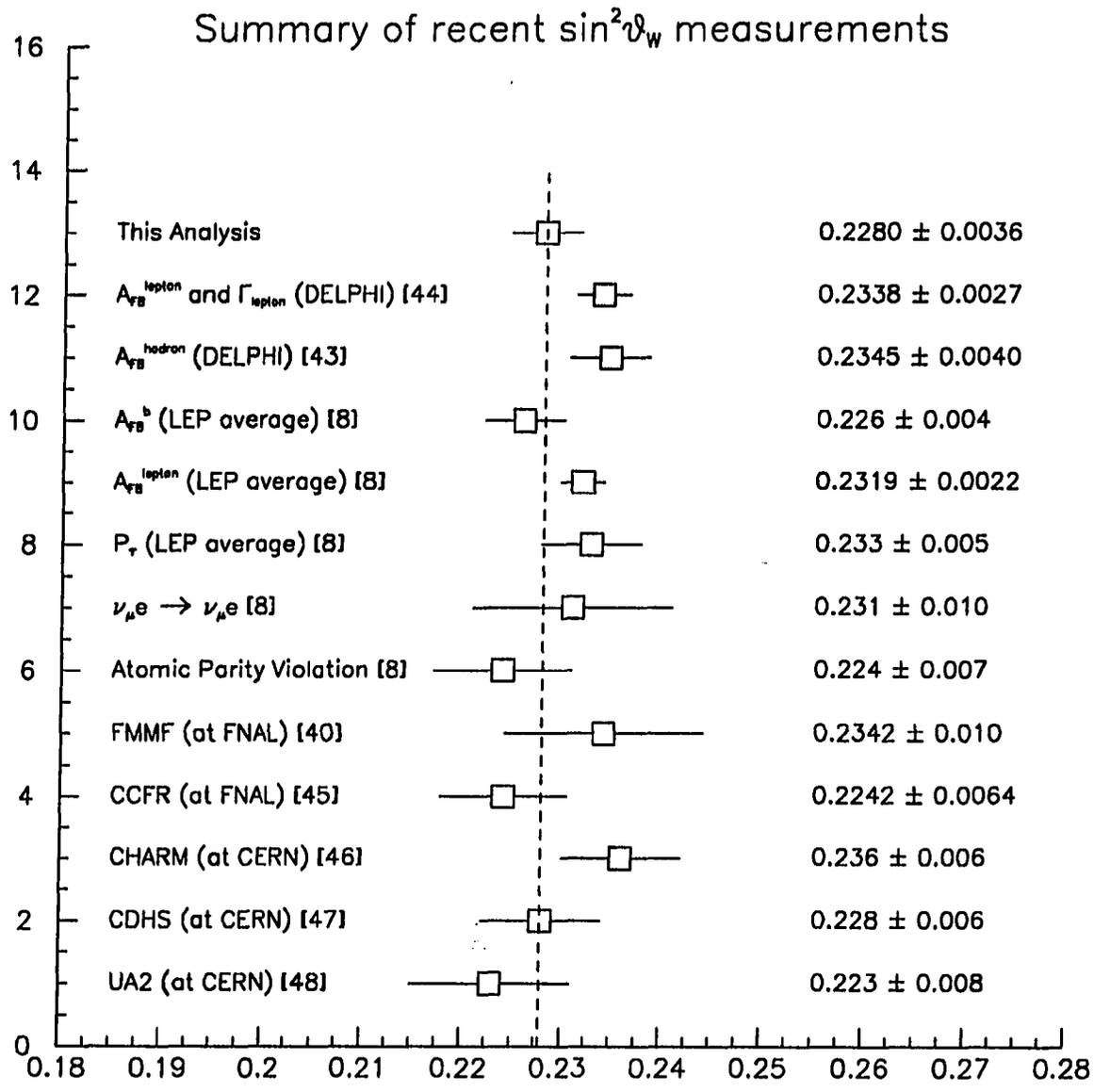


**Figure 7.1:** A summary of recent $sin^2\theta_W$ measurements. This analysis is in good agreement with previous measurements.

## REFERENCES

[ 1] F. Halzen & A. D. Martin, *Quarks & Leptons: An Introductory Course in Modern Particle Physics*, (John Wiley & Sons, Inc., New York, New York, 1984), p. 334.

[ 2] D. H. Perkins, *Introduction to High Energy Physics*, (Addison Wesley Publishing Company, Inc., Reading, Massachusetts, 1987), p. 315.

[ 3] J. E. Dodd, *The Ideas of Particle Physics*, (Cambridge University Press, Cambridge, Great Britain, 1984), p. 89.

[ 4] F. Halzen & A. D. Martin, *Quarks & Leptons: An Introductory Course in Modern Particle Physics*, (John Wiley & Sons, Inc., New York, New York, 1984), p. 280.

[ 5] D. H. Perkins, *Introduction to High Energy Physics*, (Addison Wesley Publishing Company, Inc., Reading, Massachusetts, 1987), p. 239.

[ 6] CDF Collaboration, F. Abe *et al.*, Phys. Rev. D 45 (1992) 3921.

[ 7] P. B. Renton, *Recent Physics Results from DELPHI*, (Geneva, Switzerland, 1990), DELPHI 90-56 PHYS 75.

[ 8] Review of Particle Properties, M. Aguillar-Benitez *et al.*, Phys. Rev. D 45, Part II (1992).

[ 9] F. Halzen & A. D. Martin, *Quarks & Leptons: An Introductory Course in Modern Particle Physics*, (John Wiley & Sons, Inc., New York, New York, 1984), p. 307.

[10] MARK I Collaboration, M. L. Perl *et al.*, Phys. Rev. Lett. 35 (1975) 1489.

[11] Y. S. Tsai, Phys. Rev. D 4 (1971) 2821.

[12] D. H. Perkins, *Introduction to High Energy Physics*, (Addison Wesley Publishing Company, Inc., Reading, Massachusetts, 1987), p. 254.

[13] W. J. Marciano and A. Sirlin, Phys. Rev. Lett. 61 (1988) 1815.

[14] BES Collaboration, N. Qi, plenary talk at APS Conference, (Washington (D.C.), April, 1992).

[15] R. Stroynowski, plenary talk at Rencontre de Moriond, (Moriond, France, March, 1992).

[16] S. C. C. Ting, plenary talk at The Fermilab Meeting - DPF 92, (Chicago, November, 1992).

[17] R. Kleiss *et al.*, *Proceedings of the workshop on Z physics at LEP I*, edited by G. Altarelli, R. Kleiss, C. Verzegnassi, (Geneva, Switzerland, 1989), CERN 89-08, Vol. 1, p. 237.

[18] S. Okada, *Proceedings of the Workshop on $\tau$ lepton physics*, edited by M. Davier and B. Jean-Marie, (Orsay, France, 1990). See also preprint KEK 90-164 (1990).

[19] DELPHI Collaboration, P. Abreu *et al.*, Nucl. Inst. A 303 (1991) 233.

[20] DELPHI Collaboration, P. Abreu *et. al.*, Phys. Lett. B 267 (1991) 422.

[21] A. Rouge, plenary talk at Rencontre de Moriond, (Moriond, France, March, 1992).

[22] G. Bouchiat and L. Michel, Phys. Rev. 106 (1957) 170.

[23] K. Hagiwara, A. D. Martin, D. Zeppenfeld, Phys. Lett. B 235 (1990) 198.

[24] A. Rouge, Z. Phys. C 48 (1990) 75.

[25] E. Longo and I. Sestili, Nucl. Inst. 128 (1985) 283.

[26] P. Bombade and P. Zalewski, *Study of electron identification in hadronic jets*, (Geneva, Switzerland, 1992), DELPHI 92-32, PROG 183.

[27] M. Dam, private communication.

[28] D. Bolini *et al.*, *Study of the structure of hadronic and electromagnetic showers with a segmented iron-scintillator calorimeter*, Nucl. Inst. 171 (1980) 237.

[29] P. Privitera, private communication.

[30] DELANA User Guide for the DELPHI Data Analysis Program, (Geneva, Switzerland, 1989), DELPHI 87-44 PROG 137.

[31] TANAGRA User Guide for the Track Analysis and Graphics Program, (Geneva, Switzerland, 1989), DELPHI 87-95 PROG 98.

[32] Y. Sacquin, DELPHI DST Content, (Geneva, Switzerland, 1992), DELPHI 91-22 PROG 161 (Rev. 3).

[33] R. Kleiss *et al.*, *Proceedings of the workshop on Z physics at LEP I*, edited by G. Altarelli, R. Kleiss, C. Verzegnassi, (Geneva, Switzerland, 1989), CERN 89-08, Vol. 3, p. 1.

[34] DELSIM User Manual for the DELPHI Simulation Program, (Geneva, Switzerland, 1989), DELPHI 87-96 PROG 99.

[35] DELPHI Collaboration, P. Aarnio *et al.*, Nucl. Phys. B 367 (1991) 511.

[36] F. Matorras, *A selection for $\tau$ lepton studies*, (Geneva, Switzerland, 1992), DELPHI 92-124.

[37] ALEPH Collaboration, D. Abbaneo *et al.*, Phys. Lett. B 265 (1991) 430.

DELPHI Collaboration, P. Abreu *et al.*, Z. Phys. C 55 (1992) 555.

L3 Collaboration, *A measurement of $\tau$ polarization in $Z^0$ decays*, (Geneva, Switzerland, 1992), CERN-PPE 92-132.

OPAL Collaboration, *Measurement of Branching Ratios and $\tau$ polarization from $\tau \to e\nu\bar{\nu}$, $\tau \to \mu\nu\bar{\nu}$, $\tau \to \pi(K)\nu$ Decays at LEP*, (Geneva, Switzerland, 1991), CERN-PPE 91-103.

[38] C. Prescott *et al.*, Phys. Lett. B 77 (1978) 347.

[39] P. Privitera, *Physics of the $\tau$ lepton at LEP*, (Geneva, Switzerland, 1991), CERN-PPE 91-185.

[40] FMMF Collaboration, R. Brock *et al.*, *The Fermilab Meeting - DPF 92*, edited by C. H. Albright, P. H. Kasper, R. Raja and J. Yoh, (Chicago, November, 1992), Vol. 1, p. 421.

[41] DELPHI Collaboration, P. Abreu *et al.*, Phys. Lett. B 277 (1992) 371.

[42] P. Abreu *et al.*, *The $Z^0$ coupling to the $e^+e^-$ Final State*, (Geneva, Switzerland, 1991), DELPHI 91-19 PHYS 90.

[43] V. Innocente, plenary talk at Rencontre de Moriond, (Moriond, France, March, 1993).

[44] DELPHI Collaboration, P. Abreu *et al.*, Nucl. Phys. B 367 (1991) 511.

[45] L. Rolandi, invited talk at Conference on High Energy Physics, (Dallas, 1991).

[46] CHARM Collaboration, J. V. Allaby *et al.*, Z. Phys. C 36 (1987) 611.

[47] CDHS Collaboration, A. Blondel *et al.*, Z. Phys. C 45 (1990) 361.

[48] UA2 Collaboration, J. Alitti *et al.*, Phys. Lett. B 276 (1992) 354.